



Norwegian University of
Science and Technology

Effect of Porosity and Copper Content on Copper Containing SAPO-34 for Removal of NO_x

Anders Hutcheson

Chemistry

Submission date: May 2018

Supervisor: Karina Mathisen, IKJ

Norwegian University of Science and Technology
Department of Chemistry

Acknowledgement

First, I would like to thank my supervisor Dr. Karina Mathisen for being a great source of inspiration. She was the drive that made me want to do as much lab-work as possible and always showed interest in results obtained. I would also like to thank the staff at the Swiss Norwegian Beam line (SNBL) at the European Synchrotron Radiation Facility (ESRF) for their assistance during my stay in Grenoble. The funds for the travel and stay in Grenoble were granted by the Sparebanken Midt-Norges gavefond til Norges teknisk-Naturvitenskapelige universitet, for which I am eternally grateful.

In addition, this thesis would not have been half as good without the help of my co-supervisor, Ph.D. candidate Guro Sørli. The help you have given both in the lab and in general has been invaluable. Further, I would like to thank Ph.D. candidate Daniel Ali for showing me the ropes when it comes to everything IR. The rest of the research group also deserves a thank you for being a great bunch of people.

I also need to thank friends and family, who have supported me through this endeavour. I would like to thank Silje and Julian for lending support when needed and never failing to put a smile on my mouth. Finally, I would like to thank my mom who has been supportive from start to finish.

Abstract

In this thesis, hierarchical SAPO-34 with copper isomorphously substituted(H/CuSAPO-34) was attempted synthesised, by a hydrothermal method. As a step in the process, hierarchical SAPO-34 without copper(H/SAPO-34) was synthesised, also by a hydrothermal method. To evaluate the syntheses the following characterisation methods were employed: XRD, N₂-physisorption, SEM, ICP-MS, FTIR, and XAS.

A modified version of the syntheses done by Kong et.al.¹, where mesopores were generated by either cetyltrimethylammonium hydroxide(CTAOH) or glucose, yielded H/SAPO-34. The hierarchical nature of these samples was analysed based on comparison of N₂-physisorption results of an analogue conventional SAPO-34 sample, also synthesised by a hydrothermal method. For H/SAPO-34 samples the mesopore volumes was close to 0.20cm³/g, which is significantly larger compared to the conventional counterpart, where the mesopore volume was 0.005cm³/g. The H/SAPO-34 samples had poor catalytic performance for MTH, which was due to abnormally rapid coke formation leading to deactivation.

For the synthesis of H/CuSAPO-34 a variety of structure directing agents(SDA) was tested. Based on N₂-physisorption results, syntheses using either cetyltrimethylammonium bromide(CTAB) or CTAOH were found to give rise to mesoporosity. The HC-SCR catalytic performance for H/CuSAPO-34 made with CTAOH did not exceed that of an analogue hydrothermally synthesised conventional SAPO-34(C/CuSAPO-34), also with copper attempted introduce by isomorphous substitution. From XAS analysis the presence of non-incorporated copper in H/CuSAPO-34 samples were observed, which means that copper is partially incorporated or not incorporated at all.

Sammenheng

Hoved formålet med denne master oppgaven var å syntetisere hierarkisk SAPO-34 med inkorporert kobber(H/CuSAPO-34). I tillegg ble syntese av hierarkisk SAPO-34 uten kobber(H/SAPO-34) satt som et delmål. For både H/CuSAPO-34 og H/SAPO-34 ble en hydrotermisk syntese metode utført. For å evaluere produkter syntetisert ble følgende karakteriseringsteknikker benyttet: XRD, N₂-fysisorpsjon, SEM, ICP-MS, FTIR, and XAS.

En modifisert versjon av syntesen rapportert av Kong et.al¹, hvor mesoporer ble dannet av enten cetyltrimetylammonium hydroksid(CTAOH) eller glucose ga H/SAPO-34 som produkt. For å avgjøre om produkter var hierarkiske, sammenligning av N₂-fysisorpsjons resultater for H/SAPO-34 produkter og en hydrotermisk syntetisert konvensjonell SAPO-34 ble gjort. Produkter som ble klassifiserte som hierarkiske hadde mesopore volume rundt 0.20cm³/g, mens den konvensjonelle SAPO-34 prøven hadde et mesopore volum på 0.005cm³/g. H/SAPO-34 prøvene som ble testet for MTH hadde dårlig katalytisk ytelse og grunnen til dette var unormalt hurtig dannelse av koks, som deaktiverte prøven.

For syntese av H/CuSAPO-34 ble et bredt spekter av mesopore struktur dirigerende forbindelser(MeSDA) testet. Basert på N₂-fysisorpsjons resultater ble prøver der cetyltrimetylammonium bromid(CTAB) eller CTAOH var benyttet som MeSDA klassifisert som hierarkiske. H/CuSAPO-34 prøver syntetisert med CTAOH hadde lavere katalytisk aktivitet for HC-SCR sammenlignet med hydrotermisk syntetisert konvensjonell SAPO-34, der kobber også var prøvd inkorporert. For H/CuSAPO-34 syntetisert med CTAOH ble det også funnet at høyere kobber innhold gjorde at det katalytiske aktivitetsvinduet ble flyttet til lavere temperaturer. Fra XAS resultater ble det funnet at kobber enten ikke var inkorporert, eller i bestefall delvis inkorporert.

Table of content

ACKNOWLEDGEMENT	I
ABSTRACT	II
SAMMENDRAG	III
1 INTRODUCTION	1
2 THEORY	4
2.1 CONVENTIONAL SAPO-34 (C/SAPO-34)	4
2.2 METHANOL TO HYDROCARBONS (MTH)	6
2.3 HIERARCHICAL SAPO-34(H/SAPO-34)	6
2.4 COPPER CONTAINING SAPO-34	9
2.5 HC-SCR	10
2.6 CHARACTERIZATION METHODS	11
2.6.1 <i>X-ray diffraction (XRD)</i>	11
2.6.2 <i>Nitrogen-physisorption(N₂-physisorption)</i>	12
2.6.3 <i>Scanning electron microscopy (SEM)</i>	14
2.6.4 <i>Inductively coupled plasma mass spectrometry (ICP-MS)</i>	14
2.6.5 <i>Infrared spectroscopy (IR-spectroscopy)</i>	15
2.6.6 <i>X-ray absorption spectroscopy (XAS)</i>	15
3 EXPERIMENTAL	21
3.1 SYNTHESIS	21
3.1.1 <i>Part 1: Syntheses without copper</i>	21
3.1.2 <i>Part 2: Syntheses with copper</i>	26
3.2 CHARACTERIZATION AND CATALYTIC TESTING	31
3.2.1 <i>X-ray diffraction (XRD)</i>	31
3.2.2 <i>N₂-physisorption</i>	31
3.2.3 <i>Scanning electron microscopy(SEM)</i>	32
3.2.4 <i>Inductively coupled plasma mass spectrometry (ICP-MS)</i>	32
3.2.5 <i>CO-adsorption</i>	33
3.2.6 <i>Methanol to hydrocarbon (MTH)</i>	34
3.2.7 <i>Hydrocarbon selective catalytic reduction (HC-SCR)</i>	34
3.2.8 <i>X-ray absorption spectroscopy (XAS)</i>	35

4	RESULTS.....	38
4.1	X-RAY DIFFRACTION(XRD)	38
4.1.1	<i>Conventional SAPO-34</i>	38
4.1.2	<i>H/SAPO-34: Initial synthesis with CTAB</i>	39
4.1.3	<i>H/SAPO-34: varying CTAOH content</i>	39
4.1.4	<i>H/SAPO-34: varying crystallization temperature and time</i>	41
4.1.5	<i>H/SAPO-34: glucose(GLU) and silver behenate(Agb) as MeSDA</i>	45
4.1.6	<i>H/Cu:SAPO-34</i>	46
4.1.7	<i>C/CuSAPO-34</i>	47
4.1.8	<i>H/CuSAPO-34: varying MeSDA</i>	49
4.1.9	<i>H/CuSAPO-34: CTAOH as MeSDA, with Varying Cu and Si content</i>	53
4.2	N ₂ -PHYSISORPTION.....	55
4.2.1	<i>C/SAPO-34 and H/SAPO-34</i>	55
4.2.2	<i>C/CuSAPO-34 and H/CuSAPO-34</i>	59
4.2.3	<i>H/CuSAPO-34: CTAOH as MeSDA with Varying Cu and Si content</i>	63
4.3	SCANNING ELECTRON MICROSCOPY(SEM)	69
4.3.1	<i>H/SAPO-34</i>	69
4.3.2	<i>C/CuSAPO-34 and H/CuSAPO-34</i>	69
4.4	ICP-MS.....	71
4.5	CO-ADSORPTION	73
4.5.1	<i>H/SAPO-34</i>	73
4.5.2	<i>C/CuSAPO-34 and H/CuSAPO-34</i>	75
4.6	MTH.....	77
4.6.1	<i>H/SAPO-34</i>	78
4.6.2	<i>C/CuSAPO-34 and H/CuSAPO-34</i>	80
4.7	XAS.....	83
4.7.1	<i>XANES</i>	84
4.7.2	<i>EXAFS</i>	88
4.8	HC-SCR	93
5	DISCUSSION	97
5.1	HIERARCHICAL SAPO-34 WITHOUT COPPER	97
5.2	HIERARCHICAL SAPO-34 WITH COPPER.....	100

6	CONCLUSION.....	104
7	FURTHER WORK.....	106
8	REFERENCES.....	107

Appendix A: Synthesis

Appendix B: Additional XRD

Appendix C: Additional SEM

Appendix D: XAS

Appendix E: Additional HC-SCR

1 Introduction

The reduction of NO_x-emissions has, for several decades, been on the worlds agenda. The ratification of agreements such as the Gothenburg protocol² in 1999 by major global actors, has shown the desire to reduce emission of NO_x, among other compounds. This willingness to set ever more stringent goal for NO_x-emissions has borne fruit, with the total NO_x emissions for European countries being halved since 1990³. However, the lofty goals set are not easily achieved and further reducing NO_x-emissions becomes more challenging by the year. With the Volkswagen scandal in recent memory, it is clear that more work is needed if the global goals are to be achieved.

The reason such great effort has been made to reduce NO_x-emissions is the adverse effect it has on human health and the environment. NO_x-gases are inherently toxic, leading to increased risk of respiratory and cardiovascular diseases⁴. Reaction of NO_x also leads to formations photochemical smog and acid rain, which both can be detrimental to human health and the environment⁵. These effects combined make a compelling argument for the reduction of NO_x-emissions.

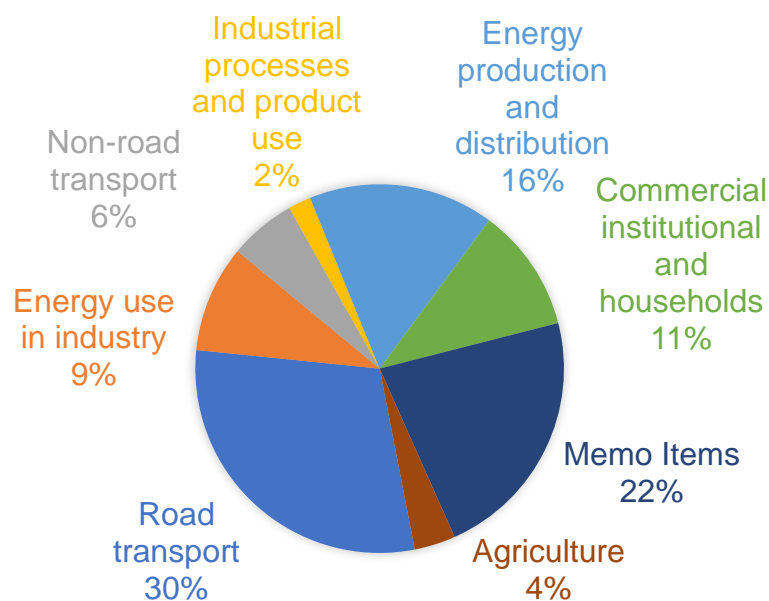


Figure 1-1: shows the sources of NO_x-emission for 33 European countries in 2015, based on the data from European Environment Agency³.

To evaluate where the greatest reductions in NO_x emissions can be made, an inspection of the sources of NO_x is valuable. In *Figure 1-1* the sources of NO_x in Europe are presented. The first thing to note is the memo items portion of pie chart. This section is mainly made up of international shipping and aviation emissions, and depending on the inventory, is not always

considered when a countries total emission is reported⁶. International shipping in Europe makes up 16% of the total emissions⁷, while the largest contributor to NO_x emissions in Europe is road transport with 30%. With shipping and road transport making up such a large fraction of the emissions, reductions here will have a large impact.

The NO_x emitted for shipping and road transport is generated during the high temperature combustion process⁸. This occurs for both petrol and diesel engines, but higher amounts of NO_x are emitted for diesel engines⁹. This is due to the effectiveness of the three-way catalyst, which is installed for most petrol engines. There is currently no comparable solution for diesel engines. There are however promising solutions, selective catalytic reduction(SCR) being one of them.

The basic principle behind SCR is for a reductant to be used, in conjunction with a catalyst, to reduce NO_x to N₂. Most research conducted uses either ammonia(NH₃) or hydrocarbons(HC) as the reductant. Of the two, NH₃-SCR is the more developed technique, being used in and most medium- and heavy-duty diesel vehicles since 2010¹⁰. However, the technique has a clear drawback, in that the NH₃ needs to be injected into the exhaust, and a tank of NH₃ is therefore required. For mobile sources the need for an NH₃-tank is suboptimal, and the possibility of NH₃-leaks is another concern¹¹. This is where HC-SCR has its main advantage, in that the exhaust from diesel engines contain enough HC to theoretically reduce all NO_x¹¹. Because of this consideration, HC is the reductant which is used in this project.

The most important component needed for HC-SCR to work is the catalyst itself. The catalysts that early on showed most promise were metal containing zeotypes¹², and much work has therefore been conducted on these type of materials. Copper containing SAPO-34 was one of the zeotypes that early on proved its value as a HC-SCR catalyst¹³⁻¹⁴, and research is still ongoing today¹¹.

Recent improvements of the catalytic properties of copper containing SAPO-34 for HC-SCR has been made by introduction of mesopores into the SAPO-34 structure¹⁵. The basic idea behind introducing mesopore into SAPO-34 is to improve diffusion properties, since diffusion often is the limiting step for zeolites and zeotypes¹⁶. This give the SAPO-34 a structure containing micro and mesopores, and these types of structures are commonly referred to as hierarchical materials. Currently, the introduction of copper into hierarchical SAPO-34 has only been achieved by ion exchange¹⁵. However, copper can also be introduced into SAPO-34 by isomorphous substitution, which has the benefits of better control of copper content and requiring fewer synthesis steps compared to ion exchange.

The main goal of this thesis is therefore to synthesise hierarchical SAPO-34 with copper introduced by isomorphous substitution, for use as a HC-SCR catalyst. The approach taken to reach this goal, is to first synthesise hierarchical SAPO-34 without copper, and subsequently modifying this synthesis. The synthesis of hierarchical SAPO-34 is therefore set as a secondary goal of the thesis.

To evaluate the syntheses, the samples have been characterised by X-ray diffraction(XRD), N₂-physisorption, inductively coupled plasma mass spectrometry(ICP-MS), scanning electron microscopy(SEM), infrared spectrometry(IR), and X-ray absorption spectroscopy(XAS). For promising samples catalytic testing has been performed. The HC-SCR was the focus of most of the catalytic testing, however some samples were tested as catalyst for the methanol to hydrocarbon(MTH) reaction.

2 Theory

In this section the properties of conventional and hierarchical SAPO-34 and methods of introducing copper into SAPO-34 is presented. The section also contains theory related to the MTH reaction, HC-SCR, and characterisation techniques used.

2.1 Conventional SAPO-34 (C/SAPO-34)

SAPO-34 is a zeotype containing silicon(Si), aluminium(Al), and phosphor(P) tetrahedrally coordinated to oxygen. Zeotypes are related to the more well know zeolites, which are only made up of Si and Al. The tetrahedrally coordinated atoms in both zeolites and zeotypes are commonly called t-atoms, due to their coordination. These tetrahedra are linked to form periodic repeating structure, which can contain pores and cages of various sizes and orientations¹⁷.

Zeotypes are classified based on the framework structure and the properties of the pores. The International Zeolite association recognises 235 unique framework types¹⁸. Porous structures are also commonly classified as micro-, meso- or macro-porous. Micropores are pores smaller than 2nm, mesopores are in the range 2-50nm, and macropores are larger than 50nm¹⁷. Microporous zeolites are further classified as small-, medium-, large-, or extra-large-pore zeolites. Small pores are limited by 8-membered rings, medium pores are limited by 10-membered rings, large pores are limited by 12-membered rings, and extra-large pores are limited by rings larger than 12-membered rings¹⁹. Further the pore system is defined as one-, two or three-dimensional, depending on the spatial orientation of the pores.

SAPO-34 is microporous and is classified as a three-dimensional small pored zeotype. It has a chabazite framework type, which is built up of distorted hexagonal prisms linked together by four membered rings to form ellipsoidal cages²⁰. The cages have a diameter of 7.5Å and a height of 8.2Å. Eight-membered rings, with a diameter of 3.8Å²⁰, link together cages and form the three-dimensional pore network. A depiction of the cage and pores, collected from VESTA(Visualization for Electronic and Structural Analysis)²¹, are shown in Figure 2-1, with the blue spheres represent T-atoms and the red spheres represent oxygen. The pore structure of SAPO-34 give rise to a high specific surface area, with specific surface areas of 550 m²/g being common.

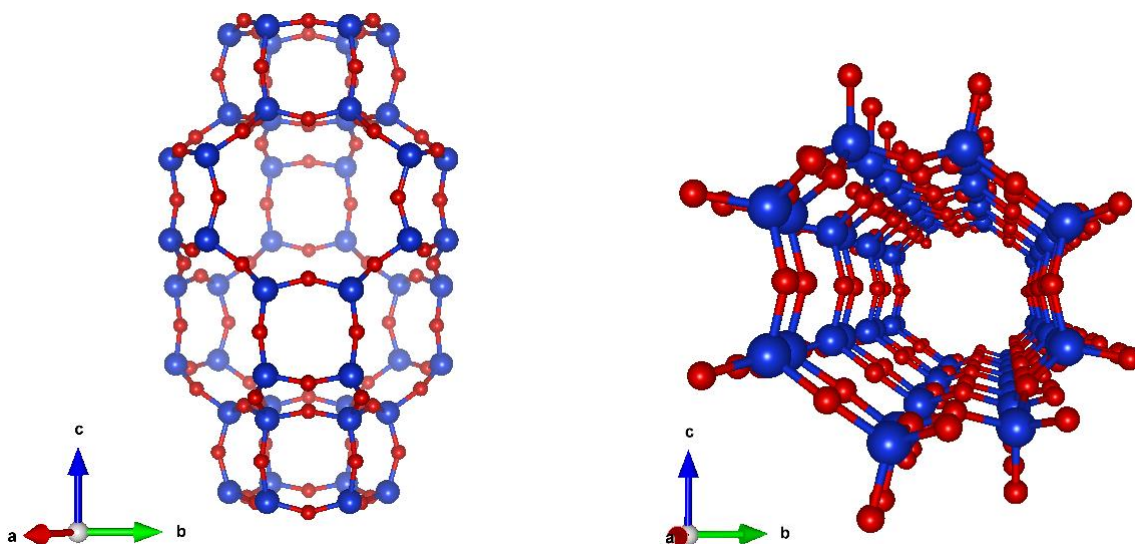


Figure 2-1: Show the cage(left) and the 8-membered pores(right) that are found in SAPO-34. The compass show from which direction the figure is viewed from. The figures collected from VESTA(Visualization for Electronic and Structural Analysis)²¹

In the SAPO-34 the framework has net negative charges, which can be thought of as arising from Si substituting P in the framework²². The negative charge is commonly balanced by a proton giving rise to a Bronsted acid site as seen in Figure 2-2. The strength of the Bronsted acid sites depend on the local environment¹⁷.

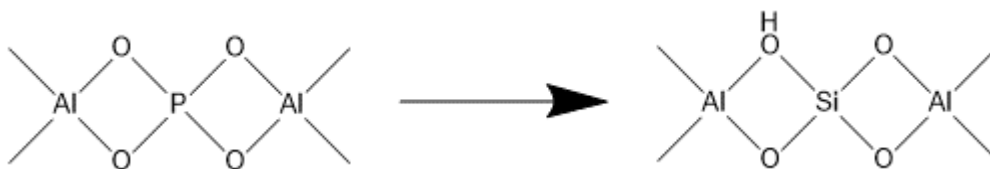
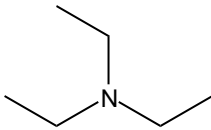
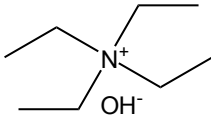
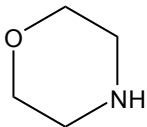
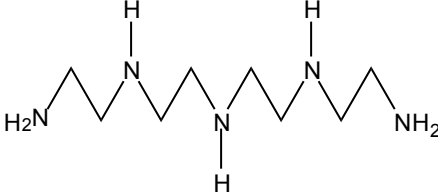


Figure 2-2: The Bronsted acid sites generated when P is substituted with Si

The synthesis of SAPO-34 is done by hydrothermal synthesis under autogenous pressure, using organic structure directing agents(SDA)²³⁻²⁴. The framework of SAPO-34 forms around the SDA which can be removed by calcination, giving rise to the micropore network. There is currently more than 20 SDA that has been used to successfully synthesise SAPO-34, with some of the more commonly used shown in Table 2-1²⁵.

Table 2-1: Name, abbreviation, and structure of some SDAs used to synthesise SAPO-34

Name	Abbreviation	Structure
Triethylamine	TEA	
Tetraethylammonium hydroxide	TEAOH	
Morpholine	MOR	
Tetraethylenepentamine	TEPA	

2.2 Methanol to hydrocarbons (MTH)

SAPO-34 is known to be a good catalyst for the methanol to hydrocarbon reaction²⁶, due to acid sites catalysing the reaction. In the MTH reaction, SAPO-34 also shows good selectivity towards lighter olefins²⁷. The selectivity of SAPO-34 towards lighter olefins, arise from micropores only being able to accommodate products below a certain size. The selectivity unfortunately has its drawback, since products that are too large to exit the structure eventually forming coke that clogs up the pores, and thus deactivate the catalyst²⁸. However, the deactivation appears to be lessened for hierarchical SAPO-34²⁹.

2.3 Hierarchical SAPO-34(H/SAPO-34)

In hierarchical SAPO-34 mesopores are introduced in addition to the micropores already present. This is meant to improve the intracrystalline diffusion, which is a slow process in micropores, and can often be the limiting step in reactions³⁰. With increased diffusion, reactants and products are retained for shorter times, and there is a smaller chance of coke formation³⁰.

Improvement of diffusion will also lead to higher catalytic activity for reactions where intracrystalline diffusion is the limiting step. Diffusion limitations occur when the rate of adsorption of reactants and/or the desorption of products is lower than the intrinsic reaction rate³¹. As a measure of the intracrystalline diffusion limitations the Thiele modulus(ϕ), given by equation (1), is commonly reported. Low values of Thiele modulus indicate that the rate of diffusion is high compared to the intrinsic reaction rate, which leads to a high volume of the catalyst being utilized. Conversely, a high Thiele modulus means that a small volume of the catalyst being utilized¹⁶.

$$\phi = \frac{r_{intrinsic}}{r_{diffusion}} = L \sqrt{\frac{k_v}{D_{eff}}} \quad (1)$$

Lowering the value of the Thiele modulus can be done by either shortening the diffusion length(L) or increasing the effective diffusivity(D_{eff})¹⁶. The introduction of mesopores is meant to increase the overall D_{eff} , since the diffusivity in mesopores are several orders of magnitude higher than in micropores¹⁶. However, for this to occur, the mesopores and micropores need to have a favourable connectivity.

The different types of connectivity that can occur in hierarchical systems are shown in Figure 2-3¹⁶. Figure 2-3b shows an interconnected hierarchical system, where the voids between the particles are designated as mesopores. This form of hierarchical system occurs for very small crystallites. In Figure 2-3c and Figure 2-3d the mesopores are intraconnected, meaning that the mesopores are within the crystallites, also known as intracrystalline. In Figure 2-3c the mesopores are accessible from the crystallite surface, while in Figure 2-3d the mesopores are entirely in the interior of the crystallite, and thereby not accessible from the crystallite surface.

The types of hierarchical connectivity which decrease the Thiele modulus are the interconnected and intraconnected with access to the crystallite surface. Mesopores that occur entirely in the interior of the crystallite will not decrease the Thiele modulus, since diffusion has to occur through micropore to get to the mesopores, which is the opposite of what is wanted.

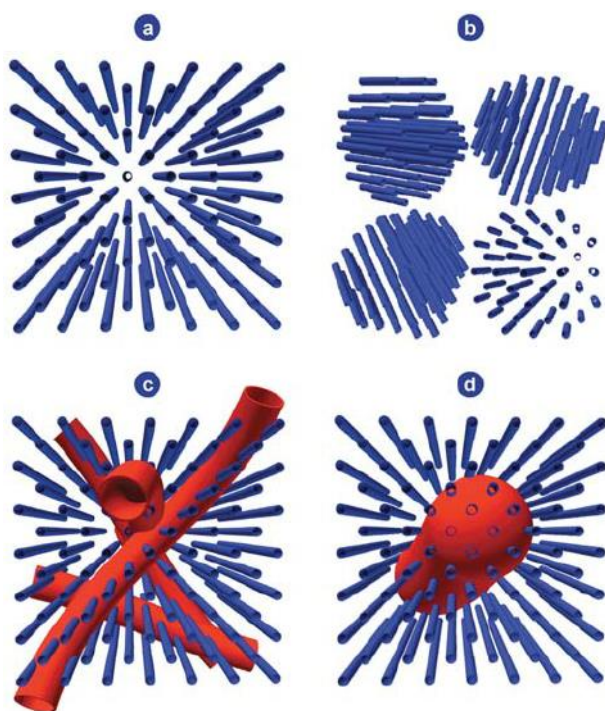


Figure 2-3 : Depiction of different types hierarchical connectivity. a) Shows a purely microporous material, b) Shows an interconnected hierarchical material, c,d) Shows two intraconnected hierarchical materials. The blue signifies micropores and red signifying mesopores. Reproduced from Pérez-Ramírez et.al.¹⁶ with permission from The Royal Society of Chemistry.

To create the mesopores two general approaches exist: top down and bottom up³⁰. For the top down approach the mesopores are created by post synthetic modifications³⁰, such as dry gel conversion²⁹. In the bottom up approach the mesopores are introduced during the synthesis by addition of a mesoporous structure directing agent (MeSDA), examples being saccharides³² and carbon nanotubes³³. For this project the bottom up approach is used, with MeSDA generated by large organic molecules, such as cetyltrimethylammonium bromide (CTAB). CTAB is a surfactant with an ammonium cation head group and the chemical structure shown in Figure 2-4, which has been used to successfully synthesise H/SAPO-34 by Kong et.al.¹.

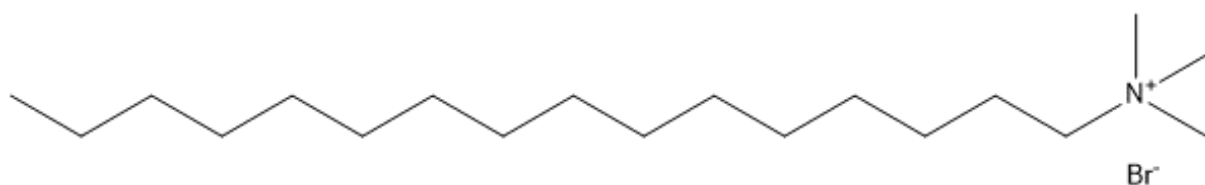


Figure 2-4: The chemical structure of CTAB.

2.4 Copper containing SAPO-34

To create copper containing SAPO-34, the copper can be introduced by impregnation, ion exchange, or incorporation. Ion exchange results in the Bronsted acid sites being replaced by copper cations, while incorporation entails copper taking the place of a T-atom in the framework²⁰. For this thesis impregnation is not relevant and will not be presented.

Ion-exchange is conducted by stirring SAPO-34 in a Cu^{2+} -solution. Ideally this should only replace the Bronsted acid sites with Cu^{2+} and leave the framework unaltered. It is however not uncommon for irreversible hydrolysis to occur during ion-exchange, due to H_2O attacking the Si-O-Al^{34} , with a resulting reduction in surface area³⁵.

Copper incorporation can be accomplished by modifying the synthesis by adding copper, commonly termed a one-pot synthesis³⁶. Incorporation results in copper becoming a part of the framework and when replacing Al additional Bronsted acid sites arise as seen in Figure 2-5.

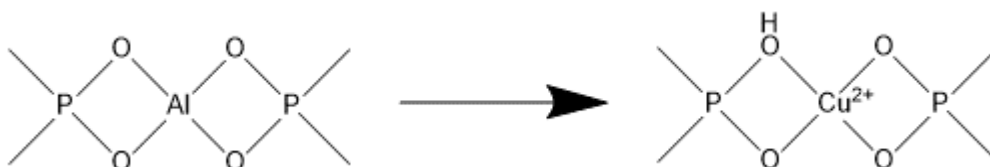


Figure 2-5: The Bronsted acid sites generated when Al is substituted with Cu^{2+} .

The framework atoms in SAPO-34 are tetrahedrally coordinated, and this is not the preferred coordination of copper(II). Commonly copper(II) adopts a tetragonally distorted octahedral coordination³⁷. Coupled with the larger ionic radius of copper compared to the atoms it replaces, the incorporation of copper is not trivial³⁸.

Additional difficulties for incorporating copper arise due to interactions between the SDA and copper. Amines are commonly used as SDA for synthesis without copper, but complications can occur for syntheses with copper. In the syntheses of SAPO-5 and SAPO-11 containing copper, amines have been shown to reduce Cu(II) to Cu(I) at temperature above 190°C , with the Cu(I) subsequently undergoing disproportionation to metallic Cu and Cu(II) ³⁹. Still, there has been successful syntheses of SAPO-34 with incorporated copper using amines as the SDA⁴⁰⁻⁴¹. For hierarchical samples the requirement of an additional SDA can also hinder the incorporation of copper.

2.5 HC-SCR

Currently there exists no ideal solution for reduction of NO_x from diesel engines. The three-way catalytic converter(TWC) is used to reduce the NO_x generated in petrol engines, but due to high air to fuel ratios in diesel exhaust, it is not an option for diesel engines¹⁷.

Selective catalytic reduction(SCR) is one approach that has been utilized for reduction of NO_x from coal power plants since 1981⁴². The basic principle behind SCR is to use a reductant to reduce NO_x , and to make the reaction go at appreciable rate, a catalyst is needed. For coal power plant, ammonia(NH_3) is used as the reductant⁴², and this is also the case for most medium- and heavy-duty diesel vehicles since 2010¹⁰. During NH_3 -SCR, equivalent amounts of NH_3 and NO reacts⁴³, with the NH_3 supplied from a tank. The need for a NH_3 -tank is not a big concern for power plants, but for mobile sources it is suboptimal. The success of NH_3 -SCR hinges on the driver of the vehicle refilling the NH_3 -tank, once empty. This may be fine for professional drivers, where a company can be held accountable, but for personal vehicles enforcement would be far more difficult. In addition, the possibility of NH_3 -leaks is another concern associated with NH_3 -SCR¹¹.

Fortunately, hydrocarbon selective catalytic reduction(HC-SCR) offers a more elegant solution for mobile sources. HC-SCR utilizes HCs already present in the exhaust as the reductant, thereby removing the need for a tank of reductant. The exhaust of lean burn engines, such as diesel engines, contains 0.05% NO_x , 5-10% O_2 , 10% H_2O and 0.05-0.1% HCs, which means that there is sufficient HCs to theoretically reduce NO_x completely to N_2 ¹¹. HC-SCR is also enhanced by the presence of oxygen, and proceeds even when water and SO_2 are present⁴⁴, making the reaction well suited for reduction of NO_x from lean burn engines.

However, for HC-SCR to become commercially viable the catalyst needs to fulfil certain requirements. The catalyst needs to be reasonably active for exhaust temperatures reached during operation. For diesel engines in trucks the exhaust temperature is between 100-200°C during idling and can reach 500°C during full throttle⁴⁵. The catalyst should also be active when water is present, and not be deactivated by SO_2 , which is present in diesel fuel⁴⁵. Finally, the catalyst should have a good lifetime, which is a measure of how long a catalyst can operate above an activity threshold.

The catalysts that initially showed the potential of HC-SCR was ZSM-5 ion exchanged with transition metals¹². ZSM-5 ion exchanged with copper(Cu :ZSM-5) was particularly promising, having reasonably high activity in the temperature range needed for diesel engines¹². Further

test also proved the catalyst suffered very little deactivation in the presence of SO₂⁴⁶. However, under realistic reaction conditions with water, Cu:ZSM-5 showed a poor lifetime⁴⁷, which is due to Cu:ZSM-5 having poor hydrothermal stability⁴⁸. The requirement for a more hydrothermally stable catalyst support was met by SAPO-34. SAPO-34 ion exchanged with copper(Cu:SAPO-34) was shown to sustain high activity for a prolonged period in the presence of water¹³. Further work has also indicated that hierarchical Cu:SAPO-34(H/Cu:SAPO-34) perform better than their conventional counterparts for HC-SCR¹⁵.

2.6 Characterization methods

In this section the characterisation techniques used are presented. For each technique the relevant theory and information that can be extracted from the techniques is given.

2.6.1 X-ray diffraction (XRD)

X-ray diffraction (XRD) is a bulk sampling technique used for analysis of crystalline materials. The technique works by irradiating a compound with X-rays, which then are scattered by the electrons in the compound. The scattered X-rays then hit a detector which measures their intensity. At certain angles of incidence (θ) given by Bragg's law:

$$2d\sin\theta = \lambda \quad (2)$$

constructive interference occurs, and a higher intensity is detected. This constructive interference arises due to crystal planes with a specific interplanar separation (d). Therefore, by varying the angle of incidence a diffractogram can be created showing intensity plotted against incidence angle. These diffractograms can be used to determine chemical composition and the crystal structure of the analyte.⁴⁹

In this thesis, XRD is used to determine whether SAPO-34 has been synthesised and to qualitatively evaluate crystallinity. This is done by comparing diffractograms of samples with the diffractogram of chabazite(CHA) shown in Figure 2-6. Since SAPO-34 is an isomorph of chabazite, the diffractogram of SAPO-34 will be the same as for chabazite. Whether the sample is hierarchical or contains copper, incorporated or ion exchanged, should not lead to any changes in the diffractogram.

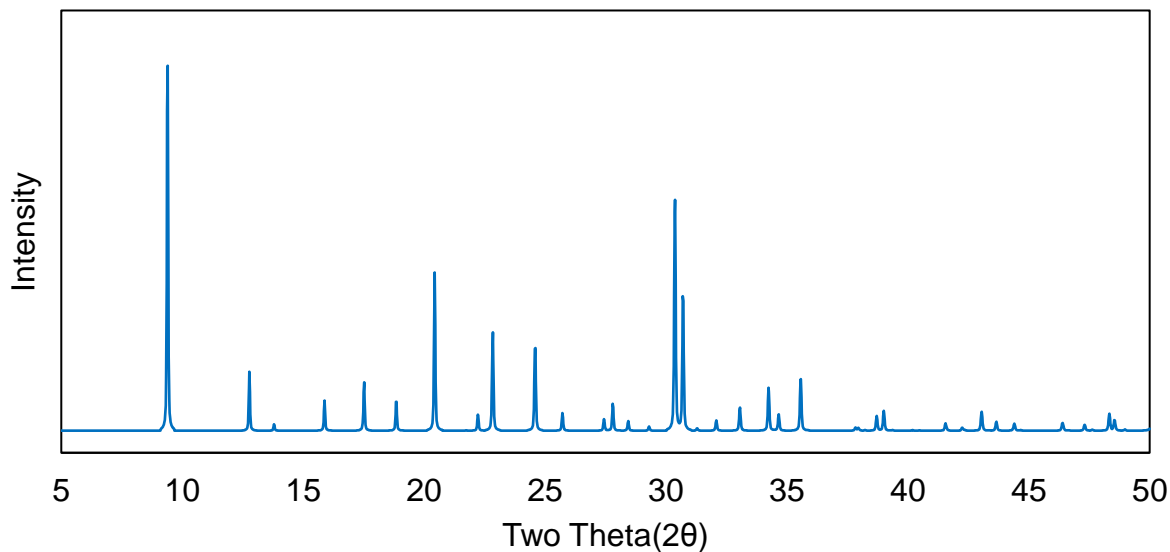


Figure 2-6: The calculated powder diffractogram of chabazite(CHA) obtained from the database of zeolite structure.¹⁸

2.6.2 Nitrogen-physorption(N₂-physorption)

Nitrogen physisorption(N₂-physorption) is conducted to obtain information about the surface areas and pore structure of materials. This is done by adsorbing nitrogen (N₂) to a known amount of sample, at liquid nitrogen temperatures. From this an adsorption-desorption isotherm can be generated, with amount of N₂ adsorbed per mass of solid plotted against the relative pressure of the gas. There are six common types of isotherms, shown in Figure 2-7. The isotherms of importance here are type 1,2, and 4. Type-1 isotherms are seen for microporous solids, such as conventional SAPO-34. In this case the pores are filled at low relative pressure. Type-2 isotherms are seen for non-porous solids. Type-4 isotherms are found for mesoporous solid, with the hysteresis occurring due to capillary forces during adsorption and desorption⁵⁰.

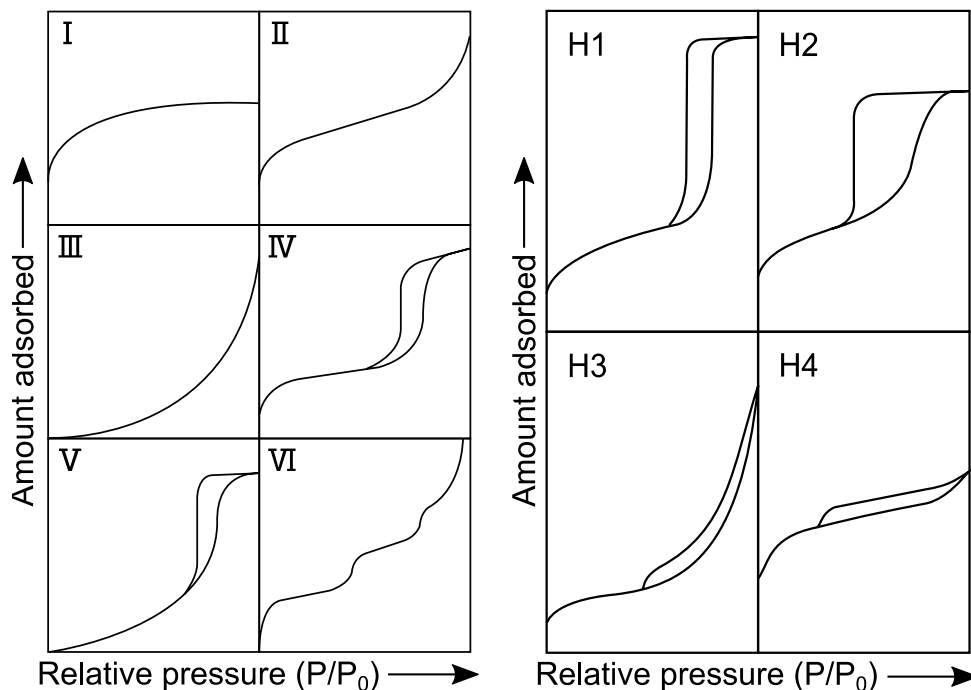


Figure 2-7: Shows the six types of isotherms (left) and the four types of hysteresis (left). Figures adapted from article by sing et al⁵⁰.

The hysteresis that occurs in mesoporous solids can have different shapes and are classified as seen in Figure 2-7. H1 hysteresis occurs in well-defined pore structures with narrow pore size distribution. H2 hysteresis are common in inorganic oxides, where there are varied pore sizes and shapes. H3 hysteresis are seen in aggregates of plate-like particles. While H4 hysteresis are common in adsorbents with slit-shaped pores in the micropore range⁵¹.

Quantitative information, such as surface areas and pore volumes can be obtained by utilizing the BET theory and t-plot method. The BET theory models the adsorbed species as forming multiple layers and the total surface area is calculated from the amount adsorbed at monolayer coverage¹⁷. A good estimate of total pore volume can be obtained by calculating the volume of gas adsorbed at high relative pressure, since the pores can be assumed to be completely filled at this point. From the t-plot method, the micro and mesopore fractions making up the surface area and pore volume can be obtained. The basic concept behind the t-plot method is to convert the isotherm to a thickness plot and comparing with the thickness plot of a non-porous reference. The differences can be attributed to the presence of micropores and used to calculate the microporous fraction of the surface area and pore volume. The mesopore fractions of surface area and pore volume can be calculated from the difference between total and the micropore fractions⁵². In addition, the pore size distribution is obtained from the physisorption model created by Barret, Joyner and Halenda (BJH).

N₂-adsorption-desorption isotherms, in combination with BET theory, t.plot and BJH methods, can be used to evaluate if a sample is hierarchical, and to a certain extent how the mesopores are ordered if present. Hierarchical samples have been shown to have a combination of type 1 and type 4 isotherm^{1, 29}. Further, the type of hysteresis that occurs can tell if the pores are ordered or disordered and give an indication of the pore size distribution⁵⁰. More information about the pore size distribution can be obtained from the BJH method. In addition, hierarchical samples show a large mesopore fraction of both surface area and pore volume^{1, 53}, and this will also be used to evaluate whether a sample is hierarchical. Finally, it is important to keep in mind that results N₂-physorption is similar for intra- and inter-crystalline hierarchical materials, and are therefore not distinguishable by N₂-physorption¹⁶.

2.6.3 Scanning electron microscopy (SEM)

Scanning electron microscopy can be used to obtain high resolution, high magnification images of samples. The images are generated by an electron beam striking the sample, while a second electron beam strikes a cathode ray tube(CRT). The impact of the electrons on the sample lead to a variety of electron and photon emission, with one type of emission chosen and detected. A signal is generated from the striking of the sample and this is used to modulate the brightness of the second beam. A strong signal lead to a bright spot on the CRT, and conversely a weaker signal leads to a dimmer spot. The two electron beams simultaneously scans the sample and the CRT, and a picture of the area scanned is thereby generated⁵⁴.

What type of emission is chosen to generate the images depend on the desired result. For generating images for topological analysis, secondary electrons are most commonly measured. Secondary electrons being electrons that are inelastically scattered by the sample⁵⁴.

The sample preparation needed for SEM is normally minimal, however some additional sample preparation is needed for non-conducting sample. The additional sample preparation comes in the form of applying a thin conducting film, often of gold or carbon⁵⁴.

SEM is used to evaluate the morphology and crystallite size of the samples. The crystallite size and morphology of C/SAPO-34 varies with synthesis procedure used²⁵, but the crystallite size close to 1 μ m⁵⁵. From knowing the crystallite size for H/SAPO-34 and H/CuSAPO-34 samples it can be determined whether the samples are intra- or inter-connected hierarchical materials.

2.6.4 Inductively coupled plasma mass spectrometry (ICP-MS)

ICP-MS is a highly sensitive analytical technique, with the capability to quantify most elements in a relatively short amount of time. The technique works by first ionising argon gas, and

thereby generating a plasma. The analyte is then introduced into the plasma and ions of the constituent elements are created. The ions created then pass into the mass spectrometer, where the different ions can be distinguished based on their mass to charge ratio(m/z).

In this thesis ICP-MS is used to determine the amount of Cu in the sample, as well as the ratios between the T-atoms that make up the SAPO-34.

2.6.5 Infrared spectroscopy (IR-spectroscopy)

IR-spectroscopy is used to obtain information regarding molecular vibrations. Molecular vibrations are excited by IR-radiation, and by measuring absorbance or transmittance while varying the wavelength of the IR-radiation, an IR-spectra is obtained.

For zeolites and zeotypes framework peaks are found in the regions $350-1250\text{cm}^{-1}$ and $3500-38000\text{cm}^{-1}$, arising from framework vibrations and stretching vibrational modes of hydroxyl groups, respectively⁵⁶⁻⁵⁷. For this project the hydroxyl groups are of interest, or more specifically the Bronsted acid sites. The peaks arising from Bronsted acid site are found in the region $3500-3650\text{cm}^{-1}$, while terminating P-OH, Si-OH and Al-OH groups are found at 3676cm^{-1} , 3742cm^{-1} , and 3748cm^{-1} , respectively⁵⁶⁻⁵⁷.

The Bronsted acid sites are commonly probed using CO. The CO molecules interact with acid sites leading to a shift of the stretching frequency from 2138cm^{-1} for free CO to higher values. The magnitude of the shift depends on the acid sites CO-interacts with. Conversely the frequency of the acid sites is shifted to a lower frequencies, and the magnitude of this shift is proportional to the acid strength⁵⁷.

This technique will be used to determine the types of acid sites present in SAPO-34 and their strength. For SAPO-34 were incorporation of copper is attempted, IR measurements can be used to discern whether this was done successfully, since framework copper can give rise to unique Bronsted acid sites⁵⁸.

2.6.6 X-ray absorption spectroscopy (XAS)

X-ray absorption spectroscopy (XAS) is an element-specific technique which gives information about a target element and its local environment⁵⁹. The method is based on X-rays exciting or ejecting core electrons.

The X-ray source needs to provide tuneable high energy X-rays, and this is commonly achieved by using a synchrotron as the source. A synchrotron works by accelerating electrons around a large loop. The loop is made up of alternating straight and curved sections. To make the

electrons follow the curved sections magnets bend the electron beam. The bending of the electron beam leads to an energy loss, and this energy loss is given off as X-rays⁶⁰. The X-rays generated travel down straight paths called beamlines. Prior to reaching the sample the X-rays are focused and a monochromator picks out X-rays of appropriate energy⁶¹.

The XAS measurements are conducted by quantifying the absorption of X-rays while the photon energy is increased in small increments. The absorption measurements can be done in transmission, with the linear absorption coefficient (μ) given by this equation:

$$\mu(E) = \log \frac{I}{I_0} \quad (3)$$

where I_0 and I is the intensity of the incident and transmitted X-ray beams respectively⁵⁹. With these measurements conducted as the photon energy is increased an XAS spectra can be plotted, like the one for a metallic copper foil shown in Figure 2-8.

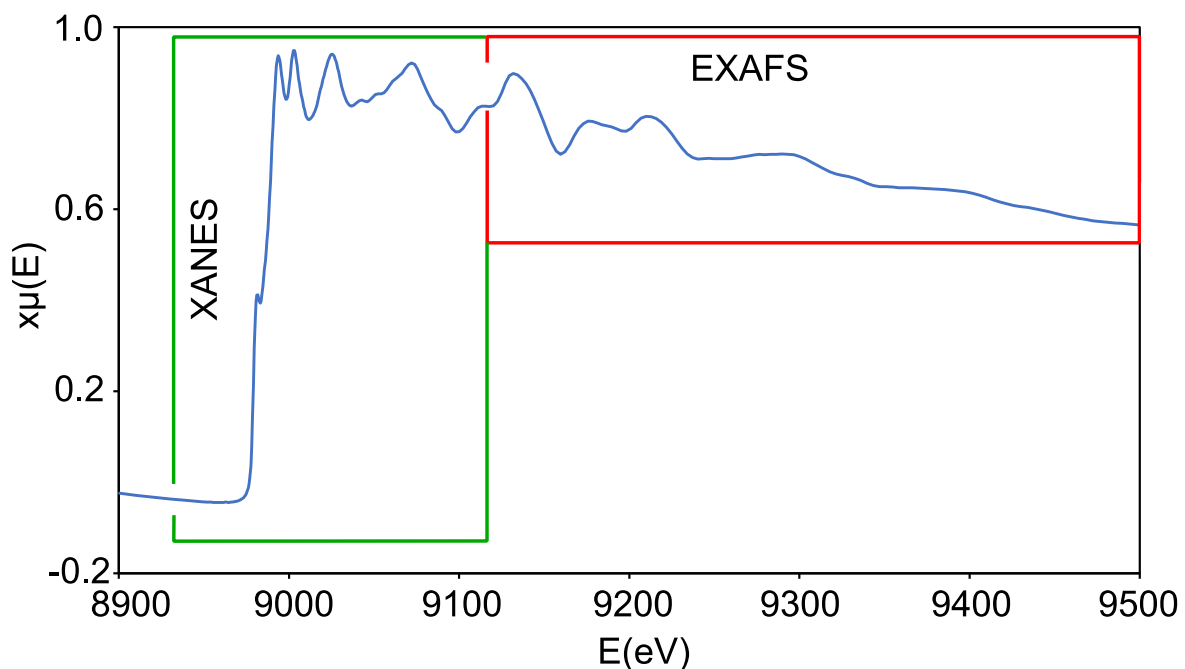


Figure 2-8: Show the XAS spectra of metallic copper, with the XANES and EXAFS regions highlighted

The XAS spectra is commonly divided into two regions; the X-ray absorption near edge structure (XANES) and the extended X-ray absorption fine structure (EXAFS). The XANES region is commonly defined so as to include any pre-edge features to 150eV above the main absorption edge, where the edge is the sharp rise in the spectrum, and the EXAFS region is in the region 150-1000eV above the absorption edge.

2.6.6.1 X-ray absorption near edge structure (XANES)

XANES gives information about the oxidation state and coordination environment⁵⁹. In Figure 2-9 the XANES of the metallic copper foil, Cu₂O and CuO are shown. The first thing to note is the feature that occurs halfway up the absorption edge. In Cu₂O this is seen as a pronounced peak, called a pre-edge, which arises from the 1s-4p excitation. This transition is dipole allowed and is therefore a prominent feature in the XANES in Cu(I) complexes⁶². For metallic copper and CuO this feature is much less prominent.

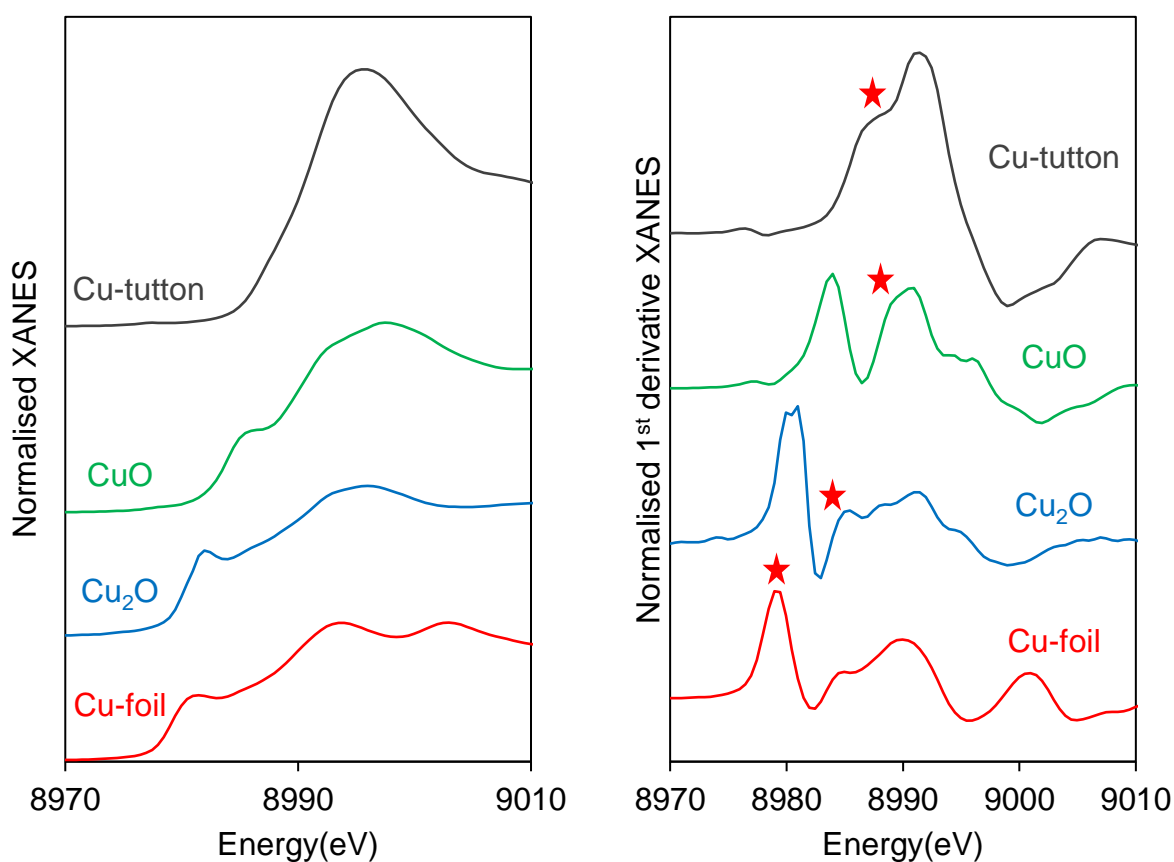


Figure 2-9: Show the normalized XANES of the Cu-foil, Cu₂O, CuO, Cu-tutton standards (left) and the derived XANES for the same standards (right), with E₀ marked with a star

The next feature is the absorption edge itself. The edge depicted in Figure 2-9 is the copper K-edge, which arises from the ejection of a 1s as a photoelectron. The edge energy, E₀, is the energy needed for this ejection to occur. For most elements E₀ is designated half way up the normalized XANES, but since copper compounds often displays pre-edges and shoulder features in this region, E₀ needs to be designated differently. The convention used here is shown for the derived XANES of four copper standards in Figure 2-9. E₀ for Cu-foil is designated as

the first peak in the derived XANES, while for Cu₂O, CuO and Cu-tutton it is designated as close to halfway up the normalized XANES, but after the pre-edge.

XANES will be used to determine the oxidation state and coordination of copper in SAPO-34. This is done by comparing the XANES of samples with the references shown in Figure 2-9.

2.6.6.2 Extended X-ray absorption fine structure (EXAFS)

The EXAFS can give information about the local environment, such as bond lengths, coordination number, and identity of neighbouring atoms. The oscillations that are the EXAFS can be understood by Fermi's Golden rule. When the X-rays pass through the sample there are several events can occur, such as, absorption, scattering and transmission. Fermi's golden rule states that the likelihood of any one of the events occurring, depends on the similarity between the original state and state after the event. The greater the similarity the more likely the event is to occur⁶³.

In the event where the x-rays eject a core electron, the photoelectron can be thought of as a wave. This wave travels radially outward from the absorber and can be backscattered off neighbouring atoms, as seen in Figure 2-10. This leads to an interference phenomenon, where the outgoing photoelectron wave can interact either constructively or destructively with the backscattered wave. If constructive interference occurs there will be higher electron density at the absorber atom, the system will be more like the atom prior to absorption, and the likelihood of absorption will be more likely as stated by Fermi's golden rule. The opposite effect occurs when destructive interference finds place⁶³.

Whether the interference is constructive or destructive depends on the photoelectron energy, which is approximately equal to $(E_{h\nu} - E_0)$, with $E_{h\nu}$ being the X-ray energy. The interference also depends on the absorber-backscatterer distance, the number of shells and the coordination number. A shell is atoms of the same type at equal distance from the absorber, and coordination number is the number of atoms in a shell. Each shell gives rise to its own sinusoidal components and the EXAFS is therefore a sum of these oscillations⁶⁴.

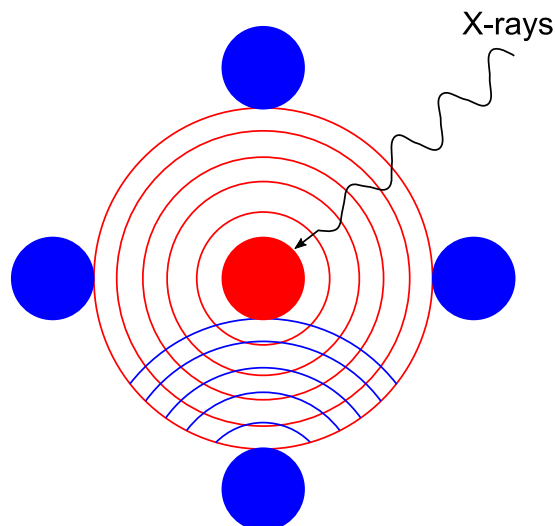


Figure 2-10: Shows the absorption of X-rays (black line), the ejection of a photoelectron (red circles), and the backscattered photoelectrons (blue circles).

The structural data contained in the EXAFS cannot be obtained directly from an XAS spectra, and several steps are needed to extract the information. The first step is to isolate the EXAFS portion, which is termed χ , of the XAS spectrum, and convert the energy to wavenumbers(k). In addition, a k weighting is added to offset the decay of the EXAFS oscillations at high k values, with k^3 -weighting being common⁶⁴. These steps give a plot like the one shown in Figure 2-11 for a metallic copper foil. Fourier transforming this plot gives a pseudo radial distribution function(PRDF), also seen in Figure 2-11. The peaks in the PRDF correspond to shells at a certain radial distance. The actual distance is slightly lower than what is seen in the PRDF, but it is still a good visualization of the local environment around the absorber⁶⁴.

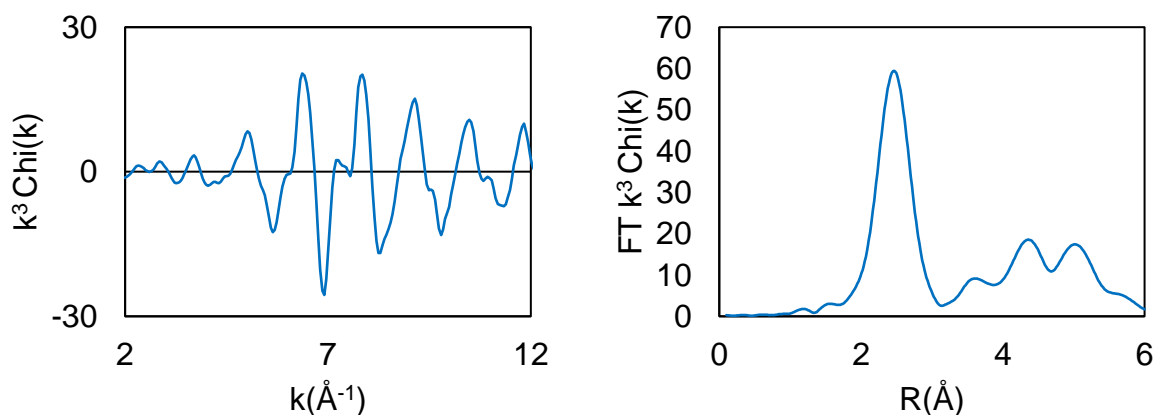


Figure 2-11: Shows the Chi(left) and FT(right) plots for metallic copper.

The next step in extracting structural data from the EXAFS is trying to fit a curve to the Chi curve. The fitting equation is called the EXAFS equation and is given below⁶⁴:

$$k^n \chi(k) = k^{n-1} \sum_j \frac{N_j}{r_j^2} F_j(k) S_i(k) e^{-2k^2 \sigma_j^2} e^{-\frac{2r_j}{\lambda(k)}} \sin(2kr_j + \phi_{ij}(k)) \quad (4)$$

- j : The j^{th} shell.
- N_j : The coordination of the j^{th} shell.
- r_j : The distance between the absorbing atom and backscatterers in the j^{th} shell.
- $F_j(k)$: The backscattering amplitude function of the j^{th} shell.
- $S_i(k)$: Amplitude reduction factor.
- $2\sigma_j^2$: Debye Waller factor for the j^{th} shell.
- $\lambda(k)$: Inelastic electron mean free path.
- $\phi_{ij}(k)$: Total phase shift.

This is a complicated equation and it is not possible to solve analytically. When EXAFS analysis is done, there are commonly 5 parameters that are varied to obtain the best fit. These are absorber-scatterer distance(r_j), degeneracy(N_j), Debye Waller factor ($2\sigma^2$), amplitude reduction factor ($S_i(k)$), and the fermi energy (E_F). In the case of a single scattering paths, meaning that the photoelectron is scattered directly back to the absorber, r_j is the average distance between absorber and scatterer in the j^{th} shell, and N is the average coordination number of the j^{th} shell. These two factors are in these cases constrained based on the bond distances and coordination numbers that can occur between the atoms of the sample. The Debye-Waller factor is a measure of the variance of r_j due to static and thermal disorder. It commonly adopts values between 0.002-0.03 Å². $S_i(k)$ can be thought of as the loss of amplitude in the EXAFS due to intrinsic effects, such as the adjustment of the remaining electrons in the absorber due to the formation of the core hole. The values are commonly between 0.7 and 1.05⁶³. E_F is a correction to the E_0 value and can take on positive and negative values, normally in with absolute value between 10-20eV.

EXAFS will be used to determine the local environment around copper in the copper containing SAPO-34. EXAFS will be very important for determining whether the copper has been incorporated into the framework or if other copper species is present.

3 Experimental

3.1 Synthesis

The syntheses done in this project are divided into the two following parts:

- Part 1: Syntheses without copper, which encompasses conventional SAPO-34(C/SAPO-34) and hierarchical SAPO-34(H/SAPO-34).
- Part 2: Synthesis with copper, which encompasses hierarchical SAPO-34 ion exchanged with copper (H/Cu:SAPO-34), conventional SAPO-34 with incorporated copper (C/CuASPO-34) and hierarchical SAPO-34 with incorporated copper (H/CuSAPO-34).

The parts are structure with the general synthesis and ion exchange procedures presented first followed by the specific syntheses that were done. In the sections regarding specific syntheses, the mole fraction is given and any alterations to the general synthesis is stated, while amounts of chemicals added can be found in appendix A. All chemicals used were acquired from Sigma Aldrich.

Some clarification about the naming scheme is in order. The names start with *C/* if the sample is conventional and */H* if it is hierarchical. The next part of the name states relevant synthesis information, such as MeSDA used, MeSDA mole fraction, Si mole fraction and crystallisation conditions. If copper is present in the sample this will be the ending of the name, together with its mole fraction. For as prepared samples */AP* will be added to the end of the name, while for calcined samples no ending will be used.

3.1.1 Part 1: Syntheses without copper

The synthesis used to make most *C/SAPO-34* and *H/SAPO-34* samples was based on the work done by Kong et.al¹. However, there were some samples made with a modified version of a different synthesis. For these samples it will be clearly stated that a different synthesis was used, and the section detailing the synthesis will be given.

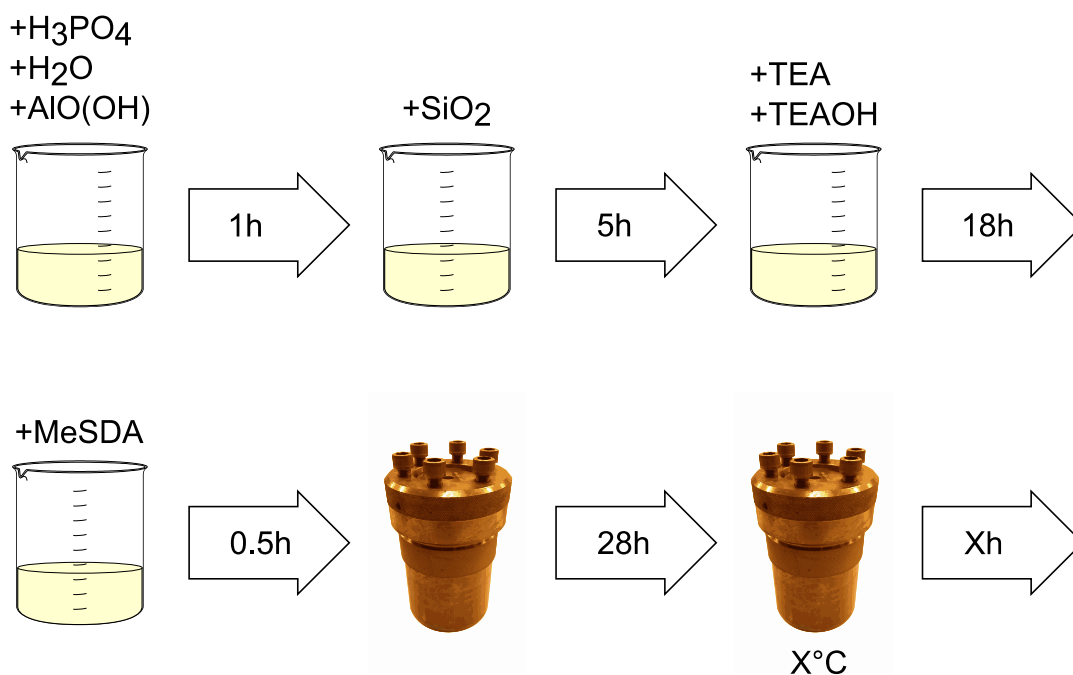


Figure 3-1: Synthesis procedure for C/SAPO-34 and most H/SAPO-34 samples.

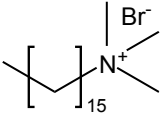
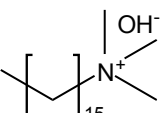
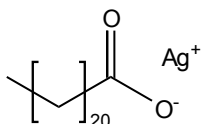
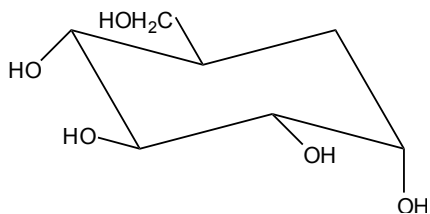
The synthesis procedure is depicted in Figure 3-1, where chemicals added are shown above the beakers and the duration of each step given in the arrows. For a typical synthesis, phosphoric acid (H_3PO_4 , 85wt%, 7.96g) was diluted with the deionized water (H_2O , 100wt%, 31.5g), followed by the gradual addition of pseudoboehmite ($\text{AlO}(\text{OH})$, 72.8wt%, 4.9g) with continuous stirring. The solution was left to stir for an hour before the colloidal silica (SiO_2 , 40wt%, 3.11g) was added and this solution was stirred for another 5 hours. Triethylamine (TEA, 100wt%, 6.98g) and tetraethylammonium hydroxide (TEAOH, 40wt%, 2.54g) was added and the solution was stirred for approximately 18 hours. Finally, the MeSDA was added and the solution was transferred to a stainless-steel autoclave with a Teflon liner and aged for 28 hours at ambient temperature. The masses given above yields a molar composition of:



The solution was then crystallized at temperatures in the range 150-200°C for between 48-120h. The gel was then washed in de-ionized water and centrifuged four times, dried overnight at 70 °C and then crushed in a mortar. Finally, the dried gel was calcined at 550 °C for six hours to remove SDA residues.

The chemical formula and concentrations of MeSDA used for synthesis of H/CuSAPO-34 is shown in Table 3-1. A different synthesis procedure was used for H/SAPO-34 made with silver behenate or glucose as the MeSDA.

Table 3-1: Chemical structure of MeSDA used to synthesise H/CuSAPO-34.

Name	Abbreviation (concentration)	Structure
Cetyltrimethylammonium bromide	CTAB (100wt%)	
Cetyltrimethylammonium hydroxide	CTAOH (0.127M)	
Silver Behenate	Agb (98wt%)	
Glucose	GLU (100wt%)	

3.1.1.1 Conventional SAPO-34(C/SAPO-34)

To have a basis of comparison for the H/SAPO-34 samples, a single C/SAPO-34 sample was synthesised. This was done using the general synthesis presented above, with the one alteration being the omission of MeSDA. The sample was crystallised at 200°C for 72h and had a molar composition of

Al : 0.85P : 0.26Si : 0.85TEA : 0.086TEAOH : 26H₂O

The sample name used for this sample is C/Si0.26.

3.1.1.2 Hierarchical SAPO-34(H/SAPO-34)

The H/SAPO-34 samples made are grouped into the following four categories:

- Initial synthesis with CTAB
- Synthesis with varying amount of CTAOH
- Synthesis with CTAOH with varying crystallization times and temperatures.
- Synthesis with other MeSDAs

Initial synthesis with CTAB

The first H/SAPO-34 sample was synthesised using CTAB as the MeSDA. The sample was crystallised at 200°C for 72h and had a molar composition of:

Al : 0.97P : 0.39Si : 0.98TEA : 0.15TEAOH : 26H₂O: 0.01CTAB

The sample name given for this sample was H/CTAB0.01

Varying CTAOH amount

The next three syntheses used CTAOH as the MeSDA, and the mole fraction of CTAOH and water was varied. These samples were crystallised at 200°C for 72h and had a molar composition of:

Al : 0.85P : 0.26Si : 0.85TEA : 0.086TEAOH : xH₂O: yCTAOH

The samples names and the mole fraction of water and CTAOH is given in Table 3-2.

Table 3-2: Mole fractions that were varied for H/SAPO-34 samples made with CTAOH as the MeSDA

Sample name	H ₂ O/Al	CTAOH/Al
H/CTAOH0.004	27	0.004
H/CTAOH0.008	29	0.008
H/CTAPH0.0013	31	0.0013

Varying crystallization temperatures and time

The following H/SAPO-34 syntheses were done with varying crystallization time and temperature, with CTAOH being used as the MeSDA. The molar composition of these samples was:

Al : P : 0.3Si : TEA : 0.1TEAOH : 32H₂O: 0.005CTAOH

In Table 3-3 the samples names and their respective crystallization times and crystallization temperatures are shown.

Table 3-3: Crystallisation temperatures and times tested for syntheses using CTAOH as the MeSDA

Sample name	Crystallization temperature	Crystallization time
	[°C]	[h]
H/150°C-48h	200	48
H/150°C-72h	200	72
H/150°C-96h	200	96
H/150°C-120h	200	120
H/180°C-48h	180	48
H/180°C-72h	180	72
H/180°C-96h	180	96
H/180°C-120h	180	120
H/200°C-48h	150	48
H/200°C-72h	150	72
H/200°C-96h	150	96
H/200°C-120h	150	120

Other MeSDAs

Glucose and silver behenate were also tested as the MeSDA in the synthesis of H/SAPO-34. However, these differ from the other H/SAPO-34 sample in that a modified version the synthesis presented in 3.1.2 was used. The modifications made to this synthesis was the omission of Cu, and for the sample made with Agb, the beaker containing the synthesis mixture

was covered with aluminium foil to hinder photoreduction of silver. These samples were crystallised at 150°C for 120h and had a molar composition of:

Al : P : 0.3Si : TEPA 0.02 : 1.85MOR : 40H₂O: xMeSDA

In Table 3-4 the samples names and MeSDA mole fractions are given.

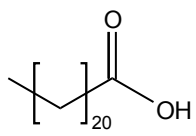
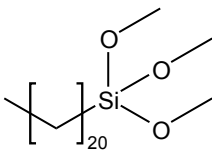
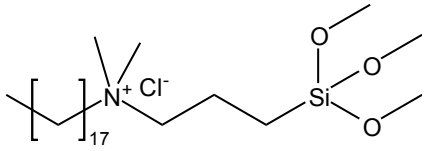
Table 3-4: Mole fractions of MeSDA used for syntheses of H/SAPO-34, using glucose or silver behenate as the MeSDA

Sample name	MeSDA	MeSDA/Al
H/GLU0.05	GLU	0.05
H/Agb0.03	Agb	0.03

3.1.2 Part 2: Syntheses with copper

The synthesis for C/CuSAPO-34 and H/CuSAPO-34 was adapted from the synthesis for H/SAPO-34. The changes made was the replacement of MiSDA, addition of copper, and removal of the aging. In addition to the MeSDA used for the synthesis of H/SAPO-34, the MeSDA shown in Table 3-5 were also tested for the synthesis of H/CuSAPO-34.

Table 3-5: Chemical structure of MeSDAs used exclusively for the syntheses of H/CuSAPO-34

Name	Abbreviation	Structure
Behenic acid	BA (100wt%)	
Trimethoxy(octadecyl)silane	TMODS (90wt%)	
Dimethyloctadecyl[3-(trimethoxysilyl)propyl]ammonium chloride	DMOAC (100wt%)	

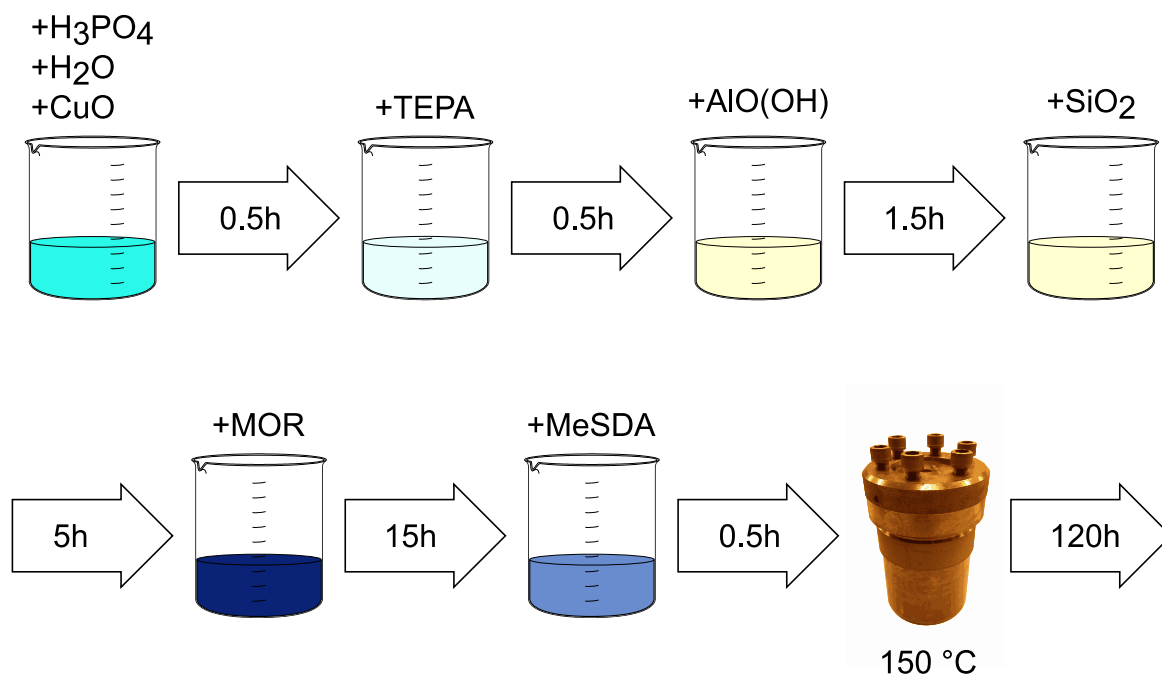


Figure 3-2: Synthesis procedure for H/CuSAPO-34 and C/CuSAPO-34, as well as H/SAPO-34 synthesised with glucose and silver behenate as the MeSDA.

The synthesis procedure is depicted in Figure 3-2, where chemicals added are shown above the beakers and the duration of each step given in the arrows. For a typical synthesis, copper oxide (CuO, 100wt%, 0.11g) was dissolved in phosphoric acid (H₃PO₄, 85wt%, 7.96g) which had been diluted with deionized water (H₂O, 100wt%, 45g), followed by addition of Tetraethylenepentamine (TEPA, 100wt%, 0.26g) all under continuous stirring. Then the pseudoboehmite (AlO(OH), 72.8wt%, 4.9g) was added gradually, left to stir for approximately one and a half hours, before the colloidal silica (SiO₂, 40wt%, 3.11g) was added and left to stir for a minimum of five hours. The morpholine (MOR, 100wt%, 11.12g) was then added, stirred overnight, before the MeSDA was added and the solution was transferred to a stainless-steel autoclave with a Teflon liner. The masses given above yields a molar composition of:



The solution was then crystallized at 150°C for 120 hours. The gel was then washed in deionized water and centrifuged four times, dried overnight at 70 °C and then crushed in a mortar. Finally, the dried gel was calcined at 550 °C for six hours to remove SDA residues.

Ion exchange

Copper ion exchange was done by first preparing a 0.03M copper(II)tetraamine solution. This was done by dissolving copper(II)nitrate($\text{Cu}(\text{NO}_3)_2$, 100wt%, 0.3607g) in deionized water (H_2O , 100wt%, 50mL). A 5M ammonia solution was prepared by diluting concentrated ammonia (NH_3 , 25wt%) with deionized water. This solution was then added dropwise to the $\text{Cu}(\text{NO}_3)_2$ solution until the solution had turned dark blue, indication formation of copper(II)tetraamine. The pH was measured to be 8.5 as a second confirmation of copper(II)tetraamine formation. In 15 mL of this solution 0.5g of H/SAPO-34 sample was added and left to stir for 24 hours at ambient temperature and with continuous stirring.

3.1.2.1 Hierarchical SAPO-34 ion exchanged with Cu(H/Cu:SAPO-34)

A selection of the H/SAPO-34 were ion exchanged with copper according to the ion exchange process described above. The samples that were ion exchange and their new sample names are given in Table 3-6.

Table 3-6: H/SAPO-34 samples that were ion exchanged and their new sample names.

Sample name	Original sample name
IE-H/CTAOH0.004	H/CTAOH0.004
IE-H/200°C-48h	H/ 200°C-48h
IE- H/180°C-72h	H/ 180°C-72h

3.1.2.2 C/CuSAPO-34

The C/CuSAPO-34 samples were made with the general synthesis for copper containing samples, with the only alteration being the omission of MeSDA. Si, Cu, and TEPA content was varied in these syntheses, while other mole fractions were kept constant and their values are shown in **Error! Reference source not found.** These samples were crystallised at 150°C for 120h and had a molar composition of:

Al : P : xSi : yCu : yTEPA : 1.85MOR : 40H₂O

In Table 3-7 the sample names and the values for the variable syntheses conditions are shown. The mole fraction of TEPA and Cu were kept identical for all syntheses and this is the only place where the TEPA mole fraction is explicitly stated.

Table 3-7: Mole fraction of Si, Cu and TEPA used for the synthesis of C/CuSAPO-34

Sample name	Si/Al	Cu/Al	TEPA/Al
C/Si0.3_Cu0.02	0.3	0.02	0.02
C/Si0.3_CuCu0.04	0.3	0.04	0.04
C/Si0.5_Cu0.04	0.5	0.04	0.04

3.1.2.3 H/CuSAPO-34

The H/CuSAPO-34 samples were made with the general synthesis for copper containing samples presented above and are divided into two groups:

- H/CuSAPO-34 made with various MeSDAs
- H/CuSAPO-34 made with CTAOH, with varying Cu, TEPA, and Si mole fractions.

All H/CuSAPO-34 sample were crystallized at 150°C for 120h.

Varying MeSDA

To determine possible MeSDA candidates a set of MeSDAs were tested. In these syntheses the only factor varied was the MeSDA and the molar composition was:

Al : P : 0.3Si : 0.02Cu : 0.02TEPA : 1.85MOR : 40H₂O : 0.05MeSDA

The samples names and MeSDA used is shown in Table 3-8.

Table 3-8: Sample names and the MeSDA used to make H/CuSAPO-34

Sample name	MeSDA
H/CTAB0.05_Cu0.02	CTAB
H/CTAOH0.05_Cu0.02	CTAOH
H/DMOAC0.05_Cu0.02	DMOAC
H/GLU0.05_Cu0.02	Glucose
H/TMODS0.05_Cu0.02	TMODS
H/BA0.05_Cu0.02	Behenic acid
H/Agb0.05_Cu0.02	Silver behenate

Varying Cu-, TEPA- and Si-content

Several syntheses of H/CuSAPO-34 were performed with CTAOH as the MeSDA and varying amounts of Cu, TEPA and Si mole fractions. The mole fraction for these samples was:

Al : P : xSi : yCu : yTEPA : 1.85MOR : 40H₂O : 0.01MeSDA

In Table 3-9 the sample names and the values of the variable mole fractions are shown. The mole fraction of TEPA and Cu were kept identical for all syntheses and this is the only place where the TEPA mole fraction is explicitly stated.

Table 3-9: Mole fraction of Si, Cu and TEPA used for the synthesis of H/CuSAPO-34, with CTAOH used as the MeSDA

Sample name	Si/Al	Cu/Al	TEPA/Al
H/Si0.3-Cu0.02	0.3	0.02	0.02
H/Si0.3Cu0.03	0.3	0.03	0.03
H/Si0.3Cu0.04	0.3	0.04	0.04
H/Si0.3-Cu0.05	0.3	0.05	0.05
H/Si0.3-Cu0.06	0.3	0.06	0.06
H/Si0.5-Cu0.02	0.5	0.02	0.02
H/Si0.5-Cu0.03	0.5	0.03	0.03
H/Si0.5-Cu0.04	0.5	0.04	0.04
H/Si0.5-Cu0.05	0.5	0.05	0.05
H/Si0.5-Cu0.06	0.5	0.06	0.06

3.2 Characterization and catalytic testing

3.2.1 X-ray diffraction (XRD)

For XRD-measurements a Bruker D8 A25 DaVinci X-ray diffractometer is used. The instrument has a Cu K α X-ray tube and a LynxEye™ SuperSpeed detector. Sample preparation is done by transferring the sample to a 25mm PMMA sample holder and ensuring that the powder surface is flat. Data was then collected between 5-75° using a variable divergence slit, which ensures that the same sample area is analysed for all angles. The resulting diffractograms were used to evaluate crystallinity and to determine phase purity by comparison with the diffractogram of chabazite.

3.2.2 N₂-physisorption

N₂-physisorption is performed on a Micromeritics Tri Star 3000 Area and Porosity Analyser. Prior to measurements the sample is degassed overnight in a Micromeritics VacPrep061 at

250°C, which is done to remove any adsorbed species. Subsequently, the sample mass of the sample is noted, and measurements were conducted.

From the measurement N₂ adsorption-desorption isotherms, total surface area, total pore volume, and the pore size distribution are obtained. The total surface area is calculated using the BET method, while the total pore volume is calculated from the amount of gas adsorbed at a pressure close to the saturation pressure. The pore size distribution is obtained in accordance with the BJH-method. In addition, the micropore and mesopore surface areas and pore volumes are obtained from the t-plot method. These results are together used to evaluate the porosity of a sample and evaluate whether a sample is hierarchical or not.

3.2.3 Scanning electron microscopy(SEM)

For SEM a Hitachi S-3400N variable pressure scanning electron microscope was used. The instrument has the capability of 300 000X magnifications and has both a backscattered electron detector (BSE) and a secondary electron detector (SED). Imaging was done using the SED, and the instrument then uses an Everhart-Thornley secondary electron detector.

Prior to imaging some sample preparation was necessary. Carbon tape was put on the sample holder and the sample was applied to the tape. Any excess sample was removed by air blown over the sample holder. The sample was then coated by carbon sputtering, which was done to lessen charging effect. The sample holder was then mounted in the SEM and the instrument was evacuated. The electron gun was subsequently turned on, using an acceleration voltage between 3-20eV.

3.2.4 Inductively coupled plasma mass spectrometry (ICP-MS)

ICP-MS elemental analysis was done on a High Resolution Inductively Coupled Plasma ELEMENT 2, connected to as mass spectrometer, by Syverin Lierhagen (IKJ). The primary purpose of this technique was to determine the amount of copper present in the samples, and secondarily to obtain the amounts of the T-atoms in the sample.

Samples were prepared by weighing out between 10-50mg of sample in a Teflon tube(25mL), and subsequently adding concentrated nitric acid (1.5mL) and concentrated hydrofluoric acid (0.5mL). The sample was decomposed for a minimum of 30min, before the solution was transferred to a larger Teflon container and diluted with between 230-250mL of deionised water. A Teflon tube(16mL) was then filled with this solution. In addition to the samples, three blanks were prepared without sample added.

3.2.5 CO-adsorption

CO-adsorption experiments were done using a vacuum cell, and the IR-measurements were performed on a VERTEX 80 FTIR spectrometer, using a liquid nitrogen cooled HgCdTe detector(LN-MCT). Sample preparation was done by pressing thin wafers of the sample and inserting these into a gold envelope. The envelope with the wafer was then transferred to the cell shown in Figure 3-3. The cell is then evacuated, and the sample heated to 500°C for 2 hours to remove any adsorbed species. The cell is subsequently cooled with liquid nitrogen and the sample is now ready for IR-measurements.



Figure 3-3: Show the cell used for CO-adsorption experiments

IR-measurements are made prior to any CO being introduced into the cell. Enough CO to saturate the Bronsted acid sites is then introduced into the cell and a IR-measurement is conducted. Desorption of CO is then done by evacuating the cell stepwise and conducting IR-measurements continuously.

3.2.6 Methanol to hydrocarbon (MTH)

The MTH reaction was conducted while continuously performing IR-measurements and using a GC-MS to analyse the gas after reaction. Diffuse reflectance infrared Fourier transform spectroscopy(DRIFTS) was the method used to obtain the IR-measurements and was conducted on a VERTEX 80 FTIR spectrometer, using a LN-MCT detector.

The sample was prepared by first pressing the sample into wafers. The wafers were gently mortared and sifted to obtain particle sizes between 212-425 μm , and a small sample holder was filled with the sifted sample, and the sample weight was noted. The surface of the sample was pressed flat to obtain a good signal during the DRIFTS measurements. The sample holder was mounted in a water-cooled DRIFTS cell and heated to 500°C in He, with a ramp rate of 5°C/min. The sample was held at 500°C for 2 hours to ensure complete dehydration of the sample.

The MTH reaction was then conducted by bubbling He through methanol, and subsequently over the sample. The flow of He was set so as to obtain a gas hourly space velocity(GHSV) of 7h⁻¹. During the reaction, IR-measurements were done continuously, and the GC-MS performed injections every 30mins. The reaction was continued until very low conversions were detected.

3.2.7 Hydrocarbon selective catalytic reduction (HC-SCR)

For the HC-SCR testing of samples the setup shown in figure was used. The gas mixture consisted of NO (2000ppm), propene (1200ppm), oxygen (2%) and helium or argon as the carrier gas. To obtain the correct concentrations, the gas flow of each individual gas was controlled by mass flow controllers(MFC). The flow of carrier gas was set to give a total gas flow of 30mL through the reactor.

Sample preparation for HC-SCR testing was done by first pressing the sample into wafers. The wafers were gently mortared and sifted to obtain particle sizes between 212-425 μm , and 0.03g of the sample was transferred to the reactor tube, with the sample being held in place by quartz wool. The reactor tube was then mounted in the tube-oven and heated to 500°C in Ar or He(4mL/min), with a heating rate of 0.5°C/min. The sample was then activated in oxygen (2%) for 1h, with a total gas flow of 30mL/min, and the sample was then ready for HC-SCR testing. The reaction was started at 500°C, reduced in 25°C increments, and ended at 275°C, with each temperature being held for 20min. The FTIR was set to continuously measure concentrations of reactants and potential products every 5min. In addition to measuring during reaction, the bypass concentration of reactants was measured prior to and after the reaction had been

conducted. This was done to determine the NO_x concentration when no reaction occurred and was used to calculate the conversion of NO_x.

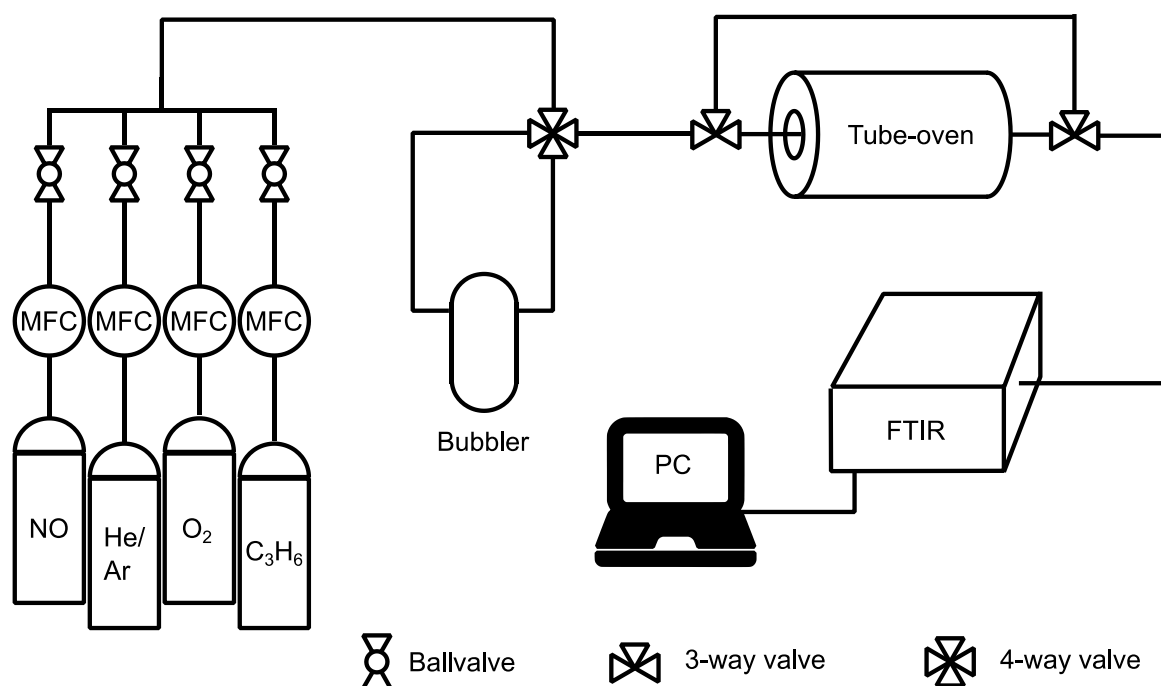


Figure 3-4: Shows the set-up used for HC-SCR catalytic testing

HC-SCR testing was done to determine the activity of samples and to a lesser extent, to determine what products were formed. The activity of samples can in turn be used to evaluate whether making hierarchical samples had the desired effect.

3.2.8 X-ray absorption spectroscopy (XAS)

XAS-measurements was performed at the Swiss-Norwegian Beam Lines(SNBL) BM31 beamline at the European Synchrotron Radiation Facility(ESRF) in Grenoble, France.

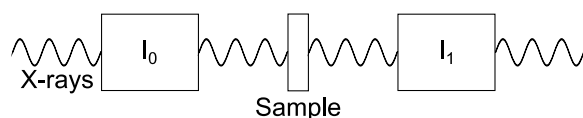


Figure 3-5: Transmission mode

Samples were run both In-situ and Ex-situ. For most Ex-situ measurements, samples were prepared by loading the sample into an aluminium sample holder, with the sample held in place by Kapton® tape. The exception was post DeNO_x samples which were pressed into wafers and taped with Kapton® tape to ensure the wafer remained intact. In both cases measurements were performed in transmission mode, as depicted in Figure 3-5.

For In-situ measurements wafers of the samples were prepared and these were then mortared and sifted to obtain appropriate particle sizes. The particles were transferred to a capillary (1.5mm) and held in place by quartz wool. The capillary was mounted in a sample holder connected to gas lines allowing gases to flow freely through the sample, with XAS measurements being performed simultaneously.

All measurements were done at the copper K-edge(8979eV) in transmission mode, with scans collected in the energy range 8.9-10keV, with a counting time of 300ms and a step length of 0.5eV.

For the temperature programmed reduction(TPR) three scans were conducted at room temperature in He(15mL/min), before the sample was heated to 670°C in H₂(15mL/min) with a heating rate of 3°C/min. During heating, shorter scans were collected in the energy range 8.9-9.6keV, with a counting time of 250ms and a step length of 0.5eV . Upon reaching 670°C three normal scans were collected.

3.2.8.1 Data analysis

The raw data obtained was reduced using the program Athena, which is part of the IFEFFIT package⁶⁵. The raw data is first converted to $\mu(E)$ and rebinned. The E_0 was then set as halfway up the normalised XANES. Any glitches were subsequently removed, and truncation was done from the point where the data became too noisy. Lastly the data was normalised between 30-150eV for XANES and from 150eV until the end of the scan for EXAFS. In addition to data reduction, Athena was also used for linear combination fitting, where reference scans are linearly combined to obtain the best fit with the scans of a sample.

After the data reduction, the EXAFS data was analysed in the program DL EXCURV. The program iteratively refines a theoretical EXAFS to the experimental EXAFS to obtain the best fit⁶⁶.

Prior to refinement, the atoms present in the samples are inputted, k^3 -weighting chosen, and the maximum R-value was set to 6Å. During refining, the program uses least square minimization in k-space to obtain the best fit⁶⁶. The parameters which can be refined are r , N and $2\sigma^2$ for each shell and the amplitude reduction factor($S_i(k)$), and the fermi energy(E_F) for the absorber atom. These parameters can be refined individually, or a combination of the parameters can be refined simultaneously. Refinement iterations are done until satisfactory agreement between theory and experimental data is obtained, and the quality of the fit is then reported as the R-factor⁶⁶.

EXAFS analysis was done for reference compounds and samples. The reference compounds were analysed to obtain a value for $S_i(k)$, for use in EXAFS analysis of samples. This was done by fixing N to known values, while r , $2\sigma^2$, and E_F was refined. Following completion of these refinements, $S_i(k)$ was then refined, and the value obtained was used for samples with similar oxidation state as the reference. For the samples all parameters were refined.

Fourier filtering was done to determine the type of backscattering in second shells. Fourier filtering extracts the contribution from a range in R-space, which is transformed back to k-space and can be refined⁶⁴.

4 Results

In this section the results of characterisation and catalytic testing will be presented. The techniques will be presented in the following order: XRD, N₂-physisorption, SEM, ICP-MS, CO-adsorption, MTH, XAS, HC-SCR. For each technique results for SAPO-34 without copper will be presented first, if the technique was applicable, followed by results for SAPO-34 with copper.

4.1 X-ray diffraction(XRD)

XRD was used mainly for fingerprint analysis, and to evaluate crystallinity to a lesser extent. The samples below are presented in the following order

- Conventional SAPO-34
- Hierarchical SAPO-34
- Copper ion exchanged SAPO-34
- Conventional SAPO-34 with incorporated copper
- Hierarchical SAPO-34 with incorporated copper.

4.1.1 Conventional SAPO-34

The diffractogram of C/Si_{0.26} is shown in **Error! Reference source not found.**, together with the diffractograms of CHA and AFI. The primary phase of the sample is chabazite, but there is also a secondary AFI phase as seen from the low intensity peak occurring at approximately 7.5°. The sample will still be used to compare the results obtained for the H/SAPO-34 samples, since the amount of AFI phase is very low.

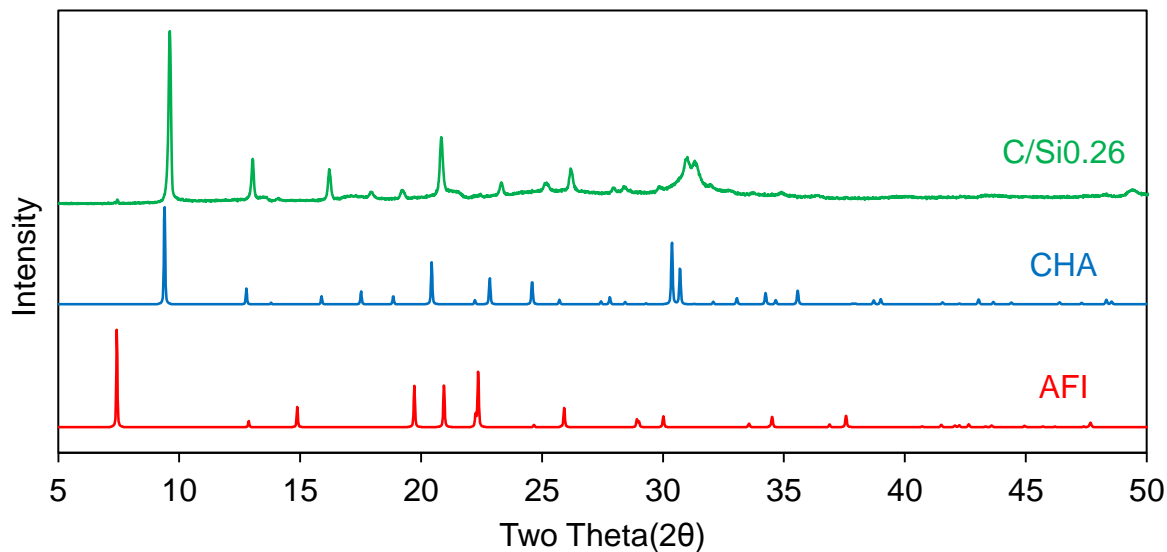


Figure 4-1: Diffractogram of CHA and C/Si_{0.26}

4.1.2 H/SAPO-34: Initial synthesis with CTAB

The initial synthesis of H/SAPO-34 used CTAB as the MeSDA and was crystallised at 180°C for 72h. This synthesis yielded phase pure SAPO-34 as can be seen from the diffractogram in Figure 4-2.

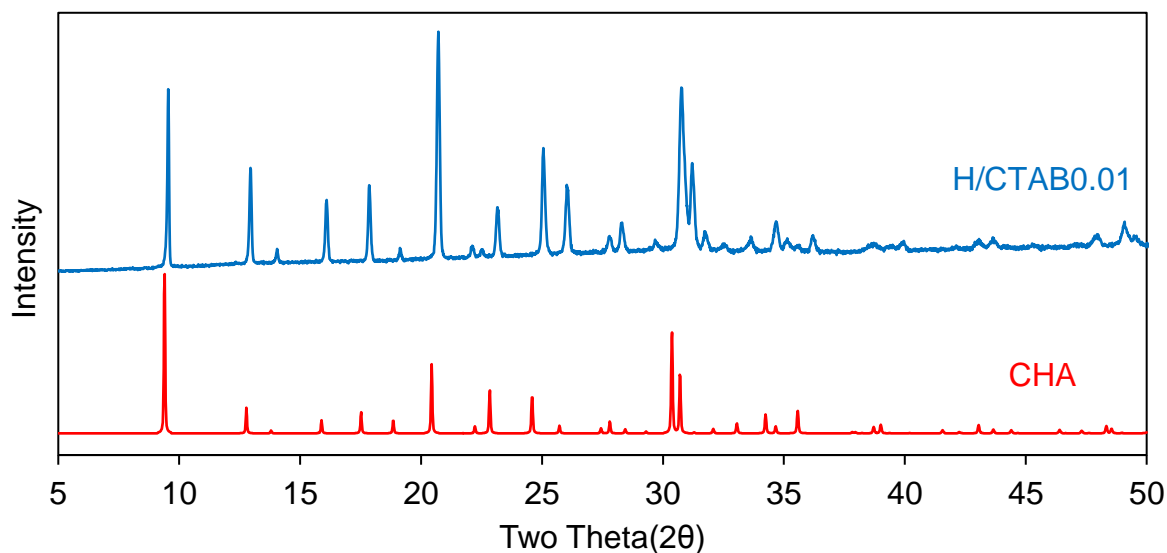


Figure 4-2: Diffractogram of CHA and H/CTAB_{0.01}

4.1.3 H/SAPO-34: varying CTAOH content

For the following H/SAPO-34 the MeSDA was changed from CTAB to CTAOH, and the effect of varying CTAOH content was examined. The change from CTAB to CTAOH was done in

anticipation of future syntheses containing copper. Ideally, only the CTAOH content would have been varied, but unfortunately water content was also varied. The change in mole fraction of water was small, and its effects are assumed inconsequential. These samples were crystallised at 200°C for 72h.

The result of the XRD analysis is summarised in Table 4-1, together with the CTAOH mole fractions. All samples had chabazite as their major phase, but they also contained a fraction of a secondary AFI-phase. This can be seen in Figure 4-3, where the peak that occurs at 7.5° arises due to the AFI phase. No further characterisation was therefore performed for these samples.

Table 4-1: XRD-results for H/SAPO-34 samples made with differing CTAOH-content

Sample name	CTAOH/Al	XRD-result
H/CTAOH0.004	0.004	CHA+AFI
H/CTAOH0.008	0.008	CHA+AFI
H/CTAOH0.0013	0.0013	CHA+AFI

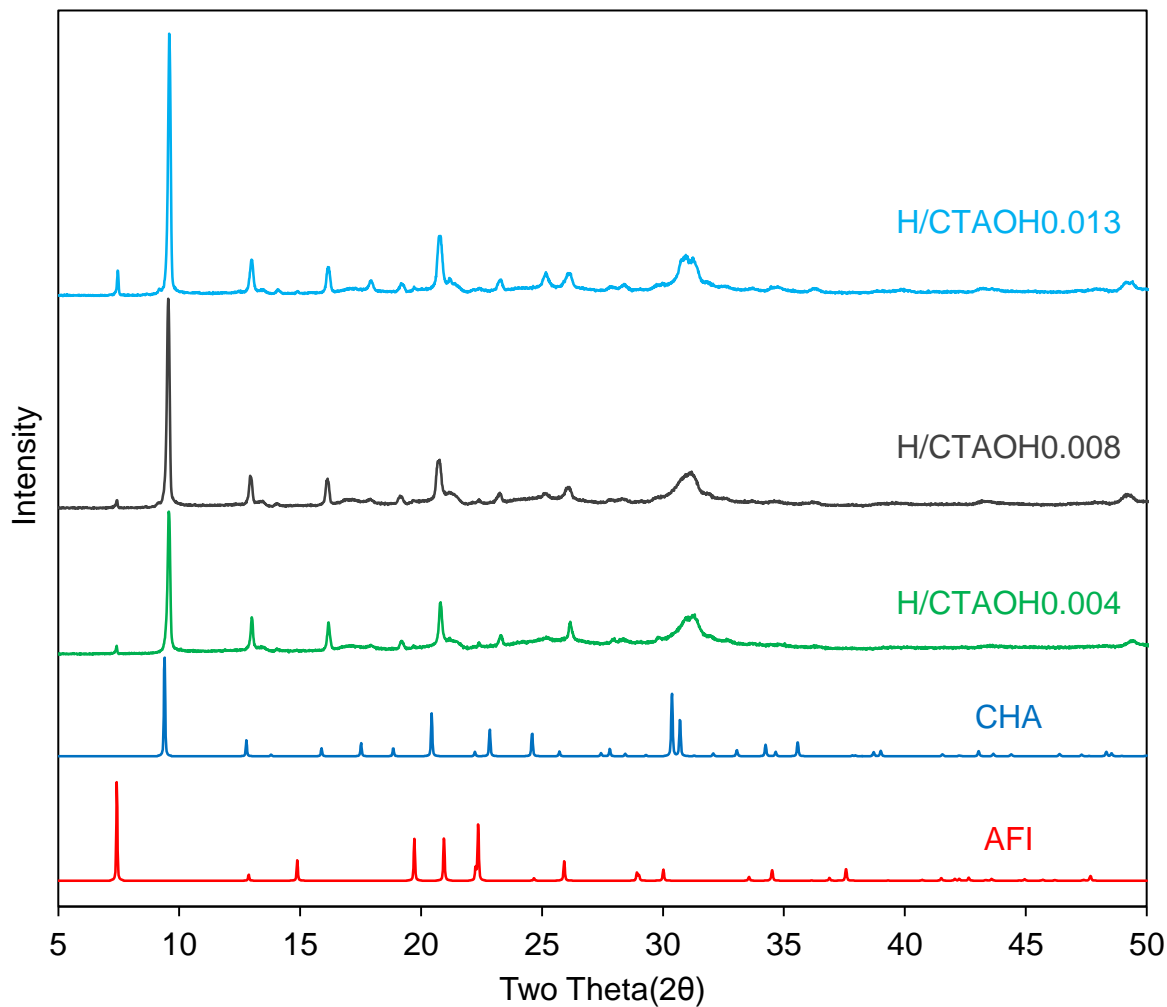


Figure 4-3: Diffractograms of AFI, CHA, and H/SAPO-34 samples synthesised with varying CTAOH content

4.1.4 H/SAPO-34: varying crystallization temperature and time

A parameter study was conducted, where crystallization temperature and time was varied, using CTAOH with a mole fraction of 0.005. The temperature and time combinations used are shown in Table 4-2, together with the result from the XRD analysis.

Table 4-2: Summary of the results obtained from XRD analysis for the crystallisation parameter study, with red signifying an amorphous product, yellow signifying a combination of chabazite and an AFI-phase, and green signifying phase pure SAPO-34.

Sample name	Crystallization temperature [°C]	Crystallization time [h]	XRD-result
H/150°C-48h	150	48	Amorphous
H/150°C-72h	150	72	Amorphous
H/150°C-96h	150	96	Amorphous
H/150°C-120h	150	120	CHA
H/180°C-48h	180	48	CHA
H/180°C-72h	180	72	CHA+AFI
H/180°C-96h	180	96	CHA+AFI
H/180°C-120h	180	120	CHA+AFI
H/200°C-48h	200	48	CHA
H/200°C-72h	200	72	CHA+AFI
H/200°C-96h	200	96	CHA+AFI
H/200°C-120h	200	120	CHA+AFI

The XRDs of the samples made with a crystallization temperature of 150°C are shown in Figure 4-4. At this temperature there is a clear trend of sample going from being almost completely amorphous to becoming phase pure SAPO-34 with increasing crystallisation times.

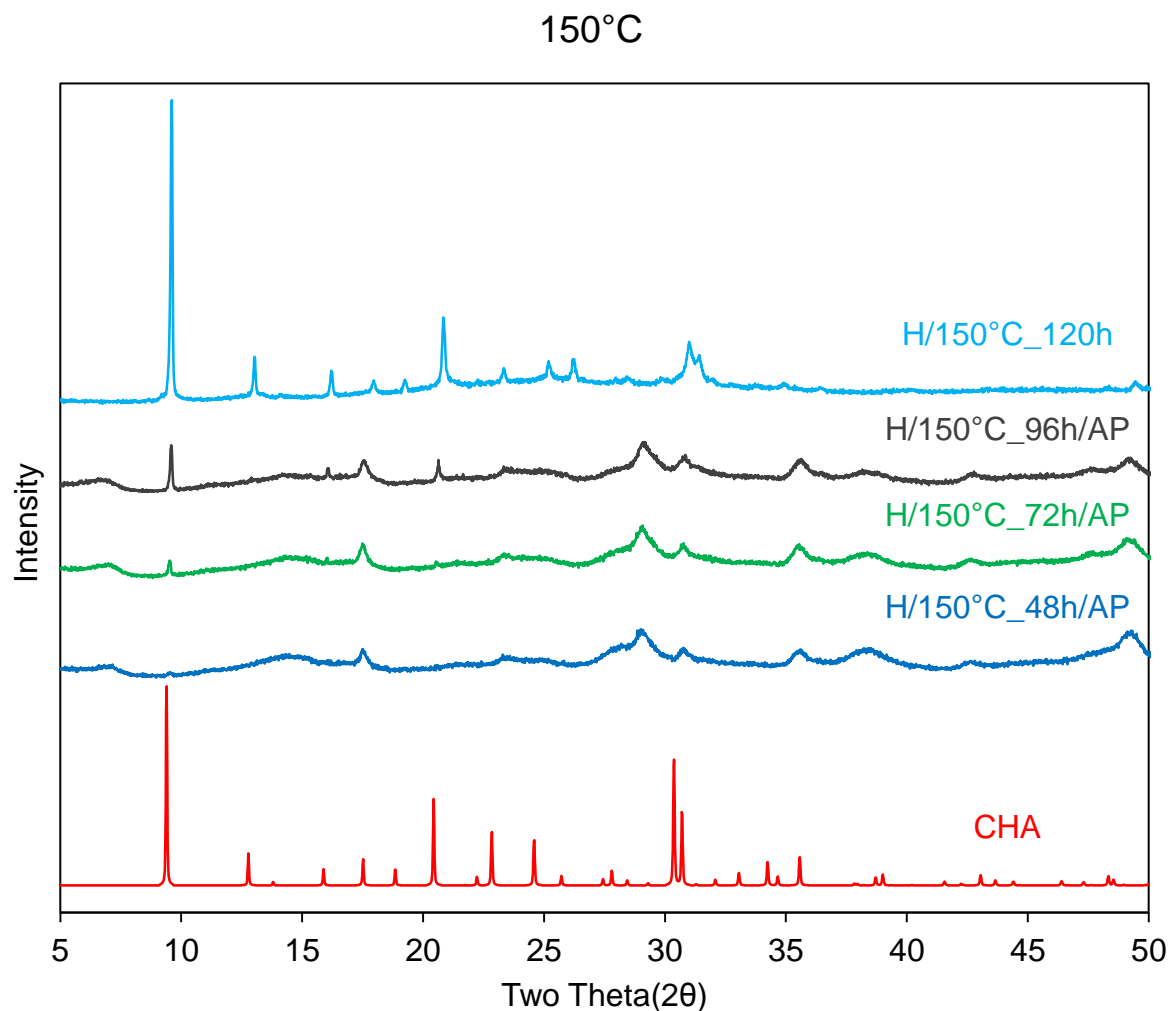


Figure 4-4: Diffractograms of AFI, CHA, and H/SAPO-34 synthesised using CTAOH as the MeSDA and crystallised at 150°C

The XRDs of the samples crystallised at 180°C are shown in Figure 4-5. The only phase pure sample was obtained with a crystallisation time of 48h, while the other crystallisation times gave a mixture of CHA- and AFI- phases. More of the AFI phase appears to form at longer crystallisation durations, with the sample left for 120h having high intensity AFI peaks.

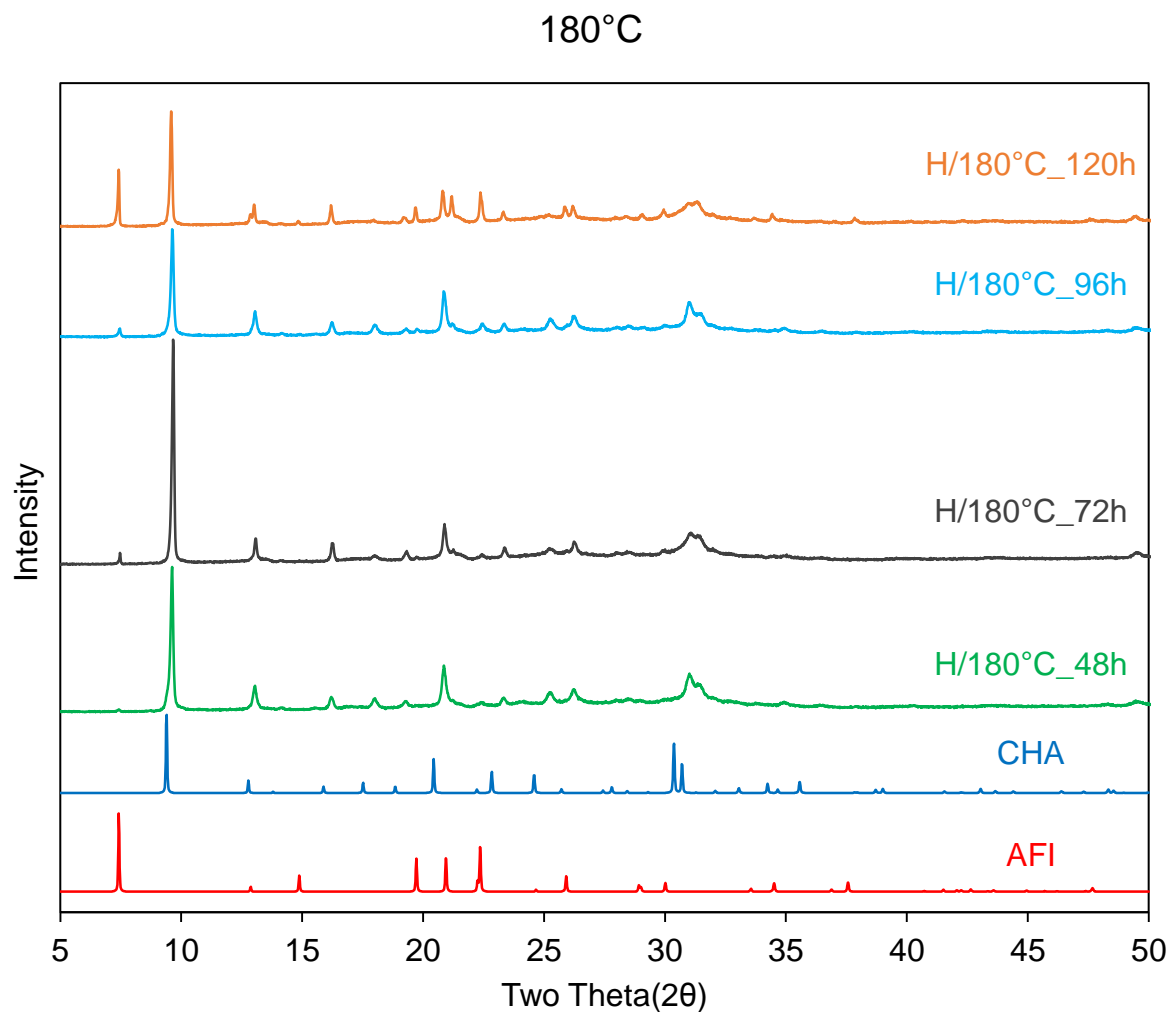


Figure 4-5: Diffractograms of AFI, CHA, and H/SAPO-34 synthesised using CTAOH as the MeSDA and crystallised at 180°C

From the XRDs of the samples crystallized at 200°C, which are shown in Figure 4-6, it appears that only the sample crystallised for 48h gave a phase pure product. The other crystallisation durations gave rise to the AFI-phase, but only small amounts. This contrasts with the effect observed for samples crystallised at 180°C, where longer crystallization times gave more of the AFI phase.

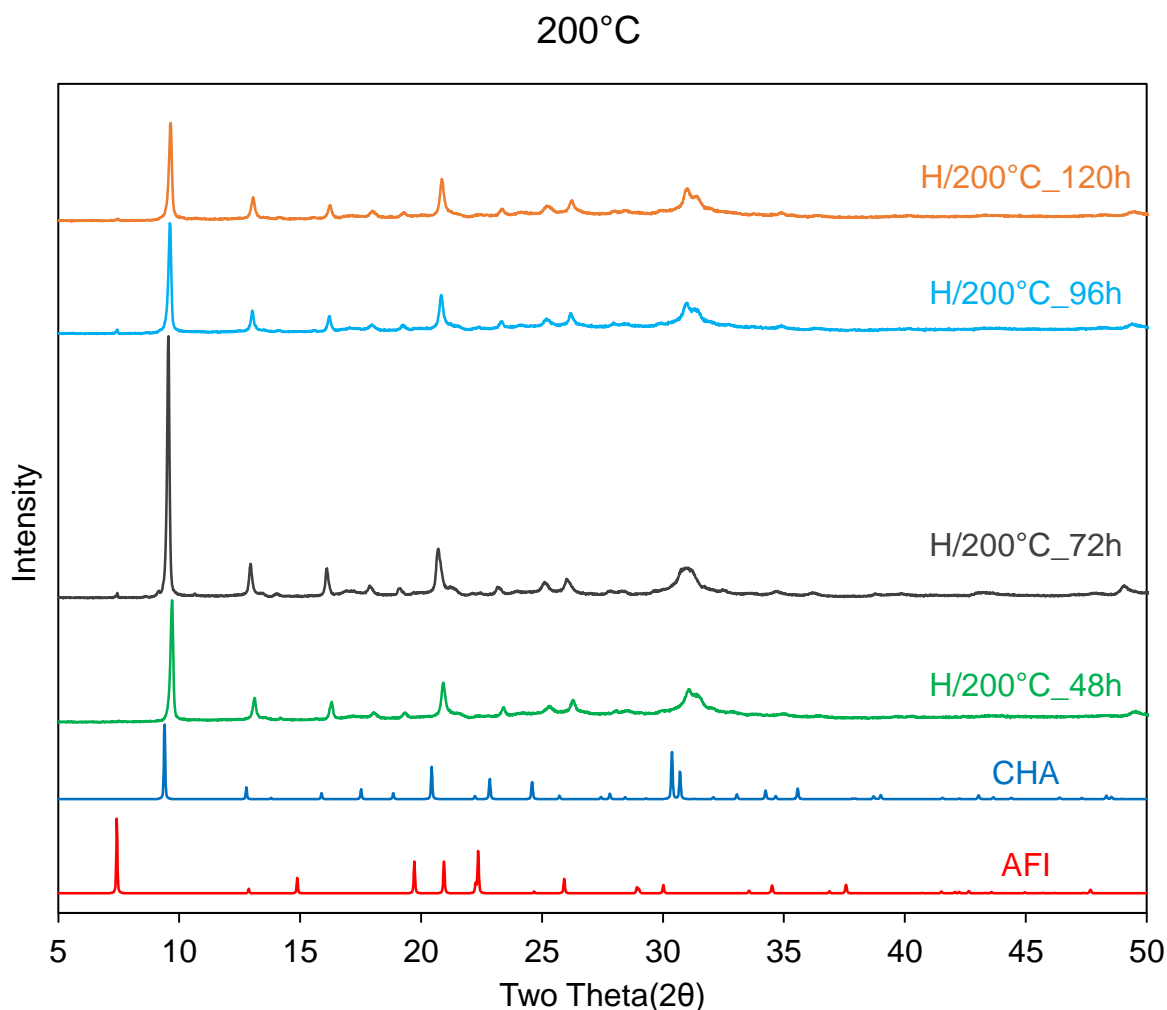


Figure 4-6: Diffractograms of AFI, CHA, and H/SAPO-34 synthesised using CTAOH as the MeSDA and crystallised at 200°C

From the parameter study, the samples H/150°C-120h, H/180°C-48h, and H/200°C-48h were found to be phase pure. These samples were therefore chosen to be characterised further.

4.1.5 H/SAPO-34: glucose(GLU) and silver behenate(Agb) as MeSDA

The two additional MeSDA tested for the syntheses of H/SAPO-34 were silver behenate(Agb) and glucose(GLU). As stated previously these samples were made with a different synthesis compared to the other H/SAPO-34 samples. The differences were that no aging was performed

and as the MiSDA morpholine and TEPA was used instead of TEA and TEOH. These samples were calcined at 150°C for 120h.

The result of these syntheses was that the sample with GLU gave a phase pure SAPO-34, while the sample with Agb gave primarily metallic silver. This is clearly visible in the XRDs show in Figure 4-7. For the H/Agb0.03 sample, the XRD is of as prepared sample, due to the sample never being calcined.

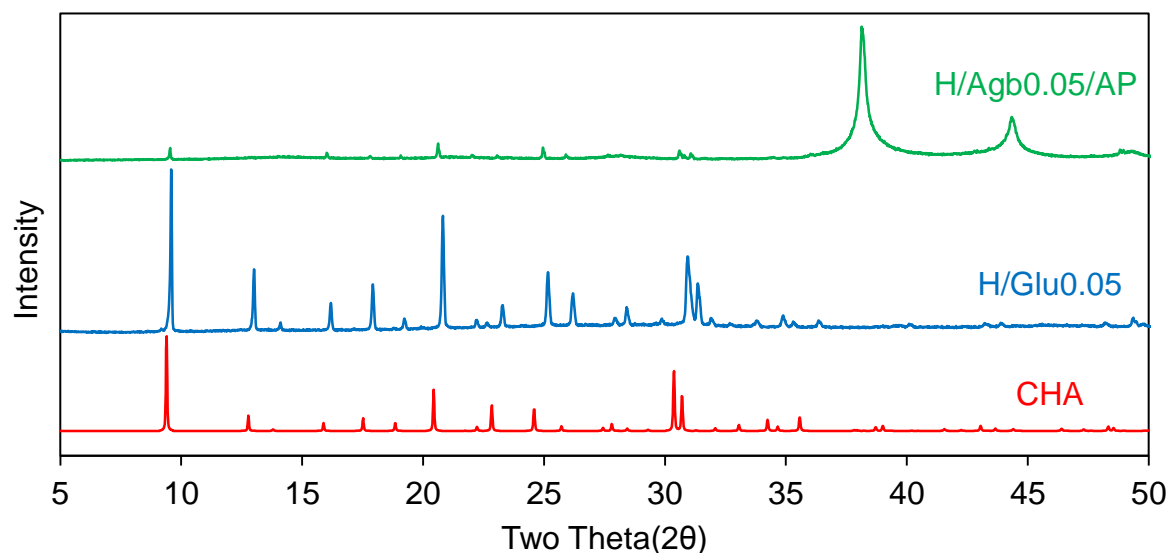


Figure 4-7: Diffractograms of CHA and H/SAPO-34 synthesised with Agb and GLU as the MeSDAs

4.1.6 H/Cu:SAPO-34

For H/CTAOH0.004, H/180°C_72h, and H/200°C_48h copper ion-exchange was performed, with diffractograms of sample post ion-exchange shown in Figure 4-8. By comparing with the diffractograms of the samples prior to ion-exchange, it can be concluded that partial collapse of the framework occurred.

The collapse of the SAPO-34 framework during ion exchange occurs due to irreversible hydrolysis, which has been shown to be more severe in SAPO-34 with high Al-O-Si bond density and framework stress³⁴.

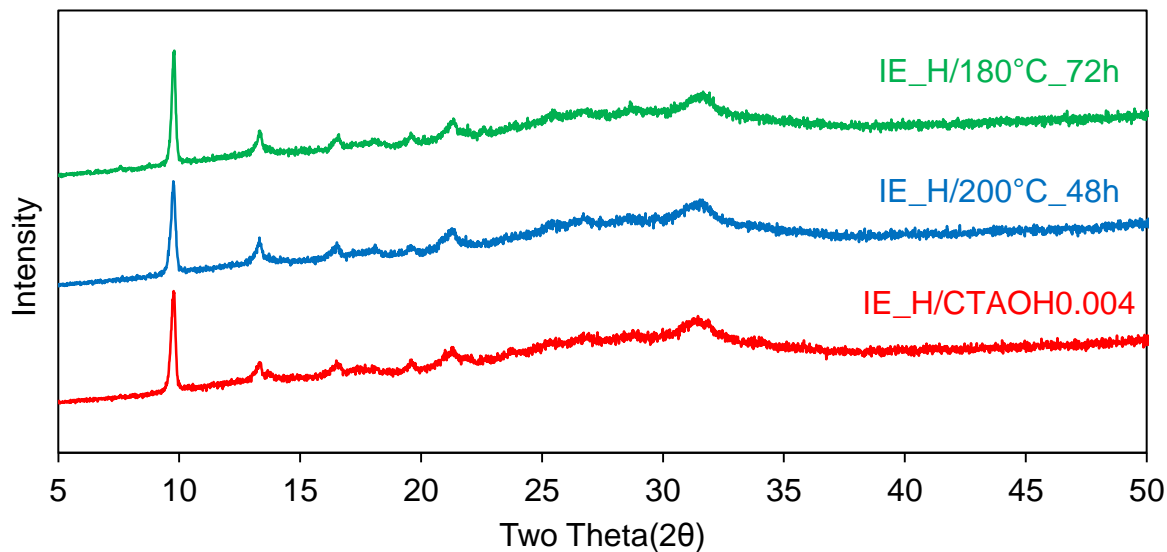


Figure 4-8: Diffractograms of the ion exchanged H/SAPO-34 samples

4.1.7 C/CuSAPO-34

In total three C/CuSAPO-34 samples were synthesised to have a basis of comparison for the H/CuSAPO-34 samples. From inspecting the diffractograms of the calcined samples shown in Figure 4-9, all samples appear to be phase pure. Of the three samples C/Si_{0.5}Cu_{0.04} is by far the more crystalline sample, with the two other samples having comparable crystallinity.

Calcined

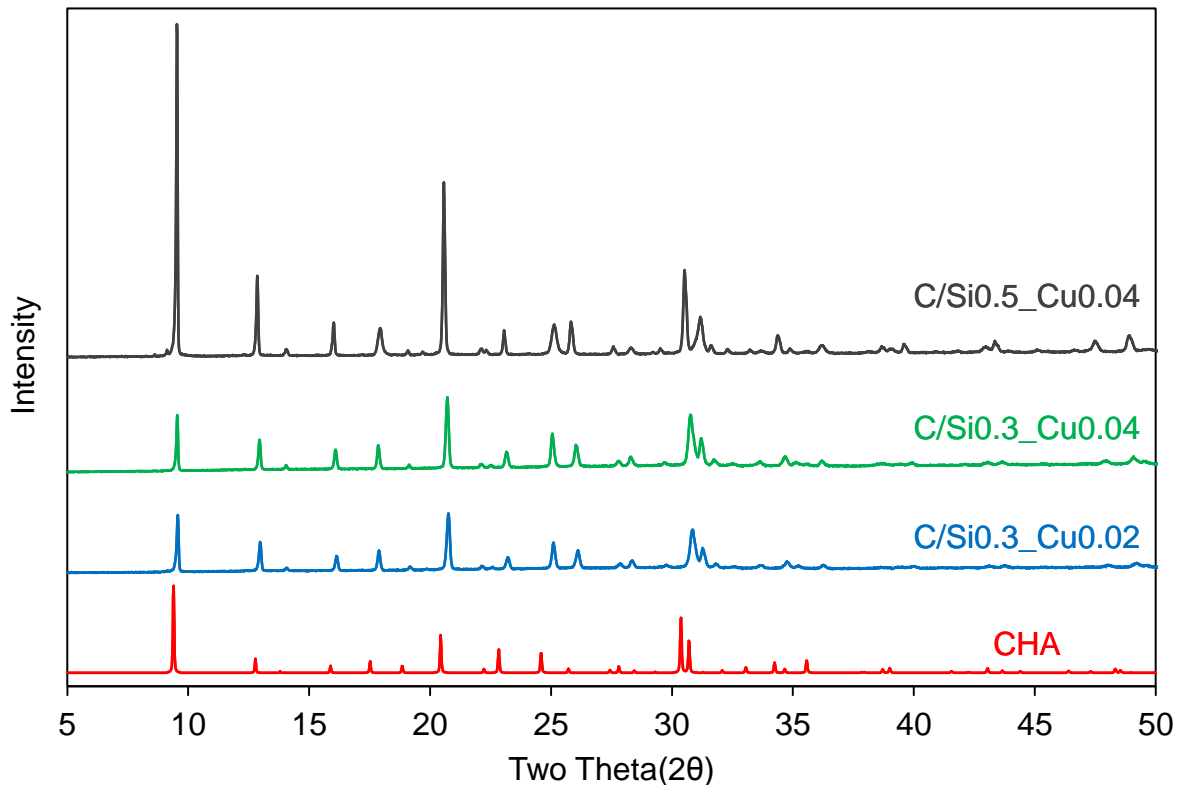


Figure 4-9: Diffractograms of the calcined C/CuSAPO-34 samples

During hydrothermal syntheses, copper has been reported to autoreduce³⁹, and detection of copper phases is therefore important. The diffractograms of metallic copper, chabazite and the as prepared samples are shown together in Figure 4-10, for this purpose. The peak that is marked with a star occurs at the same angle as a peak of metallic copper, but due to chabazite also having peaks at these angles it is difficult to ascertain the presence of metallic copper from the XRD alone.

Also shown in Figure 4-10 is the region of the diffractograms of calcines samples where CuO peaks would be found. For C/Si0.5_Cu0.04 and C/Si0.3_Cu0.04 additional peaks are marked with stars and these could arise from CuO. For C/Si0.3_Cu0.04 no additional peaks are detected, which could be due to this sample having a lower copper content. As for metallic copper, chabazite has peaks overlapping with the CuO peaks, making it difficult to draw any definitive conclusion on the presence of CuO.

Since it proved difficult to ascertain the presence of metallic copper and CuO from XRD analysis, results from XAS analysis was used to obtain a definitive answer.

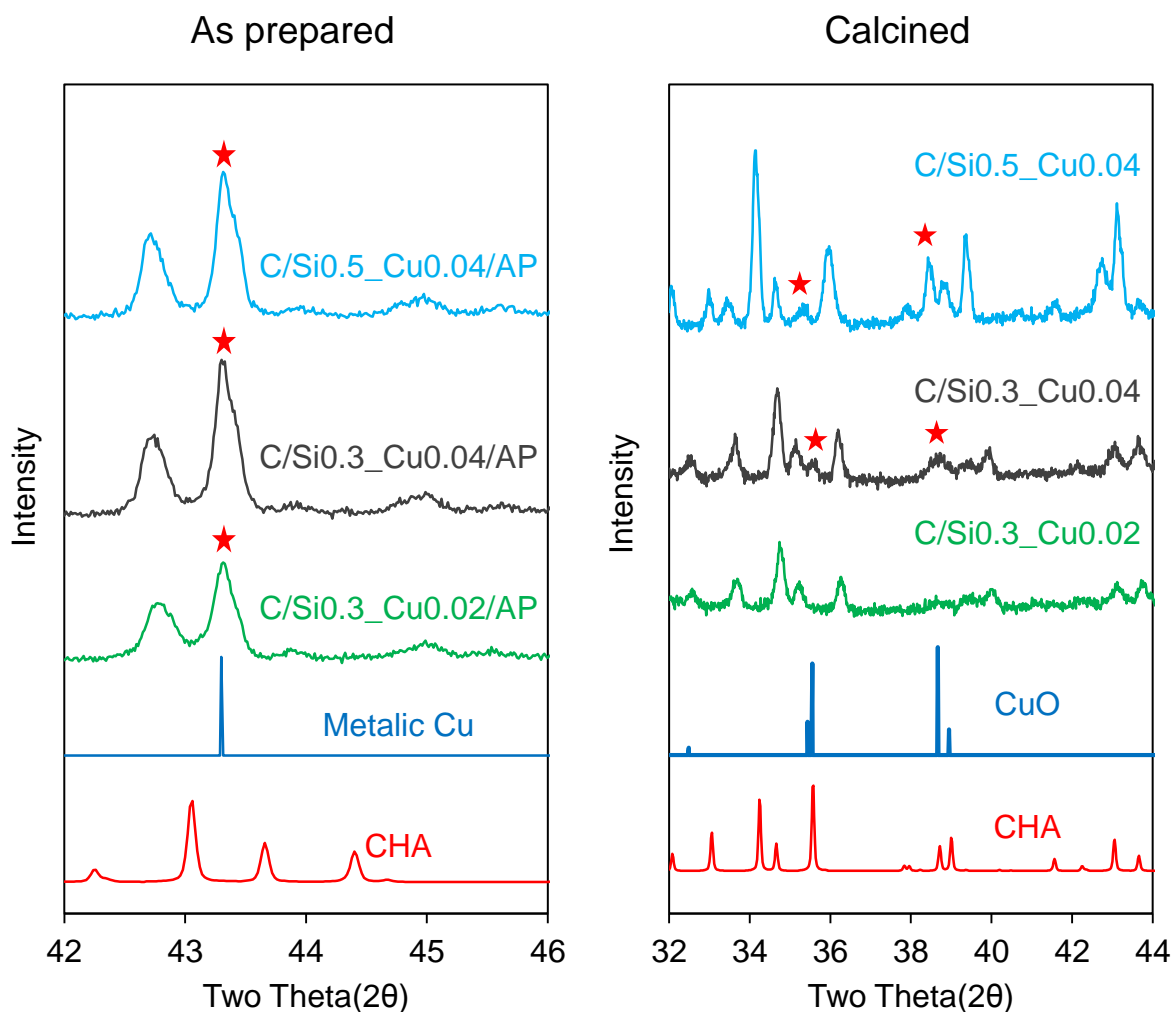


Figure 4-10: Magnified sections of the as prepared and calcined C/CuSAPO-34 diffractograms

4.1.8 H/CuSAPO-34: varying MeSDA

Several different MeSDA were tested to determine which could be used for the synthesis of H/CuSAPO-34. These samples were all made with a MeSDA/Al=0.05 and crystallised at 150°C for 120h. To determine whether the products were phase pure XRD analysis was performed, with the result summarised in Table 4-3. In total, seven different MeSDAs were tested, and of these, five of gave a product which potentially could be phase pure SAPO-34. However, there were peaks in the diffractograms of as prepared samples which could arise from metallic copper, and peaks in the diffractograms of calcined samples which could arise from CuO.

Table 4-3: Summary of the results obtained from XRD analysis for H/CuSAPO-34 samples made with various MeSDA. The XRD-results are colour-coded with red signifies an amorphous product, yellow signifying a combination CHA and a secondary phase, and green signifies potentially phase pure SAPO-34.

Sample name	MeSDA	Calcined	XRD-result
H/CTAB0.05_Cu0.02	CTAB	✓	CHA(+CuO)
H/CTAOH0.05_Cu0.02	CTAOH	✓	CHA(+CuO)
H/BA0.05_Cu0.02	Behenic acid	✓	CHA(+CuO)
H/GLU0.05_Cu0.02	Glucose	✓	CHA(+CuO)
H/TMODS0.05_Cu0.02	TMODS	✓	CHA(+CuO)
H/AgB0.05_Cu0.02/AP	Silver behenate	✗	CHA+Ag ⁰
H/DMOAC0.05_Cu0.02/AP	DMOAC	✗	Amorphous

From the diffractograms of the as prepared samples shown in Figure 4-11, it can be observed that the synthesis using DMOAC gave a completely amorphous product, and therefore no further testing was performed on this sample. Another interesting feature is seen for the sample synthesised with Agb, where the product has chabazite topology, but also contains metallic silver. This differs from the H/SAPO-34 sample made with Agb where the sample was amorphous with metallic silver. The remaining samples appeared phase pure and were therefore calcined.

As prepared

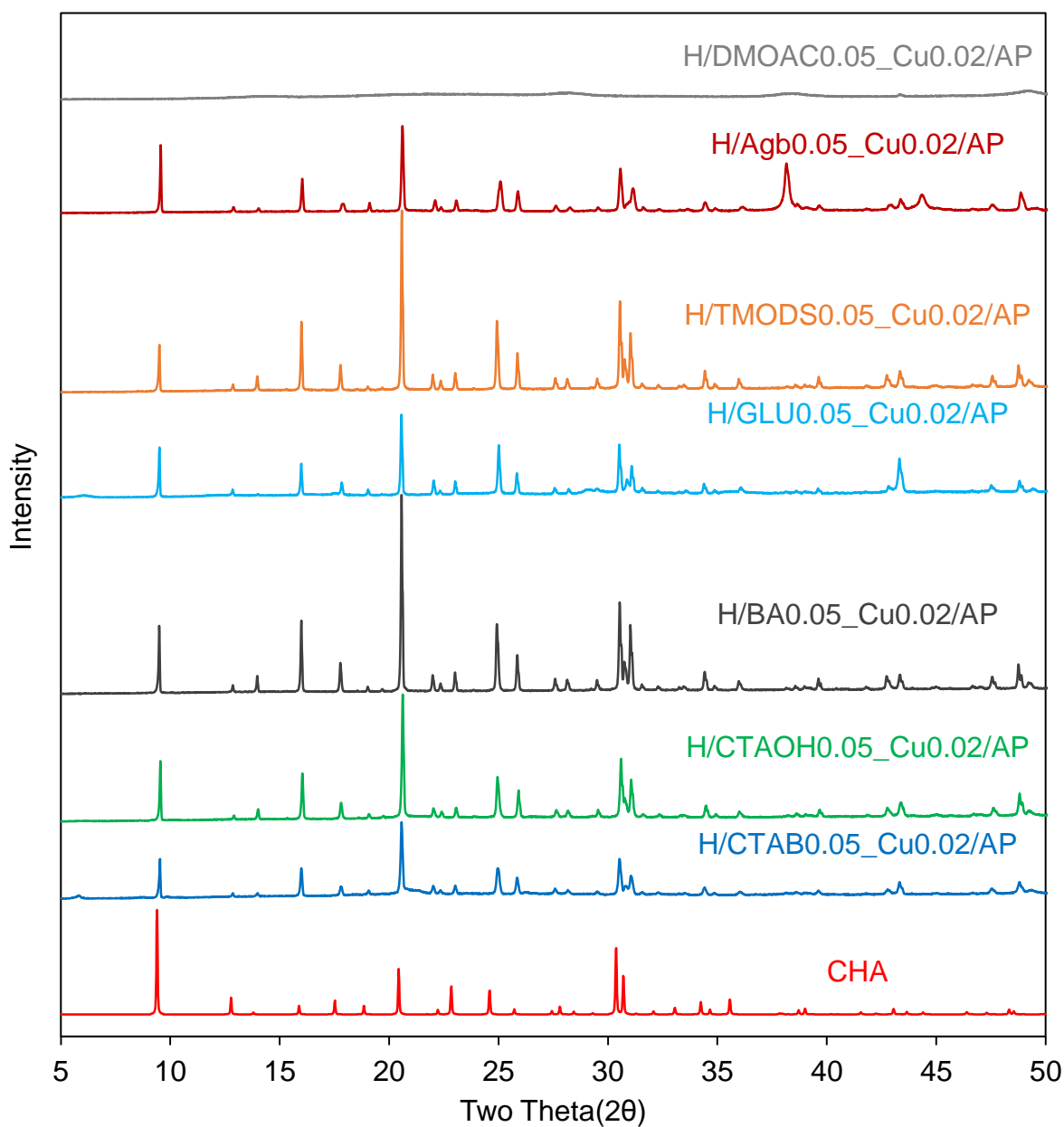


Figure 4-11: Shows the diffractograms of as prepared H/CuSAPO-34 synthesised with various MeSDAs

The diffractograms of the calcined samples are shown in Figure 4-12 and all samples appear at first inspection to be phase pure. But as for the C/CuSAPO-34 samples a more thorough investigation will be done to ascertain whether metallic copper is present in as prepared samples and if CuO is present in calcined samples.

Calcined

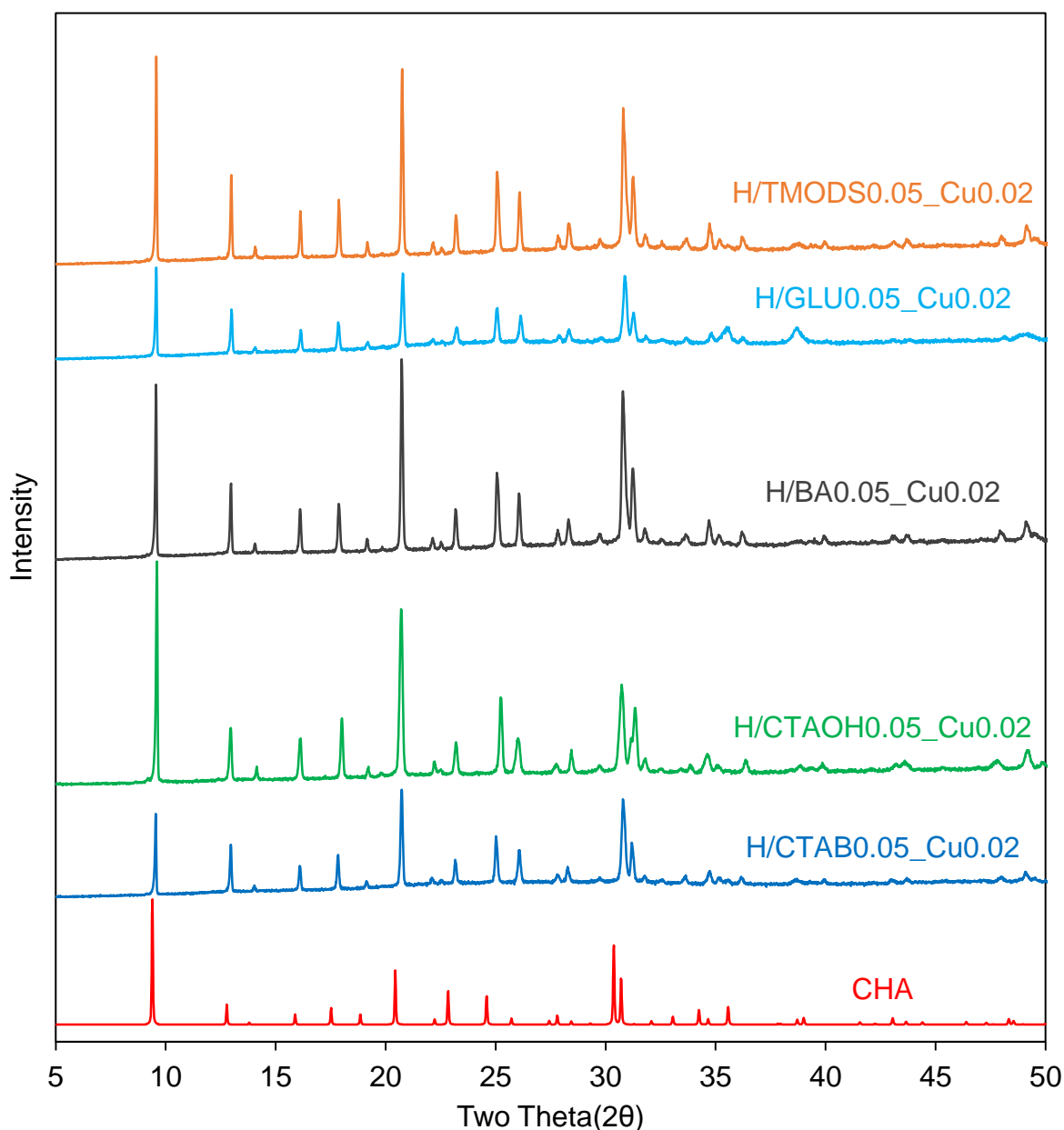


Figure 4-12: The diffractograms of calcined H/CuSAPO-34 synthesised with different MeSDAs

The regions of the diffractograms where metallic Cu and CuO peaks arise are shown in Figure 4-13 for the as prepared and calcined samples, respectively. The peaks that might arise from metallic copper and CuO are marked with stars. As was the case for the C/CuSAPO-34 it is difficult to ascertain the presence of metallic copper and CuO, due to peaks from chabazite being found at similar angles. However, the H/GLU0.05_Cu0.02 differs from the other samples in the intensity of the peaks that might arise from metallic copper and CuO. While all other

samples have similar intensities of the marked peaks, H/GLU0.05_Cu0.02 has significantly higher intensities.

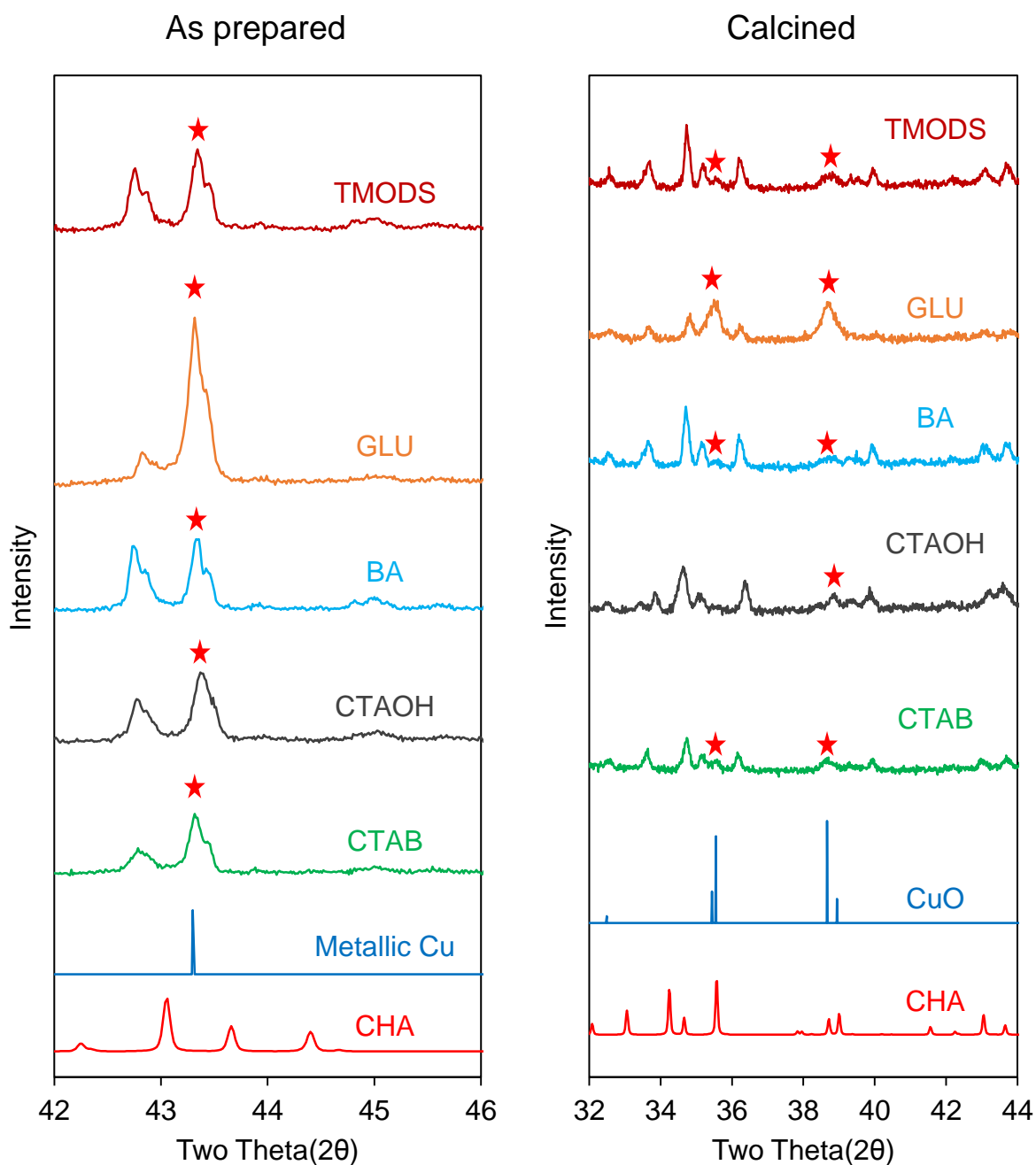


Figure 4-13: Magnified sections of the diffractograms of as prepared and calcined H/CuSAPO-34 made with different MeSDAs.

4.1.9 H/CuSAPO-34: CTAOH as MeSDA, with Varying Cu and Si content

CTAOH was used as the MeSDA in a study of the effect of varying Cu and Si content. The CTAOH mole fraction was held constant at 0.01 and the samples were crystallised at 150°C for 120h. A set of samples were made with Si/Al=0.3 and another set was made with Si/Al=0.5,

and for both sets Cu/Al was varied between 0.02 and 0.06. The result of the XRD analysis will only be presented for samples made with Si/Al=0.5, since the same trends were seen for both Si mole fractions. The diffractograms of as prepared and calcined samples with Si/Al=0.3 can be found in appendix B.

Based on the diffractograms shown in Figure 4-14, the samples set made with Si/Al=0.5 appears to be phase pure for all copper contents. The variation of copper content appears to have little effect on the crystallinity of the samples, with all samples having similar intensities. These observations were also made for samples with Si/Al=0.3

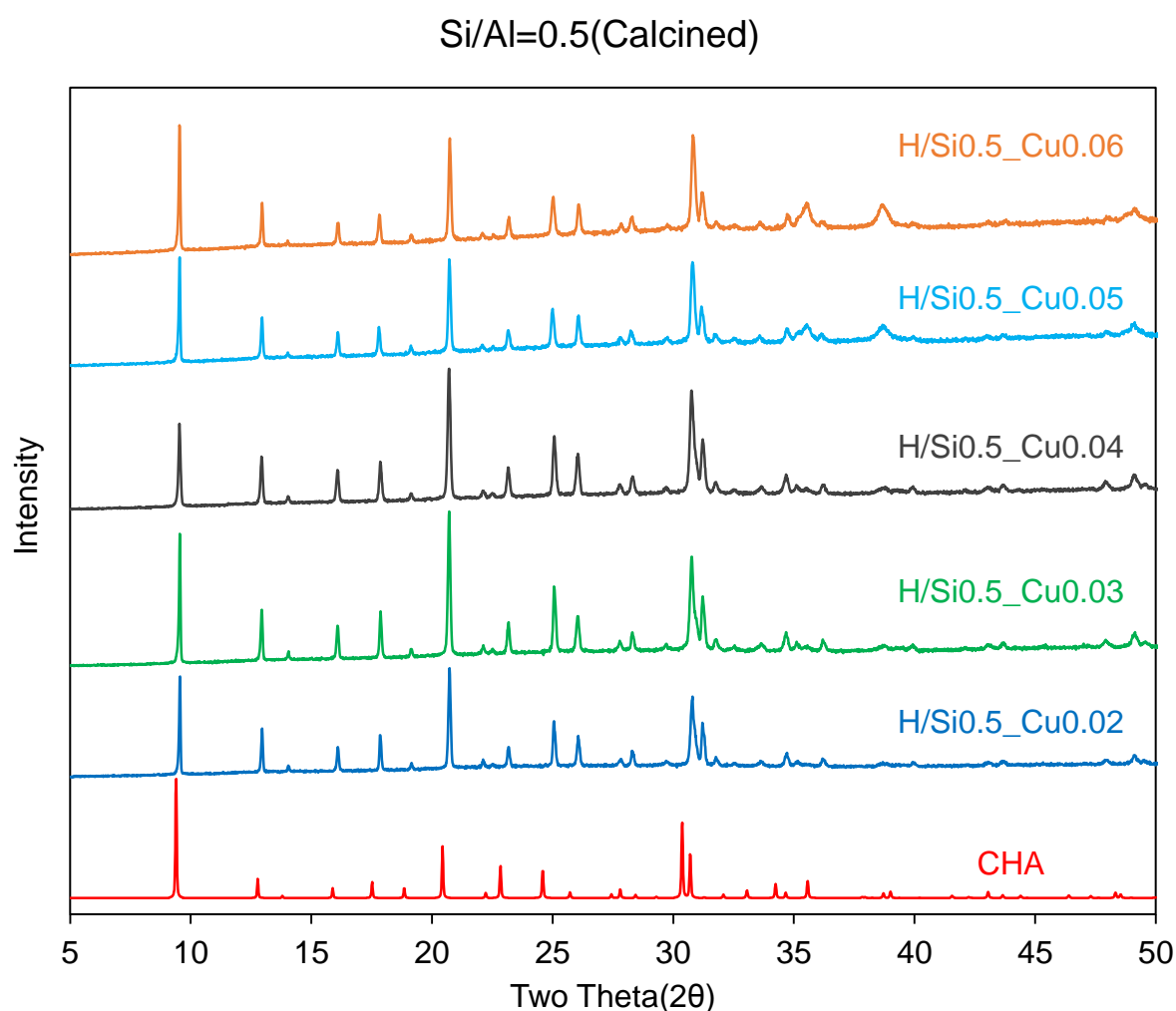


Figure 4-14: The diffractograms of calcined H/CuSAPO-34 made with CTAOH, Si/Al=0.5 and varying copper content

As in previous sections, the regions of the diffractograms where metallic copper and CuO peaks occur is shown in Figure 4-15. In the as prepared samples the peak that could arise due to metallic copper increases in intensity with increasing copper content. The same trend is also seen for the potential CuO peaks in calcined samples.

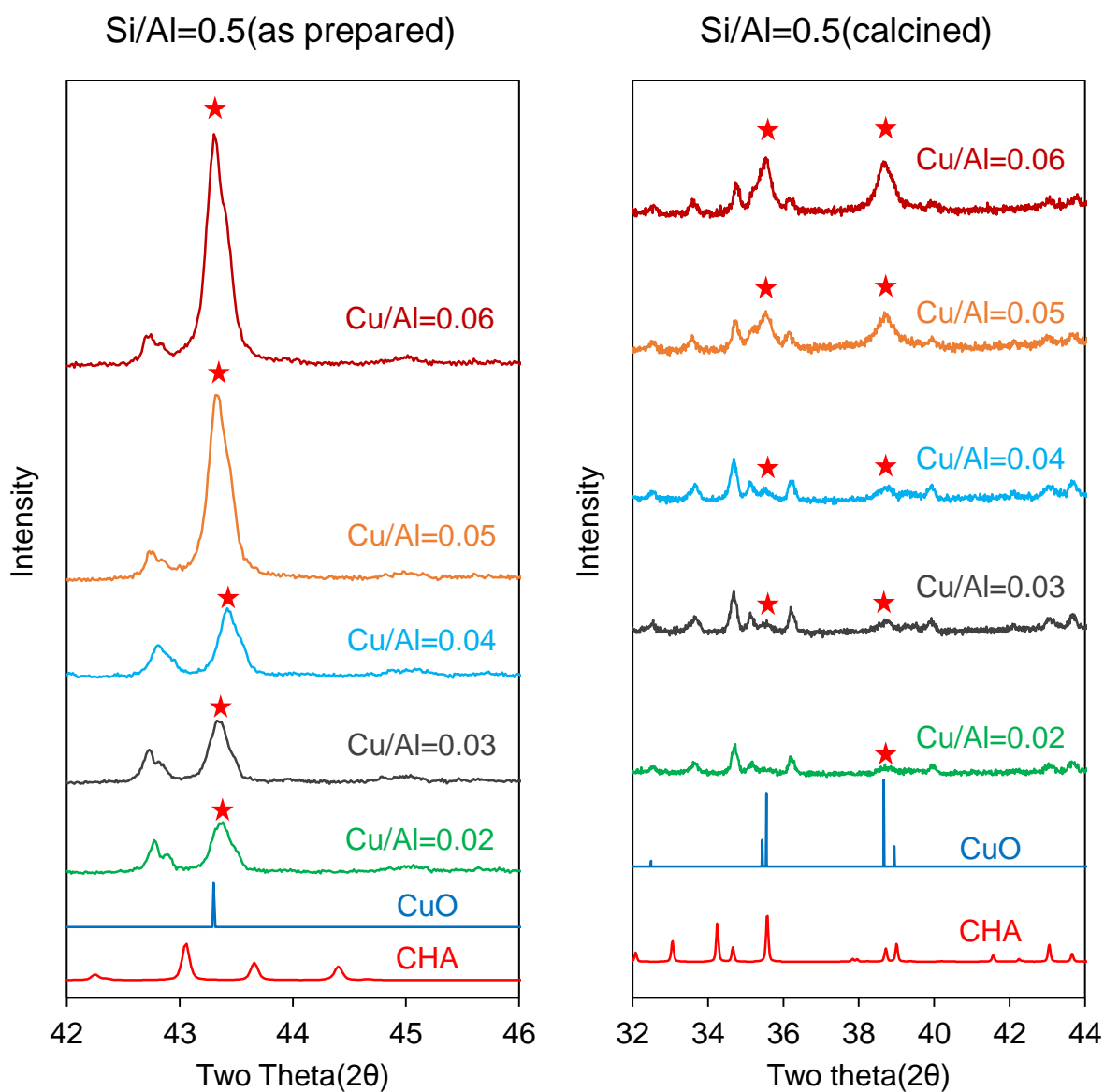


Figure 4-15: Magnified sections of the diffractograms of as prepared and calcined H/CuSAPO-34 made with CTAOH and Si/Al=0.5, with varying copper content.

4.2 N₂-physisorption

4.2.1 C/SAPO-34 and H/SAPO-34

N₂-physisorption was conducted for the phase pure H/SAPO-34 samples and for the C/SAPO-34 sample, C/Si_{0.26}, and whether the samples were classified as hierarchical is stated in Table 4-4. The classification was done by comparing mesopore surface areas and volumes as well as evaluation of the N₂ adsorption-desorption isotherm and BJH plots.

Table 4-4: Shows whether C/Si0.26 and H/SAPO-34 samples were classified as being hierarchical based on result of N₂-physisorption results. Also shown is the MeSDA and the MeSDA/Al used, as well as crystallisation parameters.

Sample name	MeSDA	MeSDA/Al	Crystallisation	Hierarchical
C/Si0.26	-	-	72h at 180°C	✗
H/CTAB0.01	CTAB	0.01	72h at 180°C	✗
H/150°C_120h	CTAOH	0.005	120h at 150°C	✓
H/180°C_48h	CTAOH	0.005	48h at 180°C	✗
H/200°C_48h	CTAOH	0.005	48h at 200°C	✗
H/GLU0.05	GLU	0.05	120h at 150°C	✓

From the surface areas plotted in Figure 4-16 it is observed that H/CTAB0.01, H/180°C_48h, H/180°C_48h, and C/Si0.26 has a total surface area above 550m²/g, which is the benchmark value for SAPO-34. The total surface area of H/GLU0.05 and H/150°C_120h on the other hand is below 550m²/g, with the specific values being 298m²/g and 470m²/g, respectively. H/GLU0.05 and H/150°C_120h also had a significantly larger mesopore surface areas compared to C/Si0.26, with the specific values being 97m²/g for H/GLU0.05 and 83m²/g for H/150°C_120h. Mesopore surface areas of similar magnitude has also been reported previously for H/SAPO-34¹, which indicates that H/GLU0.05 and H/150°C_120h are hierarchical. For H/CTAB0.01, H/180°C_48h and H/180°C_48h the mesopore volume is only slightly larger compared to C/Si0.26, which indicates that these samples are not very hierarchical.

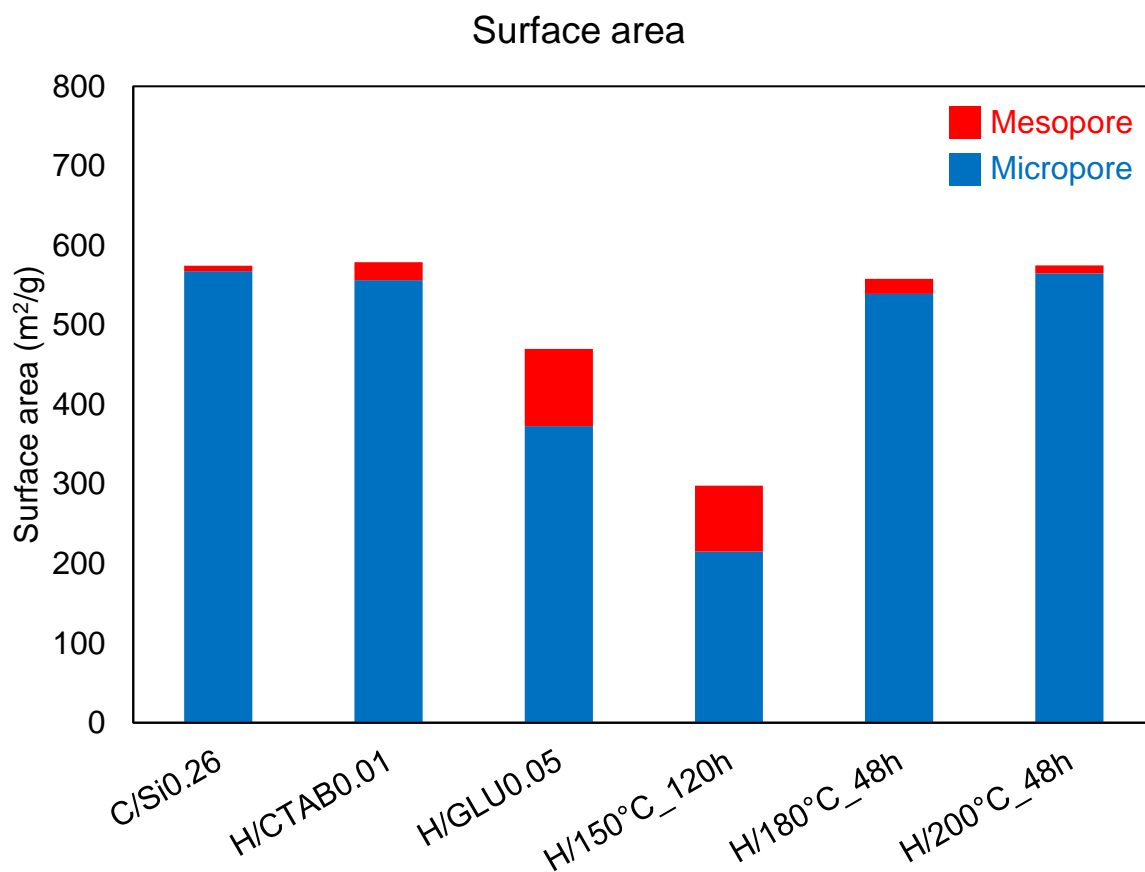


Figure 4-16: Surface areas of H/SAPO-34 samples and C/Si0.26, with red signifying mesopore surface area and blue signifying micropore surface area

Similar trends as the ones observed for surface areas, can be observed for the pore volumes plotted in Figure 4-17. The mesopore volume of H/GLU0.05 and H/150°C_120h is significantly larger compared to C/Si0.26, with values of 0.195cm³/g and 0.214cm³/g, respectively. These values of mesopore volumes are larger compared to what has been reported for H/SAPO-34 previously^{1, 53, 67}, and therefore lends credence to the classification of H/GLU0.05 and H/150°C_120h as hierarchical SAPO-34. For H/CTAB0.01, H/180°C_48h and H/180°C_48h the mesopore volume is observed being only slightly larger compared to C/Si0.26, and these samples were classified as C/CuSAPO-34.

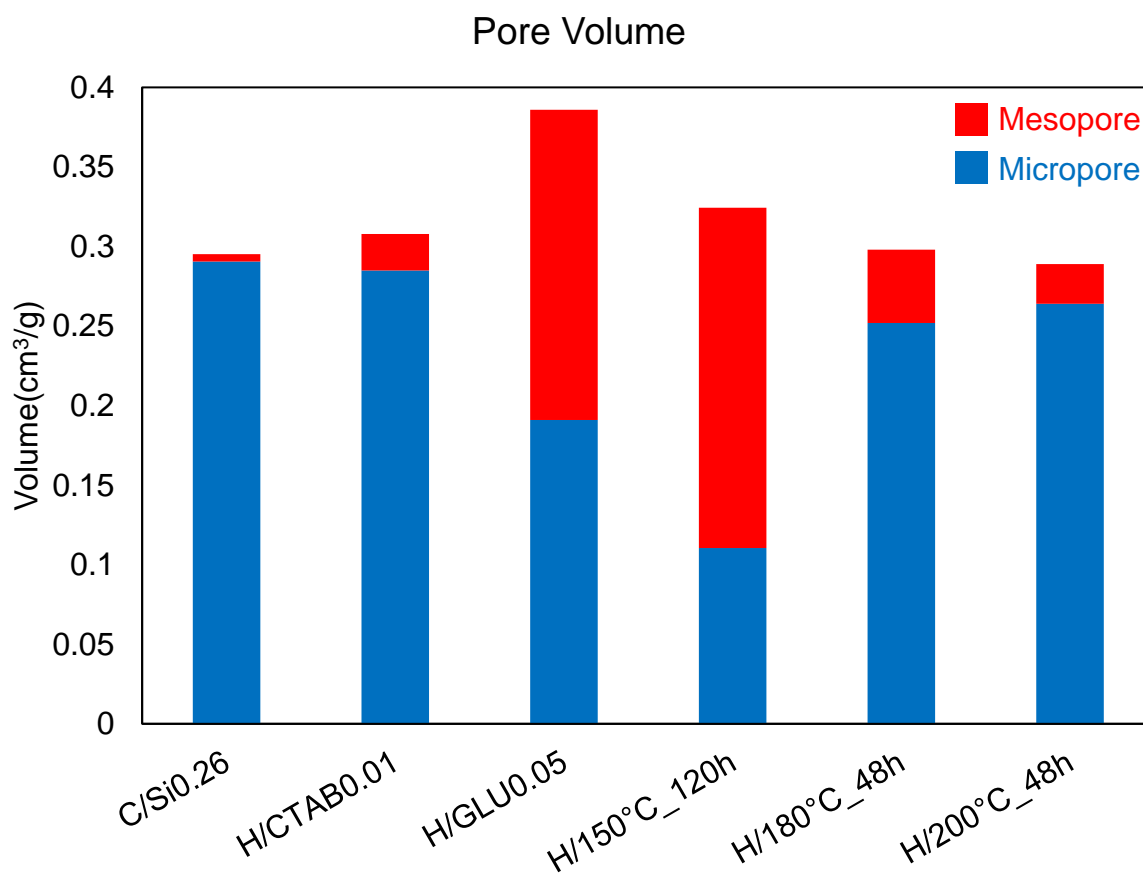


Figure 4-17: Pore volumes of H/SAPO-34 samples and C/Si0.26, with red signifying mesopore volume and blue signifying micropore volume

The isotherm and BJH plots for H/150°C_120h and H/GLU0.05, shown in Figure 4-18, also indicate the presence of mesopores. For both H/150°C_120h and H/GLU0.05, a hysteresis can be observed, although with differing shapes. For H/150°C_120h the hysteresis appears to be a combination of a type 3 and a type 4 hysteresis. This is indicating that the mesopores are disordered with no clearly defined size. For H/GLU0.05 the hysteresis also appears to be a combination of a type 3 and type 4 hysteresis, but a plateau is also observed in the hysteresis.

This could be due to the presence of more highly ordered pores with a narrower pore size, giving rise to a type 1 or type 2 hysteresis.

The BJH plots appear to back up the fact that H/GLU0.05 contains some more ordered mesopores. The defined peak that occurs at 50Å, indicate the presence of mesopores with a pore size of 50Å. For H/150°C_120h the BJH is a sloping curve, which lends credence to the mesopores being disordered with no defined pore size.

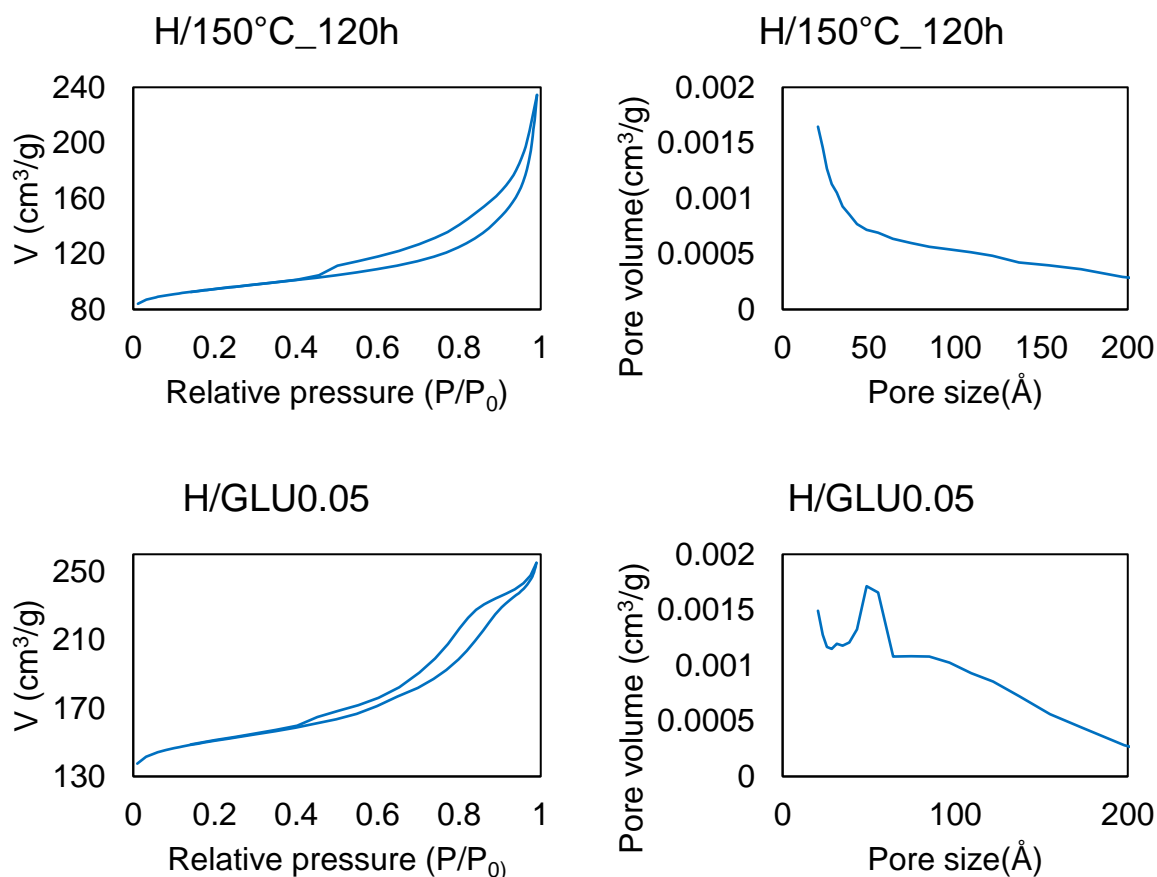


Figure 4-18: N_2 adsorption-desorption isotherm(left) and BJH plot(right) for H/150°C_120h(top) and H/GLU0.05(bottom)

In summary the H/GLU0.05 and H/150°C_120h were the only two samples that were classified as being hierarchical.

4.2.2 C/CuSAPO-34 and H/CuSAPO-34

4.2.2.1 H/CuSAPO-34: varying MeSDA

Based on XRD-results, N_2 -physisorption was performed for five of the seven H/CuSAPO-34 samples made with different MeSDA, to determine if the samples were hierarchical. In addition, N_2 -physisorption was also performed for the analogue C/CuSAPO-34 sample, C/Si0.3_Cu0.02, to have a basis of comparison. Whether the samples were classified as being hierarchical is

stated Table 4-5, with the conclusion drawn based on mesopore surface areas and volumes, N₂ adsorption-desorption isotherm, and BJH plots.

Table 4-5: Shows whether C/Si0.3_Cu0.02 and H/CuSAPO-34 samples synthesised with various MeSDA were classified as being hierarchical based on result of N₂-physisorption results

Sample name	MeSDA	Hierarchical
C/Si0.3_Cu0.02	-	✗
H/CTAB0.05_Cu0.02	CTAB	✓
H/CTAOH0.05_Cu0.02	CTAOH	✓
H/BA0.05_Cu0.02	BA	✗
H/GLU0.05_Cu0.02	GLU	✓
H/TMODS0.05_Cu0.02	TMODS	✗

From the surface areas plotted in Figure 4-19, the mesopore surface areas for H/CTAB0.05_Cu0.02, H/CTAOH_Cu0.02 and H/GLU0.05_Cu0.02 is observed being significantly higher compared to C/Si0.3_Cu0.02, which indicates that these materials are hierarchical. However, for H/GLU0.05_Cu0.02 the total surface area is only 187m²/g, which is much lower compared to the other samples. For H/BA0.05_Cu0.02 and H/TMODS0.05_Cu0.02 the mesopore surface area is comparable to C/Si0.3_Cu0.02, and these samples are most likely not hierarchical.

Surface area

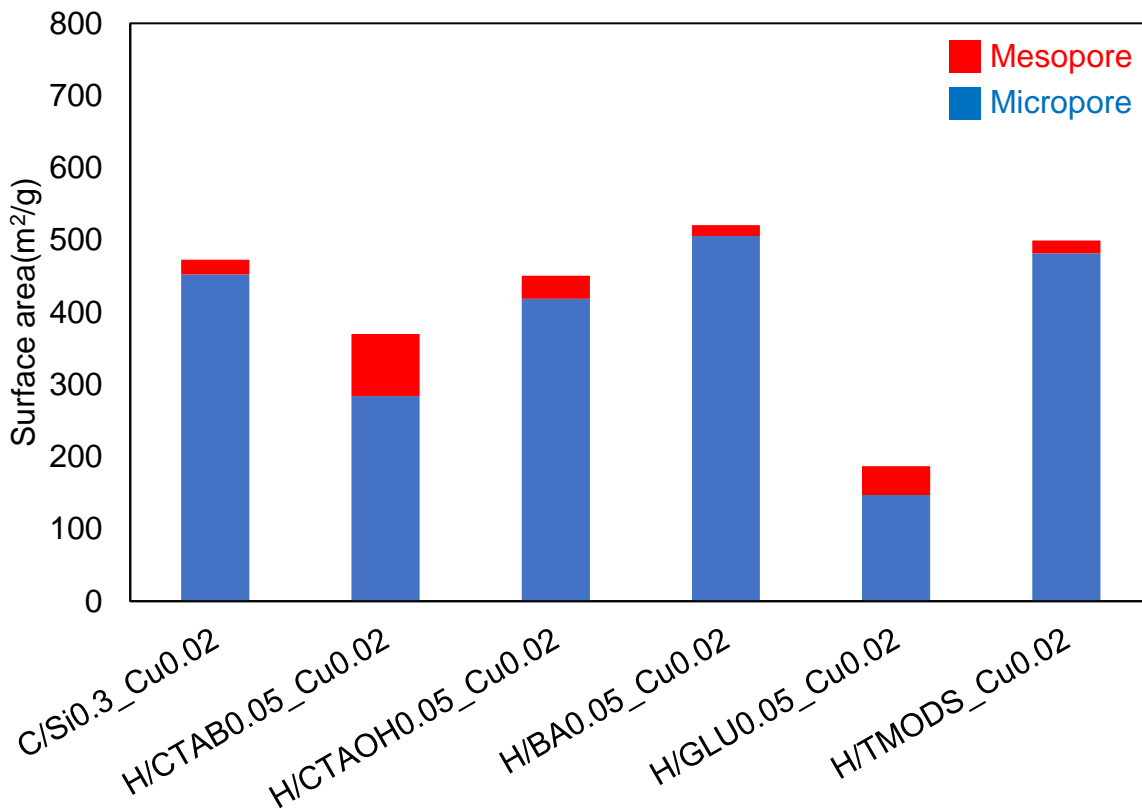


Figure 4-19: Surface areas for C/Si0.3_Cu0.02 and H/CuSAPO-34 samples made with various MeSDAs, with red signifying mesopore contributions and blue signifying micropore contributions

Similar trends as for surface areas, can be seen from the pore volumes plotted in Figure 4-20. The mesopore volume of H/CTAB0.05_Cu0.02, H/CTAOH_Cu0.02 and H/GLU0.05_Cu0.02 is much larger compared to C/Si0.3_Cu0.02, and these samples are therefore classified as hierarchical. However, due to the low total surface area of H/GLU0.05_Cu0.02, no further results will be presented for this samples. The mesopore volume of H/BA0.05_Cu0.02 and H/TMODS0.05_Cu0.02 shows comparable mesopore volumes to C/Si0.3_Cu0.02 and these samples were therefore classified as being C/CuSAPO-34.

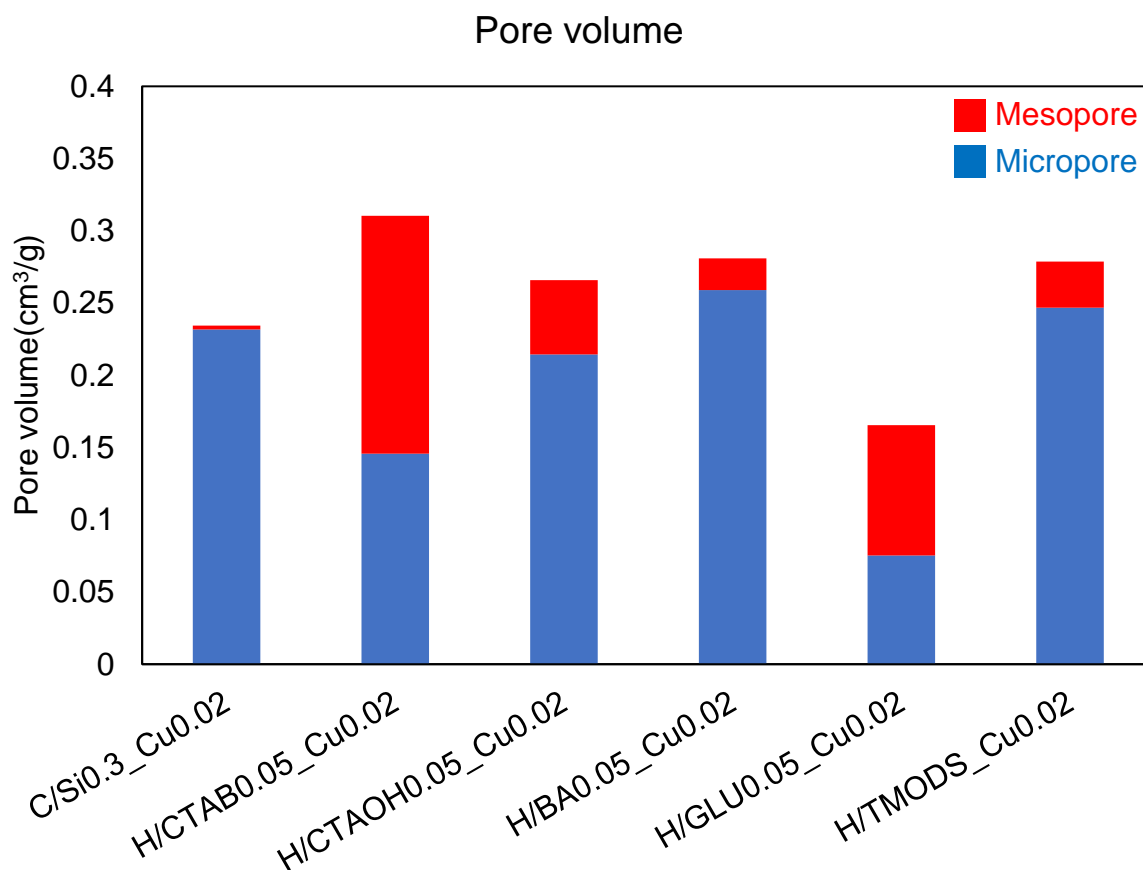


Figure 4-20: Pore volumes for C/Si_{0.3}-Cu_{0.02} and H/CuSAPO-34 samples made with various MeSDAs, with red signifying mesopore contributions and blue signifying micropore contributions

The N₂ adsorption-desorption isotherm and BJH plots for H/CTAB_{0.05}-Cu_{0.02} and H/CTAOH_{0.05}-Cu_{0.02}, shown in Figure 4-21, also indicate a hierarchical pore system. Both samples show a hysteresis which appears to be a combination of a type 3 and a type 4 hysteresis. This indicates disordered mesopores with no clearly defined pore size. However, the samples differ in the shape of the BJH plots. The BJH-plot of the sample made with CTAB has a peak slightly below 50 Å, while the sample made with CTAOH is a smooth line without any clear peaks. This could mean that the sample made with CTAB has a more defined pore size compared to the CTAOH sample. The peak is however very slight and only consist of a single data point.

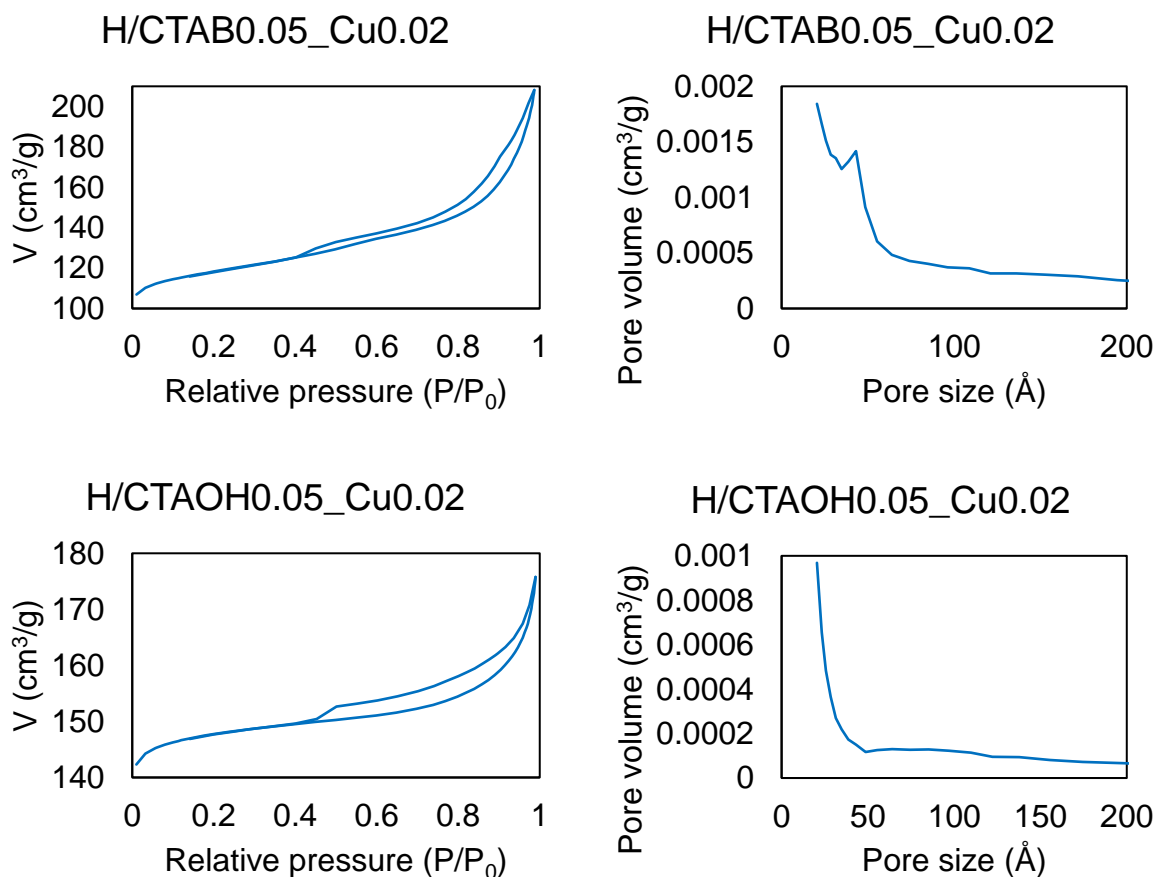


Figure 4-21: N₂ adsorption-desorption isotherm(left) and BJH plot(right) for H/CTAB0.05_Cu0.02 (top) and H/CTAOH0.05_Cu0.02 (bottom)

From N₂-physisorption, CTAOH and CTAB appear to be the most promising MeSDA for synthesis of H/CuSAPO-34. The reason CTAOH was used for the syntheses where Cu and Si content was varied, was due to fear of bromide complexing copper and thereby hindering incorporation of copper.

4.2.3 H/CuSAPO-34: CTAOH as MeSDA with Varying Cu and Si content

N₂-physisorption was performed for a selection of the samples made with CTAOH and varying amounts of Cu and Si content. In addition, N₂-physisorption was also performed for C/Si0.3_Cu0.04 and C/Si0.5_Cu0.04 to have a basis of comparison. As can be seen in Table 4-6, all H/CuSAPO-34 tested were characterised as being hierarchical. However, as will be shown below, large variations in surface areas and pores volumes are present between the samples.

Table 4-6: Shows whether C/Si0.3_Cu0.04, C/Si0.5_Cu0.04 and selection of H/CuSAPO-34 samples made with CTAOH were classified as being hierarchical based on result of N₂-physisorption results. Also shown is the Si and copper contents added during syntheses.

Sample name	Si/Al	Cu/Al	Hierarchical
C/Si0.3_Cu0.04	0.3	0.04	✗
C/Si0.5_Cu0.04	0.5	0.04	✗
H/Si0.3_Cu0.02	0.3	0.02	✓
H/Si0.3_Cu0.04	0.3	0.04	✓
H/Si0.5_Cu0.02	0.5	0.02	✓
H/Si0.5_Cu0.04	0.5	0.04	✓
H/Si0.5_Cu0.06	0.5	0.06	✓

From the plotted surface areas shown in Figure 4-22, the total surface area is observed ranging between 281-402m²/g for the H/CuSAPO-34 samples. This is lower compared to the C/CuSAPO-34 samples which had total surface areas in the range 452-487m²/g. The mesopore surface areas of the H/CuSAPO-34 samples are larger compared to the C/CuSAPO-34, indicating that the samples are hierarchical. However, changes in both total surface area and mesopore volume is observed with changes in Si and Cu content, but no clear trend is apparent.

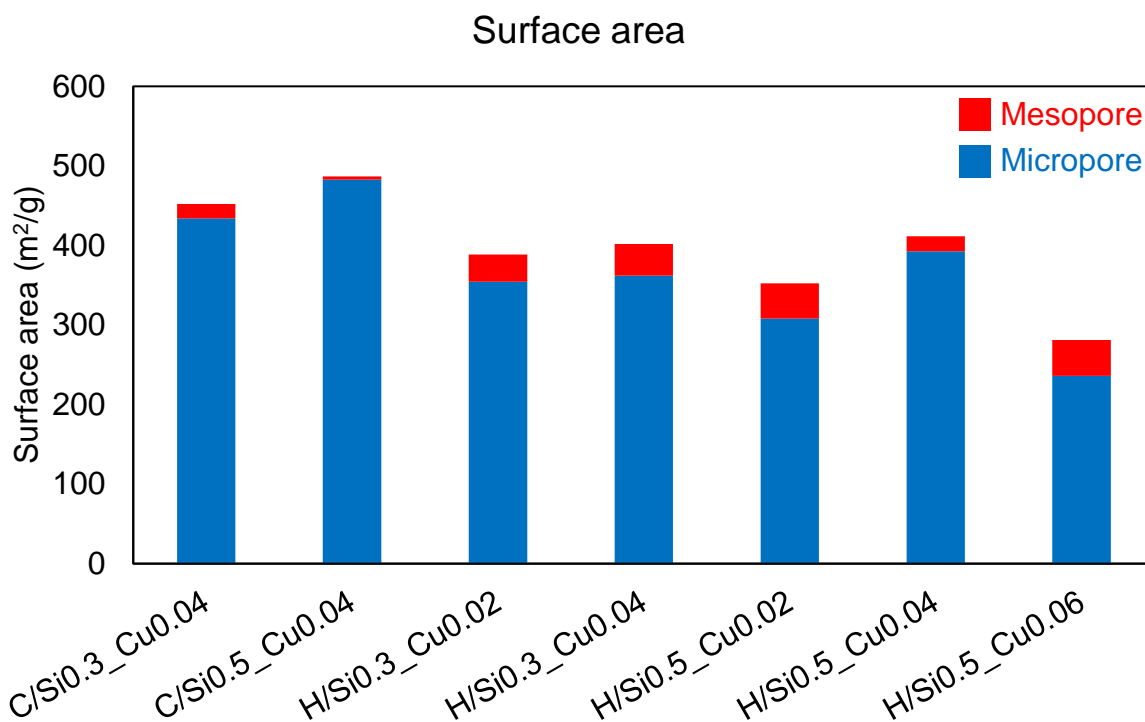


Figure 4-22: Surface areas for C/Si_{0.3}Cu_{0.04}, C/Si_{0.5}Cu_{0.04}, and H/CuSAPO-34 samples made with CTAOH, with red signifying mesopore contributions and blue signifying micropore contributions

The pore volumes plotted Figure 4-23 show much the same trends as the surface areas. For all H/CuSAPO-34 the mesopore volume is larger than for the C/CuSAPO-34, and all samples are therefore characterised as being hierarchical. However, the mesopore volumes are observed varying with Cu and Si content, but no clear trend is apparent.

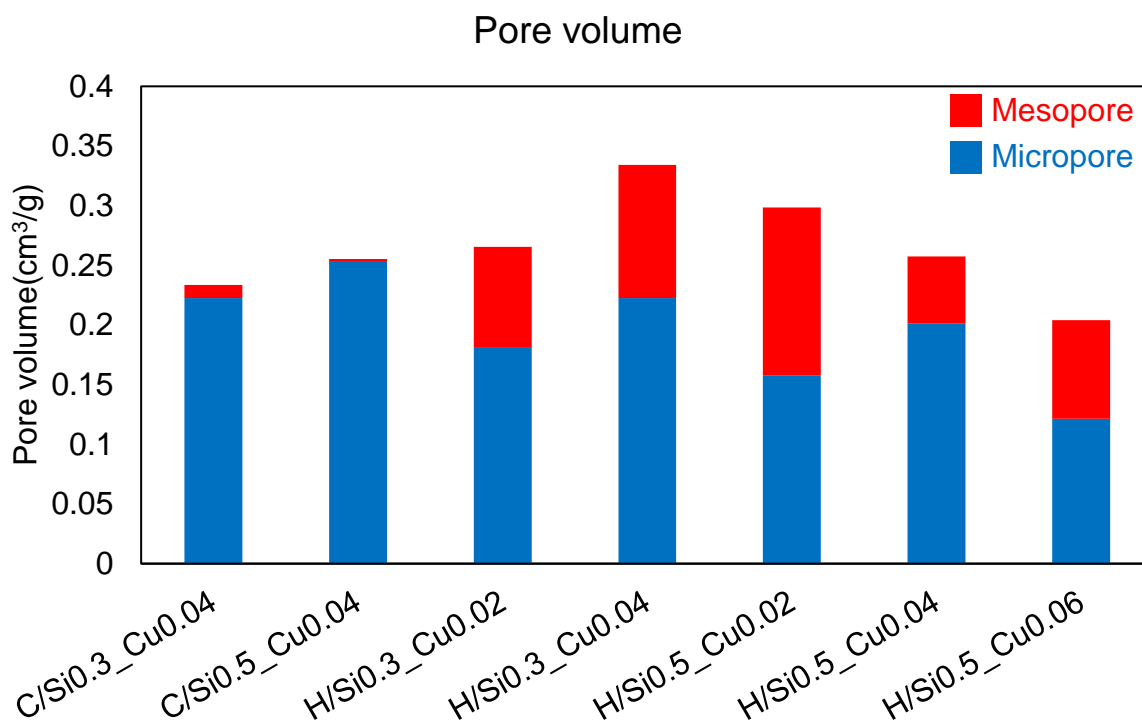


Figure 4-23: Pore volumes for C/Si0.3_Cu0.04, C/Si0.5_Cu0.04, and H/CuSAPO-34 samples made with CTAOH, with red signifying mesopore contributions and blue signifying micropore contributions

The N₂ adsorption-desorption isotherms and BJH plots for the samples are shown in Figure 4-24 and Figure 4-25. All samples have the combination of a type 1 and a type 4 adsorption isotherm that is expected for hierarchical materials. There are only minor differences in the shape of the hysteresis, with all samples having a hysteresis that appears to be a combination of a type 3 and type 4 hysteresis. However, for both samples with H/Si0.3_Cu0.04 and for H/Si0.5_Cu0.02 there is a plateau which occurs in the desorption part of the hysteresis.

Differences are also seen in the BJH plots. H/Si0.5_Cu0.02 has a broad peak in the range 50-200 Å. Both H/Si0.3_Cu0.02 and H/Si0.3_Cu0.04 has a similar broad peak, but also has a peak occurring slightly below 50 Å, which could signify the presence of some more ordered mesopores. For the H/Si0.5_Cu0.04 and H/Si0.5_Cu0.06 the BJH plot is mostly flat with no clearly defined peaks, which is indicative of disordered pores without a clearly defined pore size.

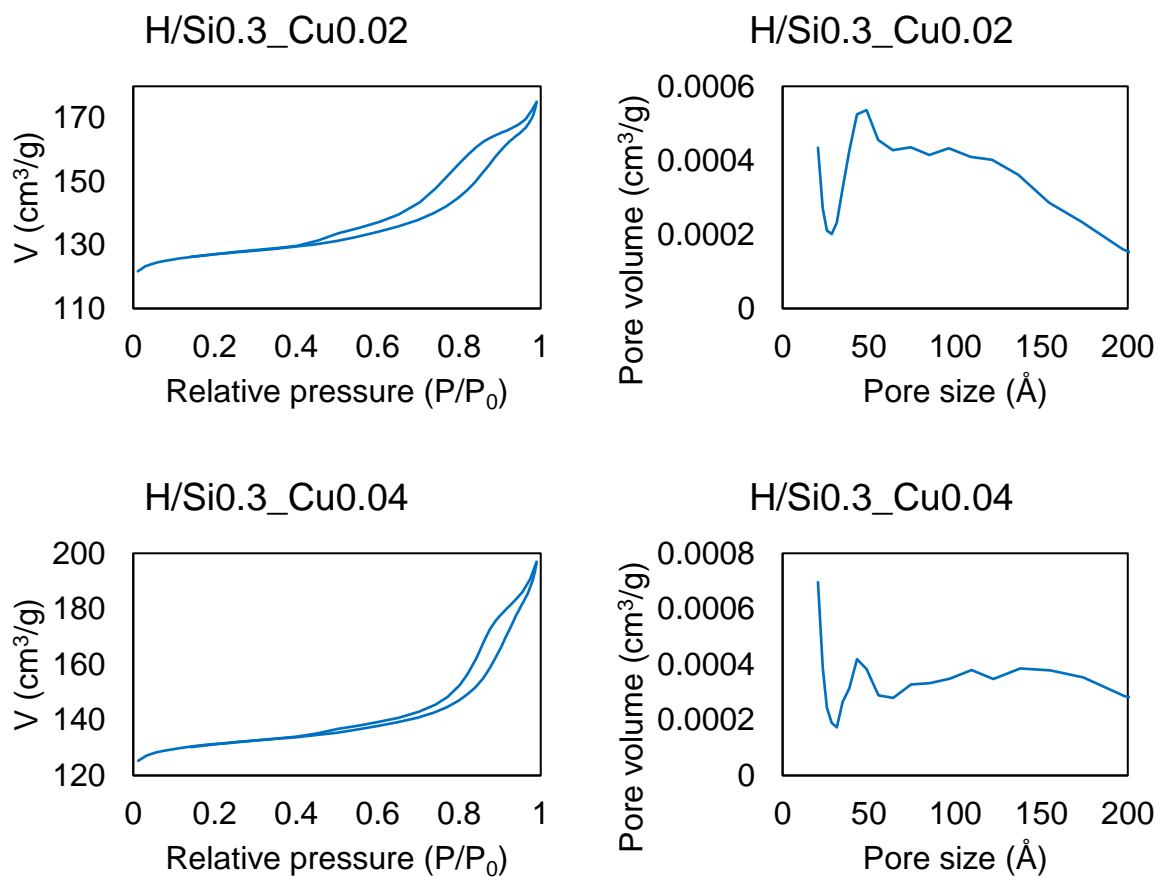


Figure 4-24: N₂ adsorption-desorption isotherm(left) and BJH plot(right) for H/CuSAPO-34 samples synthesised with Si/Al=0.3

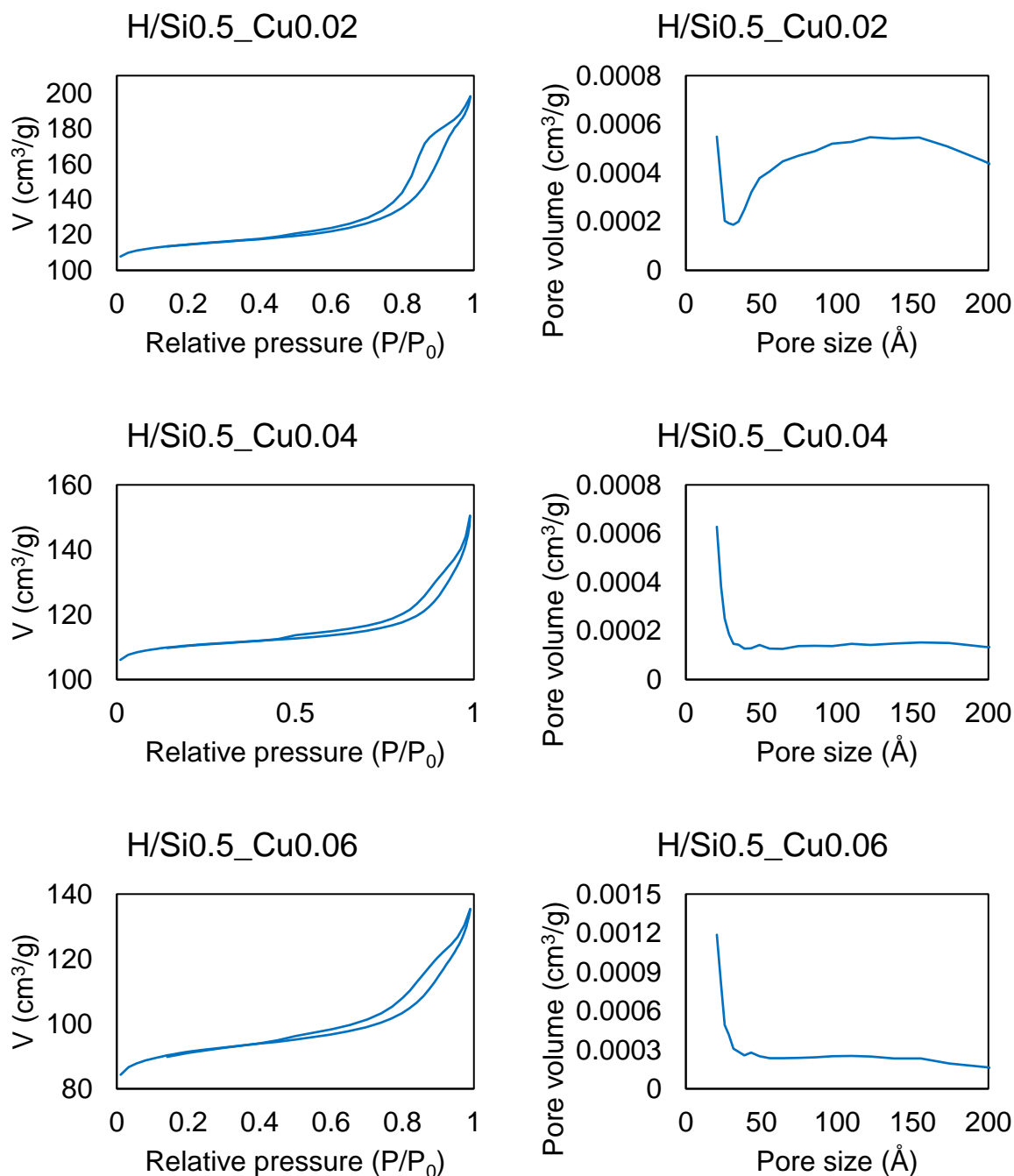


Figure 4-25: N₂ adsorption-desorption isotherm(left) and BJH plot(right) for H/CuSAPO-34 samples synthesised with Si/Al=0.5

From the N₂-physorption it appears that the selected H/CuSAPO-34 made with CTAOH and varying Cu and Si content are all hierarchical with mostly disordered mesopores. Variation of both surface areas and pore volumes are observed with changes in Cu and Si content, but no clear trend could be drawn

4.3 Scanning electron microscopy(SEM)

4.3.1 H/SAPO-34

SEM-images taken for H/GLU0.05 are shown in Figure 4-26. It appears that most of the crystallites are in the size range 10-30 μm , but there were also large aggregates with sizes larger than 50 μm . H/GLU0.05 therefore has significantly larger particles sizes compared to conventional SAPO-34, which commonly has crystallites sizes close to 1 μm ⁵⁵.

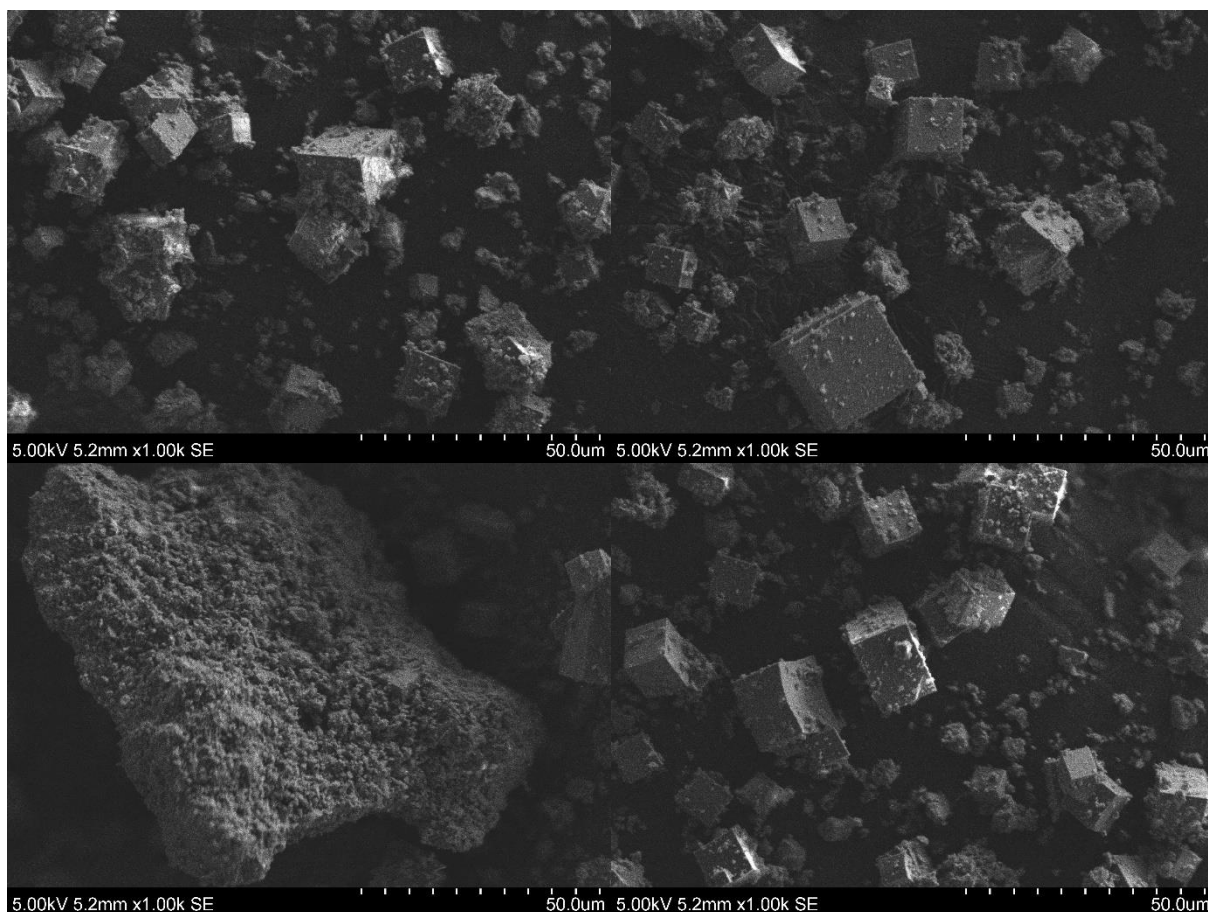


Figure 4-26: SEM-images of H/GLU0.05

4.3.2 C/CuSAPO-34 and H/CuSAPO-34

SEM imaging was also performed for copper containing SAPO-34 samples, with the averages particle sizes obtained shown in Figure 4-27 and an image of each sample shown in Figure 4-28. Additional SEM-images was used to calculate the average crystallite sizes, and these can be found in Appendix C.

For H/Si0.5_Cu0.02, H/Si0.5_Cu0.04 and H/Si0.5_Cu0.06 a trend of increasing particle size with increased Cu/Al is observed. Evaluating the SEM images, it also appears that increasing Cu/Al yields more irregular particles, with H/Si0.5_Cu0.02 having mostly cubic particles and

H/Si0.5_Cu0.06 having highly irregular particles. For C/Si0.3_Cu0.04 the particles size is slightly smaller compared to H/Si0.5_Cu0.04, which both were made with Cu/Al=0.04. However, since the Si/Al ratio used is different between these samples it is not a perfect comparison, and caution should be had stating any crystallite differences between C/CuSAPO-34 and H/CuSAPO-34. The crystallite size of all C/CuSAPO-34 and H/CuSAPO-34 samples presented here are larger than what is common for C/SAPO-34⁵⁵.

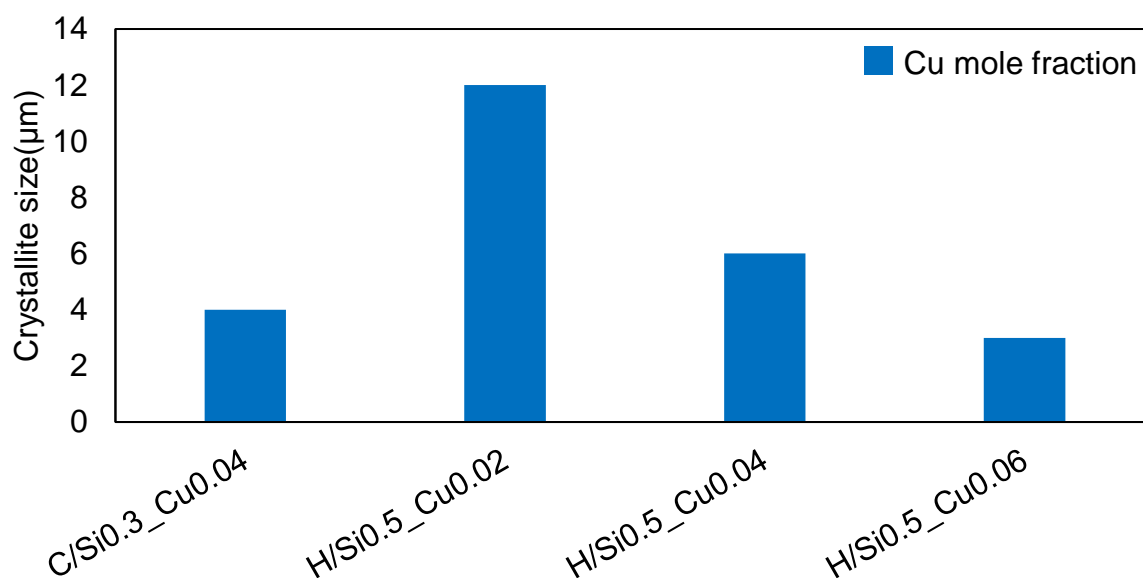


Figure 4-27: Average particle sizes for C/Si0.3_Cu0.04 and H/CuSAPO-34 samples made with Si/Al=0.5 and varying copper content

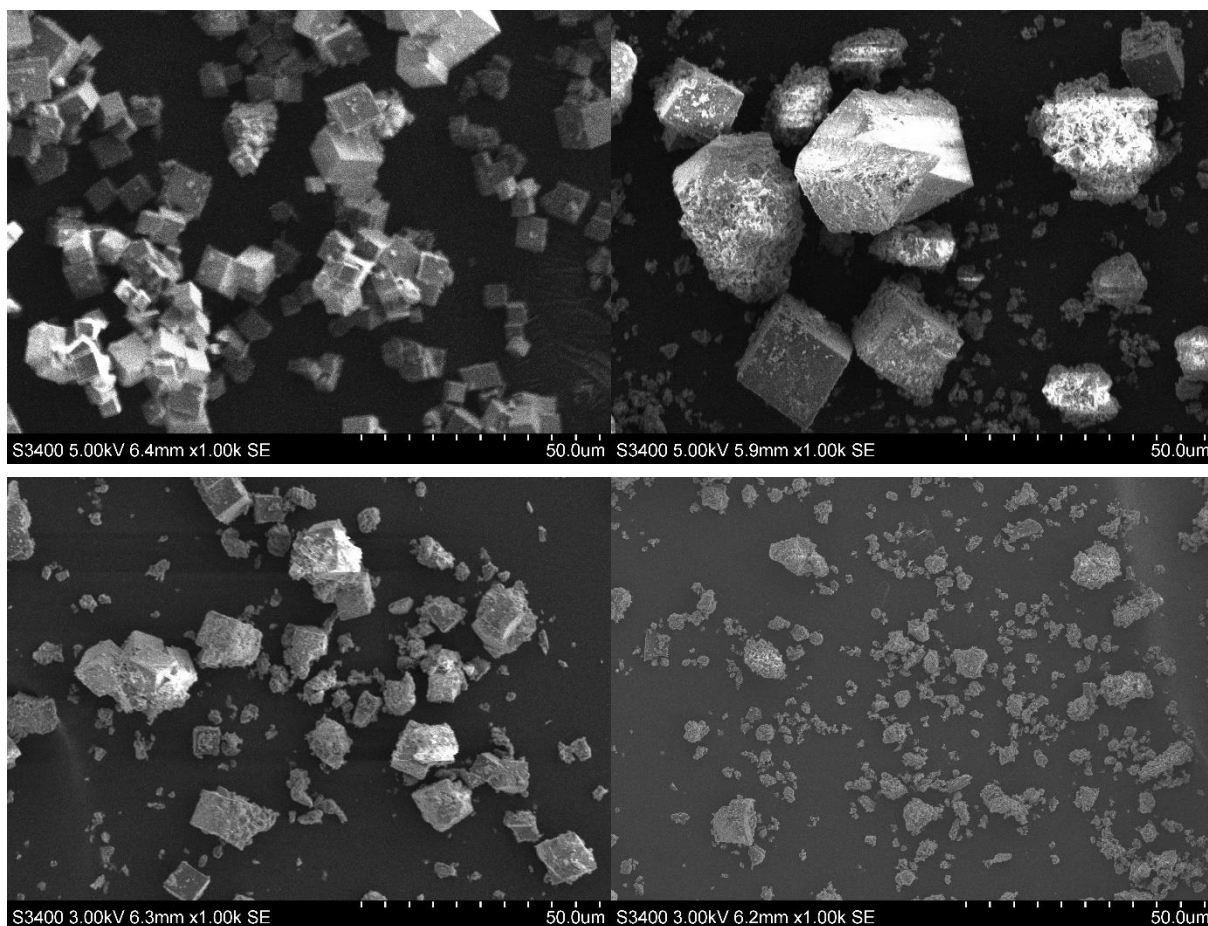


Figure 4-28: Show the SEM images of C/Si_{0.3}_Cu_{0.04}(Top left), H/Si_{0.5}_Cu_{0.02}(Top right), H/Si_{0.5}_Cu_{0.04}(Bottom left), H/Si_{0.5}_Cu_{0.06}(Bottom right)

4.4 ICP-MS

ICP-MS was performed to determine the amount of copper present in calcined C/CuSAPO-34 and H/CuSAPO-34 samples. The copper content obtained from ICP-MS analysis of the samples with Si/Al=0.3 and Si/Al=0.5 are shown in Figure 4-29 and Figure 4-30, respectively. For all samples the mole fraction of Cu from ICP-MS is significantly higher than the mole fraction of Cu used in the synthesis mixture. The copper content in the sample is also seen increasing with the amount of Cu added during synthesis, and from ICP-MS results alone there appear to be no upper limit to uptake of copper.

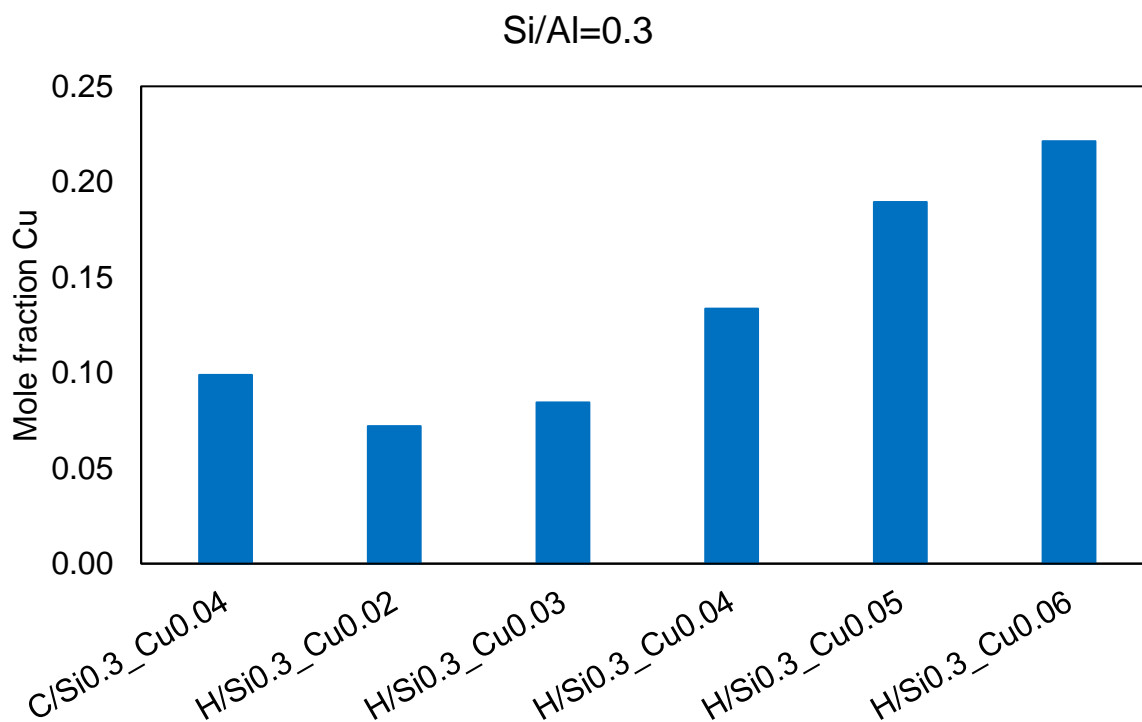


Figure 4-29: Cu/Al from ICP-MS for calcined samples synthesised with Si/Al0.3

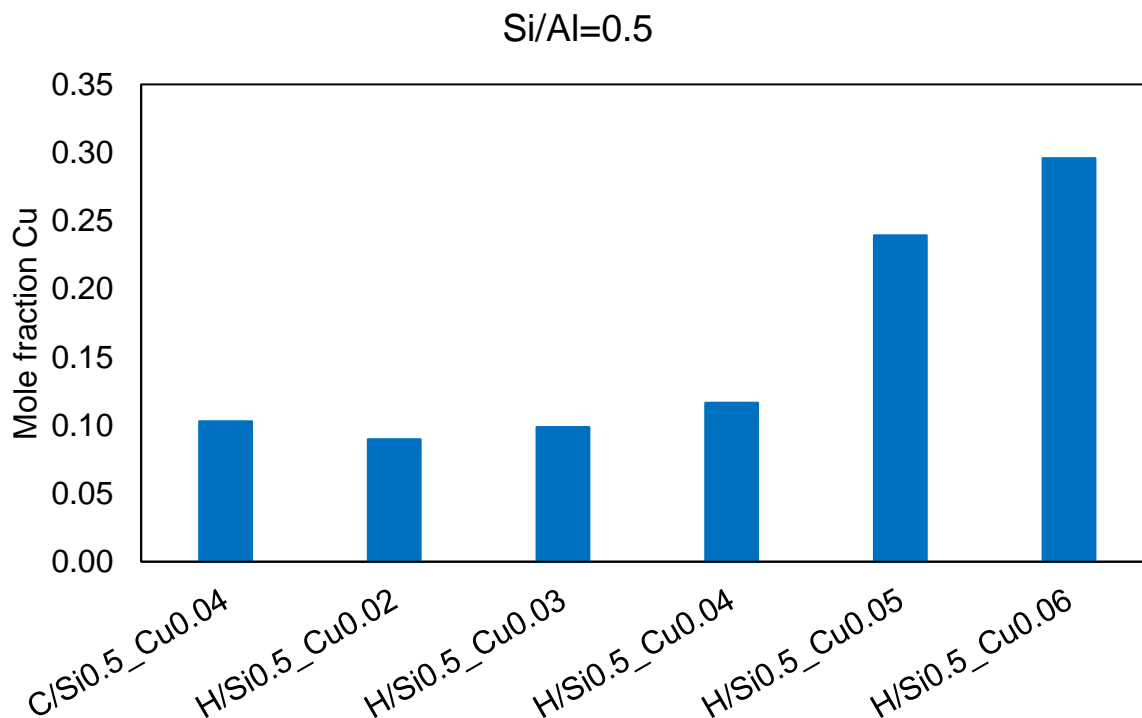


Figure 4-30: Cu/Al from ICP-MS for calcined samples synthesised with Si/Al0.5

4.5 CO-adsorption

CO-adsorption was performed for hierarchical SAPO-34 with and without copper. For H/SAPO-34 this was done to determine whether Bronsted acid sites were present, ascertain their acid strength and detect any anomalous acid properties compared to conventional SAPO-34. For H/CuSAPO-34 CO-adsorption was performed mainly to detect whether acid sites arising from incorporated copper were present, in addition to the general investigation of acid properties.

4.5.1 H/SAPO-34

CO-adsorption was performed by Daniel Ali(IKJ) for H/150°C_120h to investigate the acid properties of this sample. The Bronsted region is shown in Figure 4-31, with spectra measured prior to and during CO-adsorption. In the spectrum measured at vacuum the doublet observed at 3627cm⁻¹ and 3606cm⁻¹ is assigned to Bronsted acid sites, and the peaks at 3677cm⁻¹, 3735⁻¹, and 3745⁻¹ are assigned to terminating P-OH, Si-OH, and Al-OH respectively⁵⁷. The intensity of the peaks arising from the terminating groups is significantly higher than what is common for SAPO-34^{57, 67}.

With increasing CO-pressure, the Bronsted acid site band decreases in intensity. Simultaneously a band appears at 3359cm⁻¹ which is assigned to Bronsted acid sites with CO adsorbed⁵⁷. This shift of the Bronsted acid band is a measure of the acid strength and is measured to be 276cm⁻¹ for this sample. This is in good accordance with values reported for conventional SAPO-34⁵⁷.

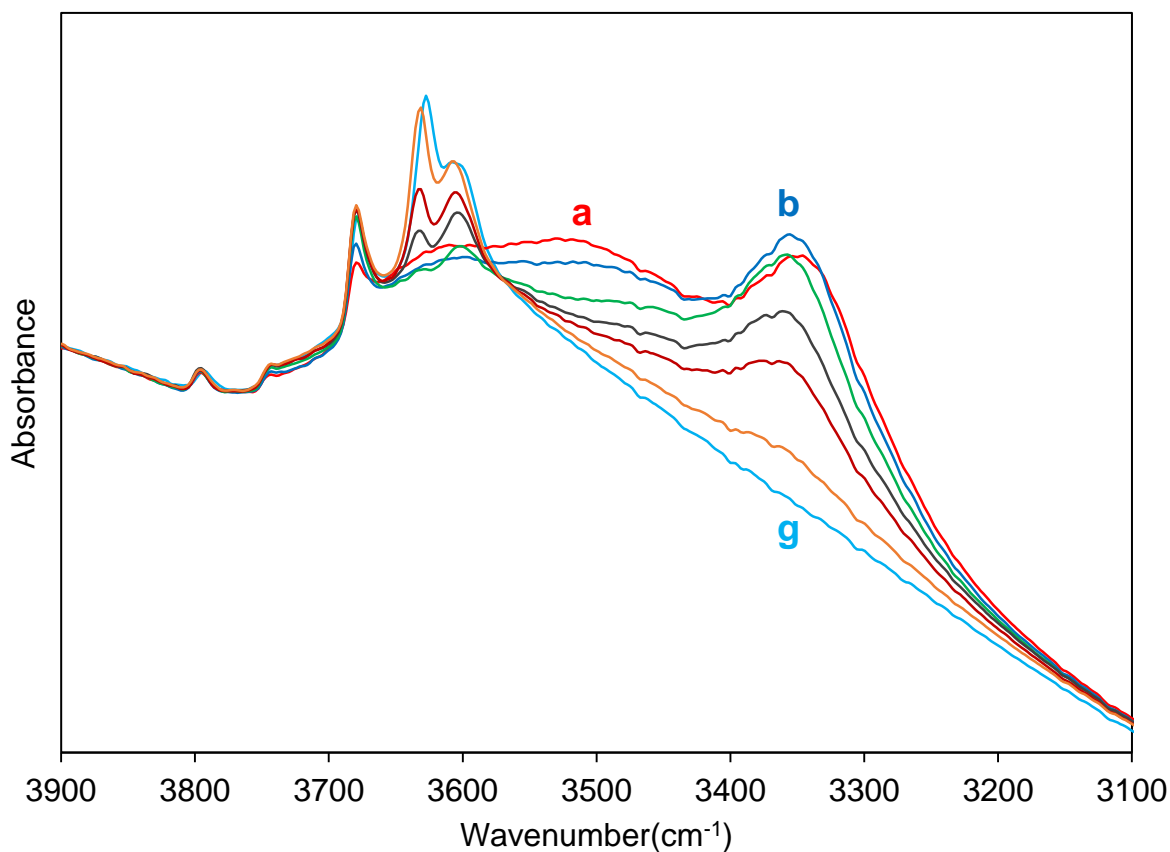


Figure 4-31: The Bronsted region with spectra measured at a CO pressure of: a) 3.7 mbar, b) 0.53 mbar, c) 0.051 mbar, d) 0.033 mbar, e) 0.020 mbar, f) 0.019 mbar, g) vacuum

In Figure 4-32 the CO-region of the spectra measured during the CO experiments are shown. With increasing CO-pressure, the first band to arise is found at 2171cm^{-1} and is assigned to CO polarised by strong Bronsted acid sites. The second band to arise occurs at 2159cm^{-1} and is assigned to CO polarised by weaker Bronsted acid sites. The band found at 2140cm^{-1} , arises at high CO-pressures and is assigned to physisorbed CO⁵⁷. Overall, the bands that arise in the CO-region is in accordance with what has been reported for conventional SAPO-34⁵⁷.

To summarise, the acid properties of H/150°C_120h appears to be in accordance with what has been reported for conventional SAPO-34. The only difference found was high intensity of terminating surface groups.

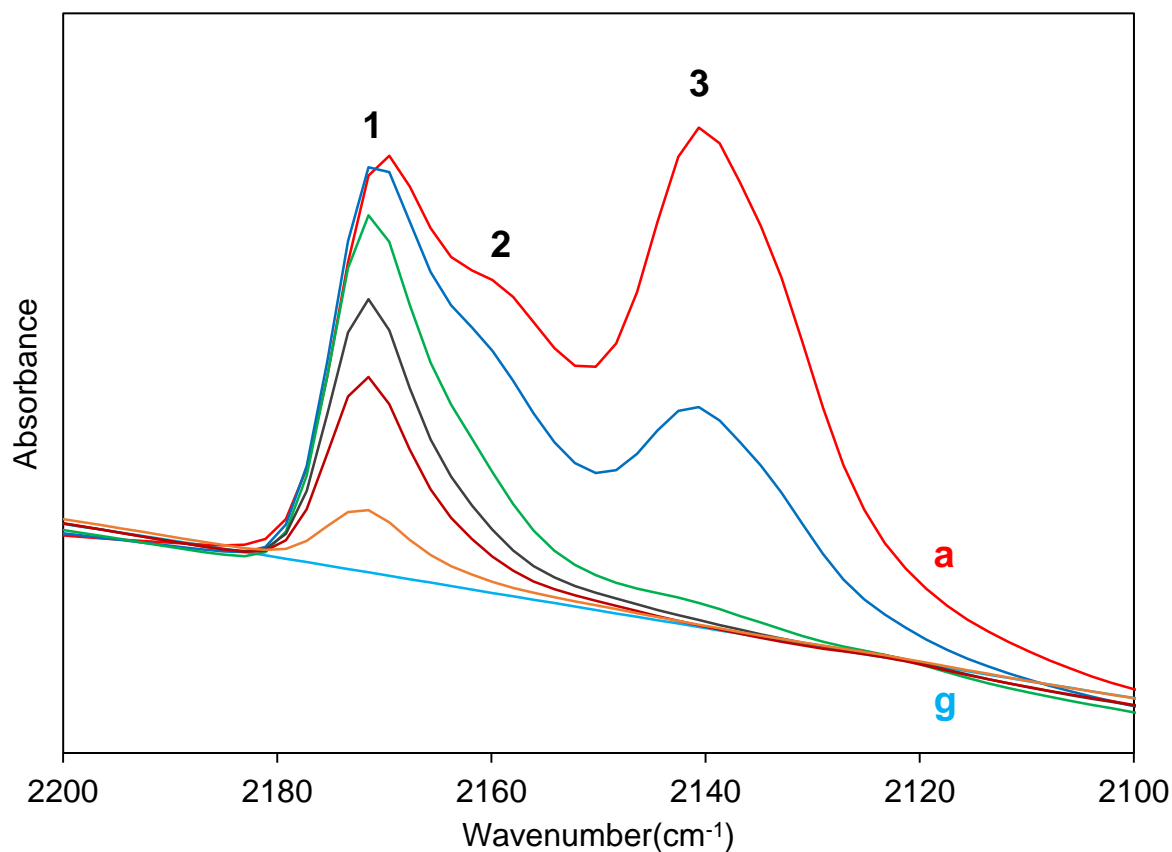


Figure 4-32: The CO-region with spectra measured at a CO pressure of: a) 3.7 mbar, b) 0.53 mbar, c) 0.051 mbar, d) 0.033 mbar, e) 0.020 mbar, f) 0.019 mbar, g) vacuum. The bands detected are found at: 1. 2171cm^{-1} , 2. 2159cm^{-1} , and 2140cm^{-1} .

4.5.2 C/CuSAPO-34 and H/CuSAPO-34

Co-adsorption was done for H/Si_{0.3}Cu_{0.04}, with the Bronsted region shown in Figure 4-33 and the CO-region shown in Figure 4-34.

In the Bronsted region the doublet arising from Bronsted sites with high and low acid strength is observed at 3627cm^{-1} and 3604cm^{-1} , and the shift of the high strength acid sites is measured to be 264cm^{-1} . These values are in good accordance with what was reported by for conventional SAPO-34 by Bordiga et al.⁵⁷. No bands arising from Cu-Bronsted sites were detected.

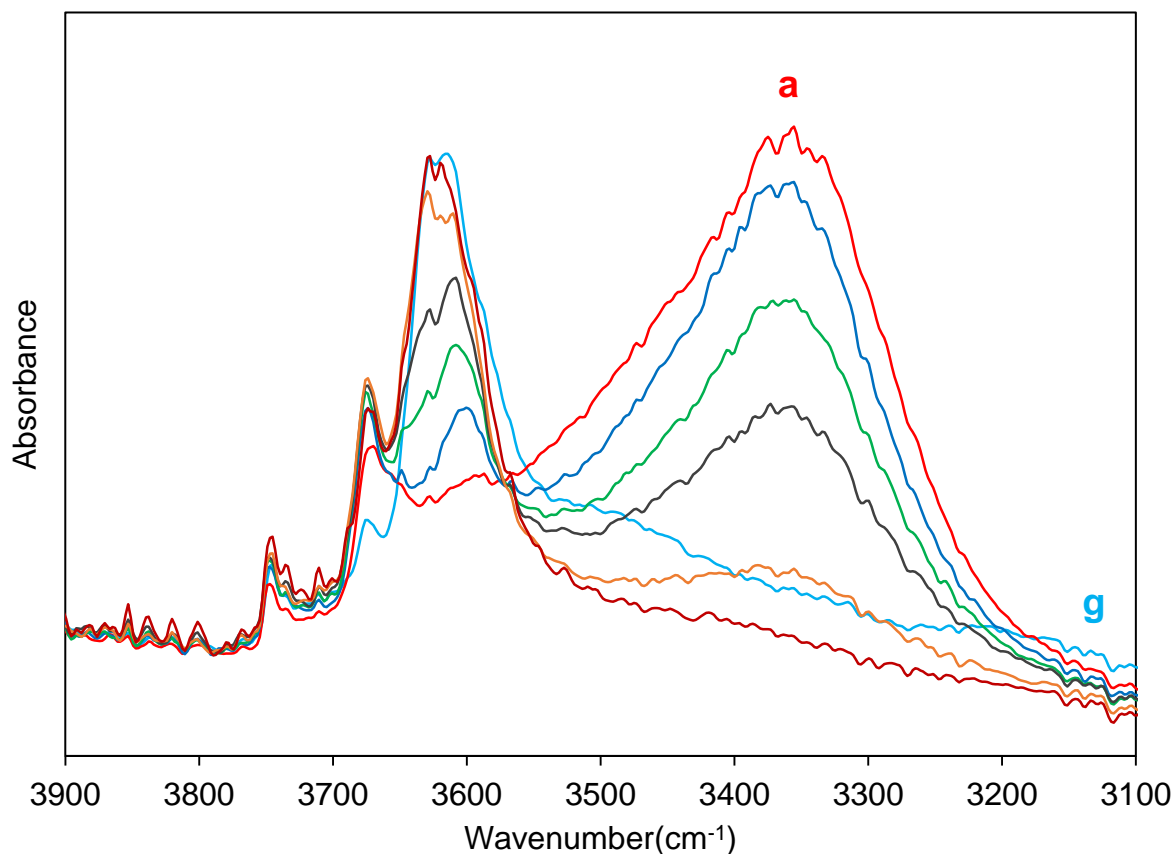


Figure 4-33: The Bronsted region with spectra measured at a CO pressure of: a) 3.0 mbar, b) 0.068 mbar, c) 0.037 mbar, d) 0.026 mbar, e) 0.015 mbar, f) 0.0002 mbar, g) vacuum

In the CO-region the characteristic bands that appear for SAPO-34 are all present. These are the bands appearing at 2177cm^{-1} and 2157cm^{-1} , ascribed to CO bound to high and low frequency Bronsted acid sites. At higher CO-pressure, these bands combine to form the band located at 2165cm^{-1} . The band that is observed at 2142cm^{-1} is assigned to physisorbed CO, and this band normally decreases in intensity with decreasing CO pressure. However, in this case the band does not decrease in intensity but is rather shifted to higher frequencies as CO-pressure is reduced. At a CO pressure of 0.000065 the band is found at 2154cm^{-1} , which is the frequency reported for Cu^+ -CO species⁶⁸.

The two-remaining bands appearing at 2217cm^{-1} and 2186cm^{-1} most likely arise due to CO interacting with copper. Based on work done by Szanyi et al.⁶⁹, the 2217cm^{-1} is ascribed to CO bound to Cu^{2+} . The band at 2186cm^{-1} is ascribed to $\text{Cu}^+(\text{CO})_3$, as was done by Cortés Reyes et al.⁵⁸.

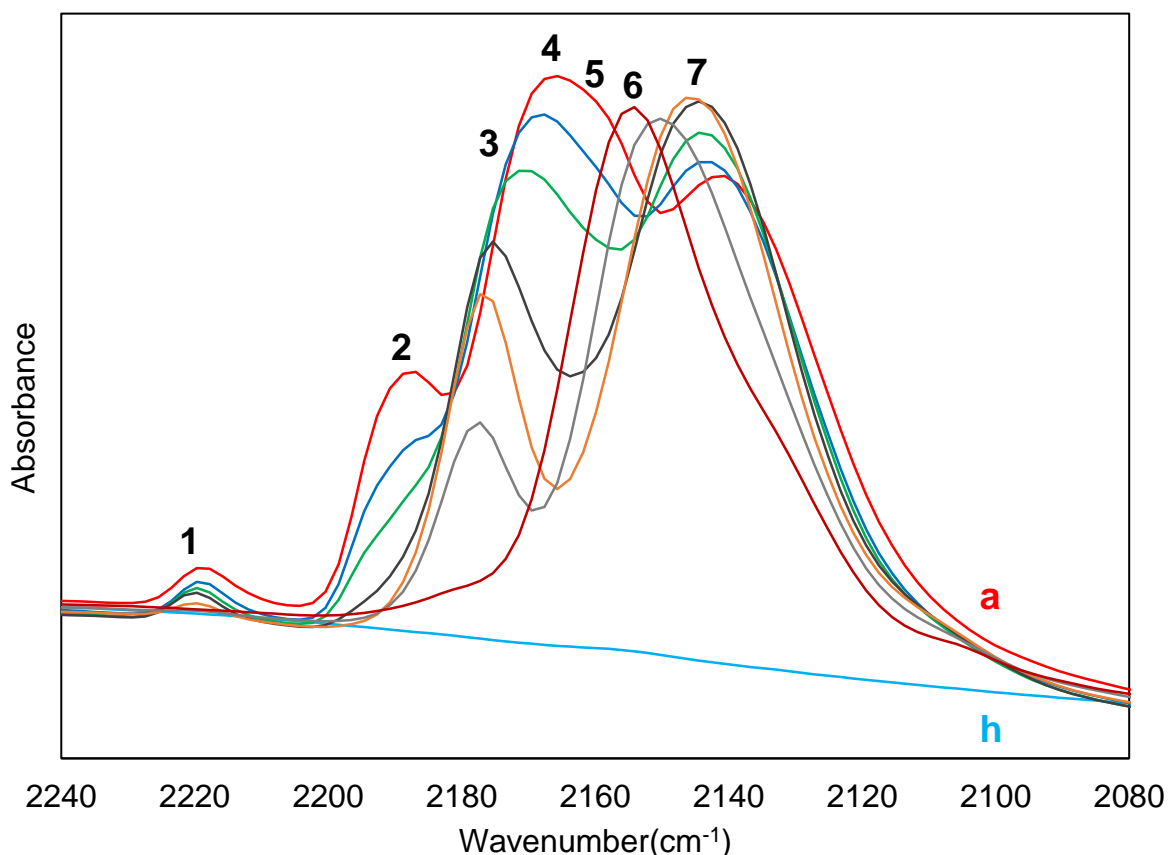


Figure 4-34: The CO-region with spectra measured at a CO pressure of: a) 3.0mbar, b) 0.1mbar, c) 0.045mbar, d) 0.019mbar, e) 0.0082mbar, f) 0.00033mbar, g) 0.0000065mbar, h) vacuum. The bands detected are found at: 1. 2217 cm^{-1} , 2. 2186 cm^{-1} , 3. 2175 cm^{-1} , 4. 2165 cm^{-1} , 5. 2157 cm^{-1} , 6. 2154 cm^{-1} , 7. 2142 cm^{-1}

Based on the results of CO adsorption, H/Si0.3_Cu0.04 has the characteristic Bronsted acid sites found in SAPO-34. From the CO-region there are two bands that potentially arise due to CO interacting with Cu^+ , and a band that arises from interactions between CO and Cu^{2+} . There were not found any bands which could be assigned to Bronsted sites arising from incorporated copper.

4.6 MTH

MTH was performed for hierarchical SAPO-34 with and without copper. This was done to determine the catalytic activity, and by comparing to reported activities of conventional SAPO-34, the effect mesopores has on catalytic activity can be ascertained.

4.6.1 H/SAPO-34

The samples H/GLU0.05 and H/150°C_120h were tested for the MTH reaction, since these were the most promising hierarchical samples. The experiment for H/150°C_120h was conducted by PhD candidate Daniel Ali (IKJ). For both samples the results were poor, with H/GLU0.05 being completely inactive and H/150°C_120h having a conversion of 21% after 10min, and subsequently deactivating completely. This is significantly worse than the conventional SAPO-34⁷⁰.

Bronsted acid sites are present in both samples, as can be seen from the DRIFTS spectra in Figure 4-35 and Figure 4-36. This makes the poor performance peculiar, since the Bronsted acid sites are the active sites for the MTH reaction. During the MTH reaction the common trend of the Bronsted acid sites is to shift to lower wavenumbers and decrease in intensity⁶⁷. This trend is not seen for H/GLU0.05 and H/150°C_120h, with the acid sites being shifted to lower wavenumber, but not decreasing in intensity. In fact, for H/GLU0.05 the intensity of the acid site peak increases during the MTH reaction. The shift of the acid sites occurs rapidly, with only small changes occurring after 10 min for both samples.

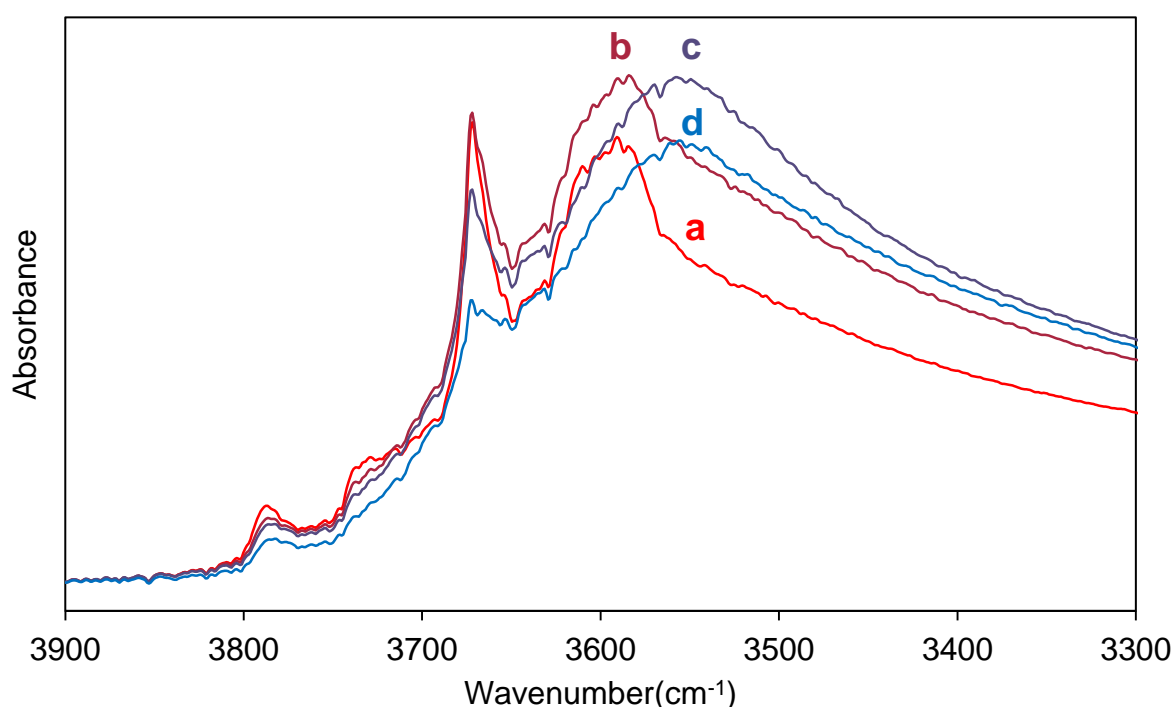


Figure 4-35: The Bronsted acid site region of H/150°C_120h during MTH after: a) 0min, b) 2min, c) 10min, d) 4h 30min.

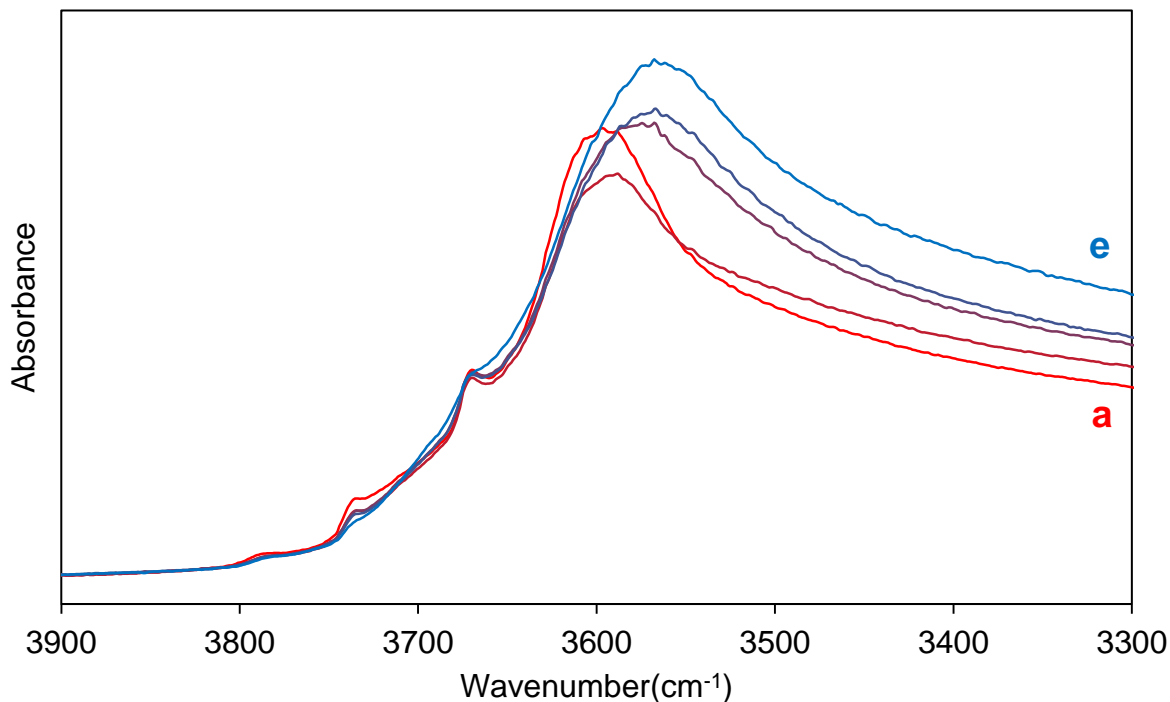


Figure 4-36: The Bronsted acid site region of H/GLU0.05 during MTH after: a) 0min, b) 2min, c) 4min, d) 6min, e) 2h 20min.

4.6.1.1 N₂-physisorption post MTH of H/GLU0.05

To detect if any changes had occurred to the pore structure of H/GLU0.05 during MTH, N₂-physisorption was performed. The results obtained were that the surface area was greatly reduced from 470 m²/g prior to MTH to 80 m²/g after MTH. The values obtained for micro and mesopore fractions could not be used for the sample after MTH, since a negative micropore fraction was obtained for both surface area and pore volume. However, the shape of the adsorption isotherm shown in Figure 4-37 is a type 4 isotherm, which occurs in mesoporous solids⁵⁰. This means that the sample after MTH mainly contains mesopores while the micropores have been clogged up. This points towards rapid coke formation being the reason for the poor performance of the samples, but not why the samples deactivated so rapidly.

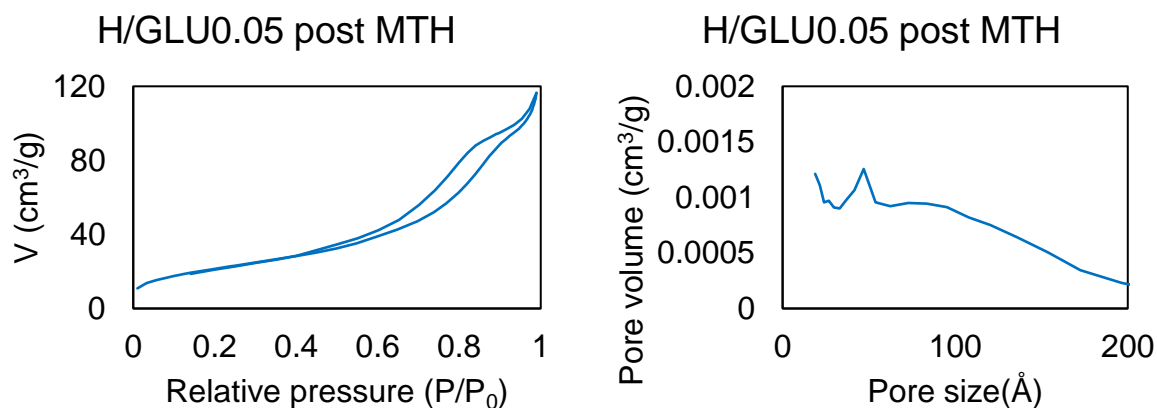


Figure 4-37: The N₂ adsorption-desorption isotherm(left) and BJH plot(right) for H/GLU0.05 post MTH

4.6.2 C/CuSAPO-34 and H/CuSAPO-34

The samples C/Si0.3_Cu0.04 and H/Si0.3_Cu0.04 were tested as catalysts for the MTH reaction. The activity of both catalysts was poor, with the H/Si0.3_Cu0.04 being completely inactive, and C/Si0.3_Cu0.04 having a methanol conversion of 16% after 44min and subsequently being completely deactivated. This is very similar to the results obtained for the conventional and hierarchical samples without copper. The shift of the acid sites of both samples is also very similar, as can be seen in Figure 4-38 and Figure 4-39. The Bronsted acid site band can be seen first decreasing in intensity, followed by an increase in intensity and shift to higher frequencies. This is not the behaviour that has been reported previously, where the band decreases significantly in intensity in addition to being shifted to higher frequencies⁶⁷.

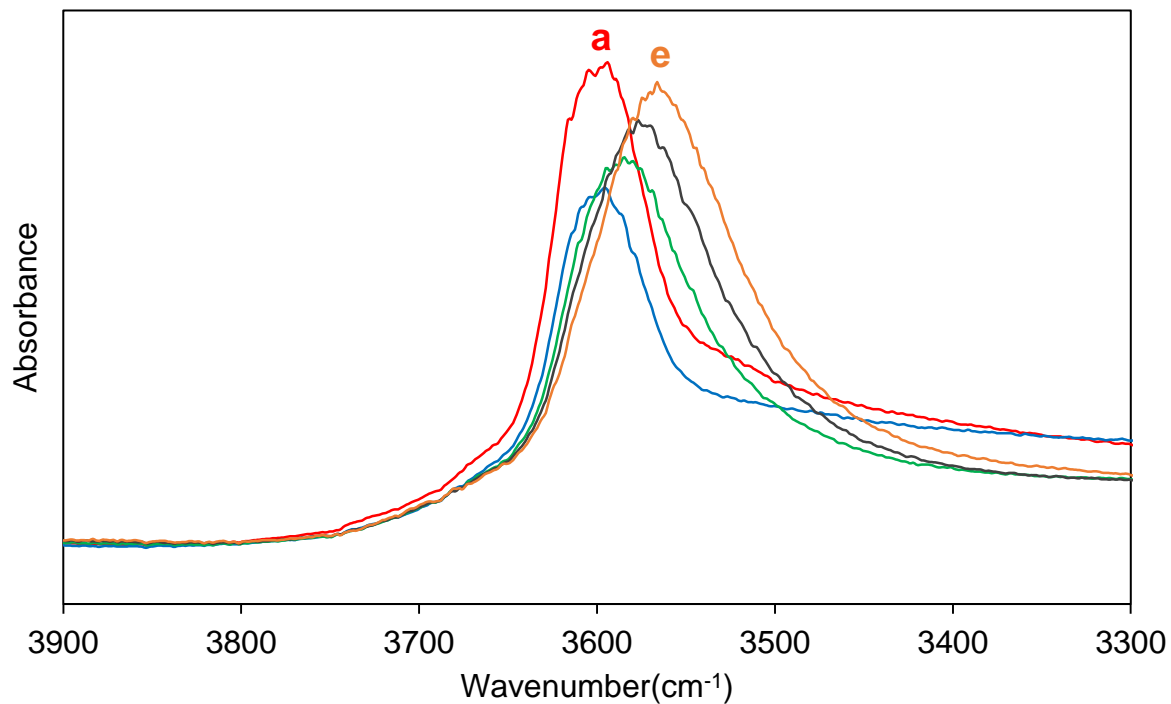


Figure 4-38 The Bronsted acid site region of C/Si_{0.3}_Cu_{0.04} during MTH after: a) 0min, b) 2min, c) 50min, d) 52min, e) 2h 24min

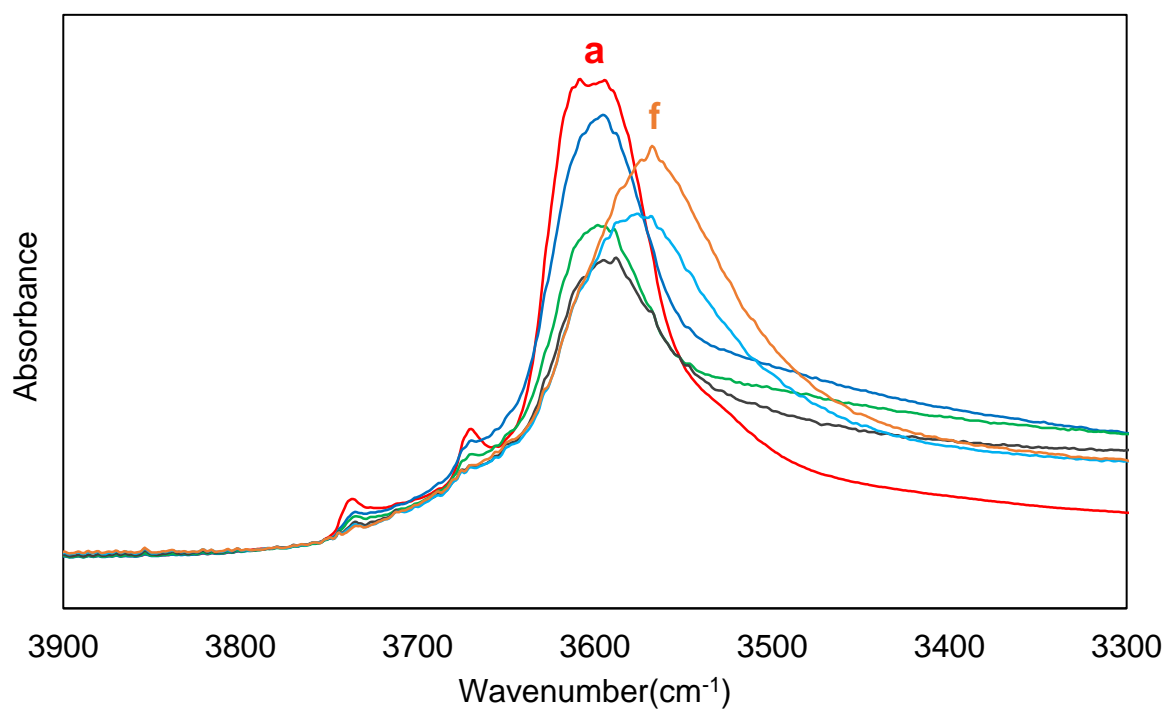


Figure 4-39: The Bronsted acid site region of H/Si_{0.3}_Cu_{0.04} during MTH after: a) 0min, b) 30sec, c) 2min, d) 50min, e) 58min, f) 2h 2min

4.6.2.1 N₂-physisorption post MTH

For the H/Si_{0.3}_Cu_{0.04} N₂-physisorption was done on sample post reaction, post reaction with flushing of He for 16hours, and post reaction with burn off in air at 350°C. The results from the N₂-physisorption is summarised in Figure 4-40.

After the MTH reaction the surface area is greatly reduced, and this reduction appears to due to clogging of micropore, as can be seen from the micropore volumes (blue column). The non-micropore volume is hardly changed, which indicates that the mesopores are left unaltered by the MTH reaction.

The flushing in He appears to generate a small fraction of the micropores, as seen from slight increase in micropore volume. After heating in air, all pores are regenerated as seen from the total surface area.

For the C/Si_{0.3}_Cu_{0.04} the result of N₂-physisorption pre MTH and post flushing are shown in Figure 4-41. Similarly, to the H/Si_{0.3}_Cu_{0.04}, the surface area of the sample is significantly reduced due to blocking of micropores.

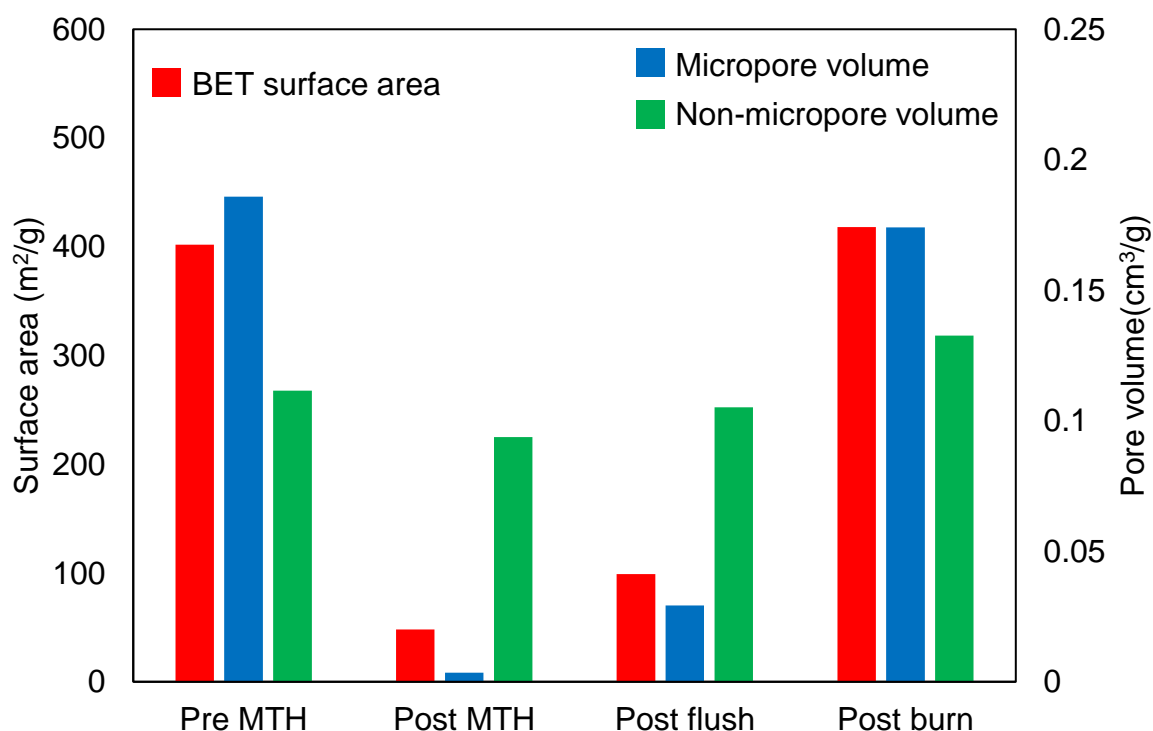


Figure 4-40: The BET surface area, micropore volume and non-micropore volume for H/Si_{0.3}_Cu_{0.04} pre and post MTH and post flush and burn.

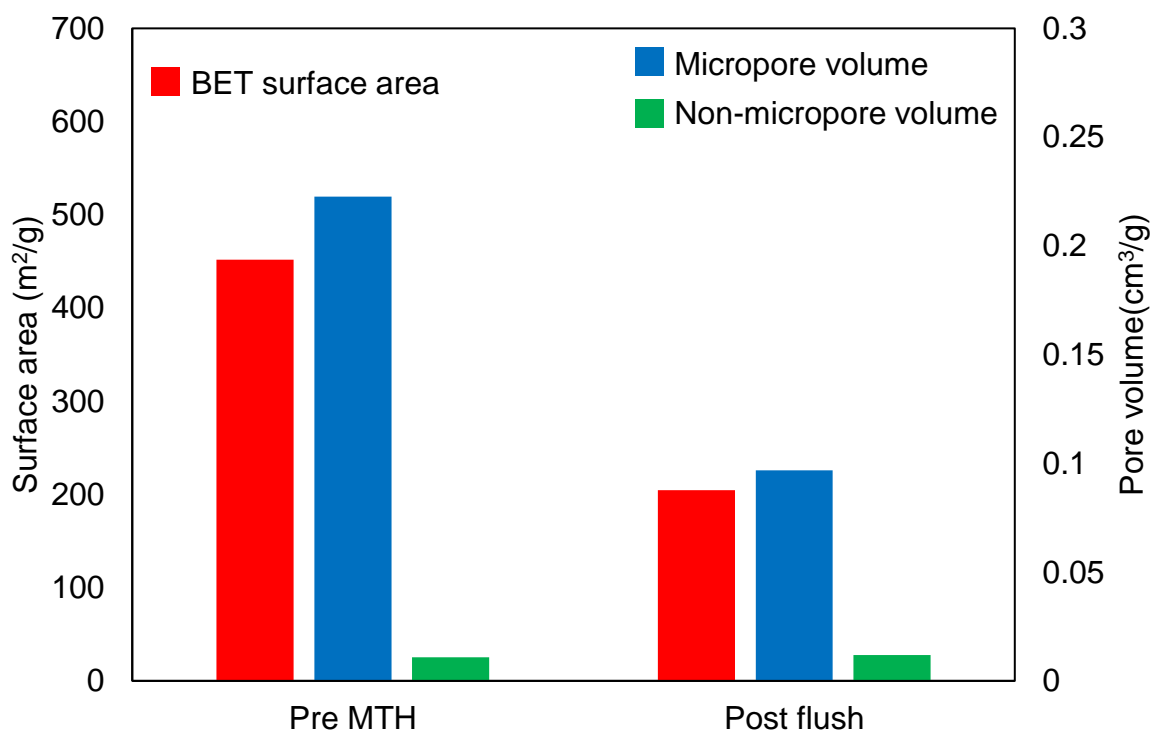


Figure 4-41: The BET surface area, micropore volume and non-micropore volume for C/Si_{0.3}_Cu_{0.04} pre MTH and post flushing

To summarise, the Bronsted acid in the two samples do not decrease in intensity during MTH as has been reported for conventional SAPO-34. Both samples had poor activity and deactivated rapidly due to blocking of the micropores. The mesopores in H/Si_{0.3}_Cu_{0.04} are not altered during MTH.

4.7 XAS

XAS was performed for as prepared and calcined H/CuSAPO-34 and C/CuSAPO-34 samples, as well as for post HC-SCR samples. For post HC-SCR samples tested in dry feed /HCd will be added to the name of the sample and /HCw will be added for samples tested in wet feed. XAS was done to elucidate the oxidation state, coordination, and local environment of Cu. The information obtained will be used to determine whether copper has been successfully incorporated, and if any changes occurred during HC-SCR.

Ex-situ XAS measurements were done for the samples shown in Table 4-7. In addition, in-situ XAS was done during temperature programmed reduction (TPR) of C/Si_{0.3}_Cu_{0.04}. The references that will be used for fingerprint analysis of XANES are Cu-foil, Cu₂O, and CuO.

Table 4-7: The samples and state of the samples that Ex-situ XAS measurements were performed for. ✓ indicates that measurements were performed and ✗ indicates that measurements were not performed.

Sample name	State			
	As prepared	Calcined	Post HC-SCR(dry)	Post HC-SCR(wet)
C/Si0.3_Cu0.04	✓	✓	✗	✗
H/Si0.3_Cu0.04	✓	✓	✗	✗
H/Si0.5_Cu0.02	✓	✓	✓	✗
H/Si0.5_Cu0.04	✓	✓	✓	✓
H/Si0.5_Cu0.06	✓	✓	✓	✗

4.7.1 XANES

From the XANES information about the oxidation state and coordination of copper can be obtained. For samples E_0 is designated as half way up the normalised XANES, and the values obtained can be compared to the E_0 values of the references with known oxidation states. The E_0 values for all Ex-situ samples are plotted on a linear trendline generated from the E_0 values of Cu-foil, Cu_2O and CuO is shown in Figure 4-42. All samples appear between a oxidation state of Cu^+ and Cu^{2+} , with As prepared samples appearing closer to Cu^+ compared to the calcined samples. Comparing the calcined samples with the post HC-SCR samples there appears to be a very slight shift towards Cu^+ for the post HC-SCR samples

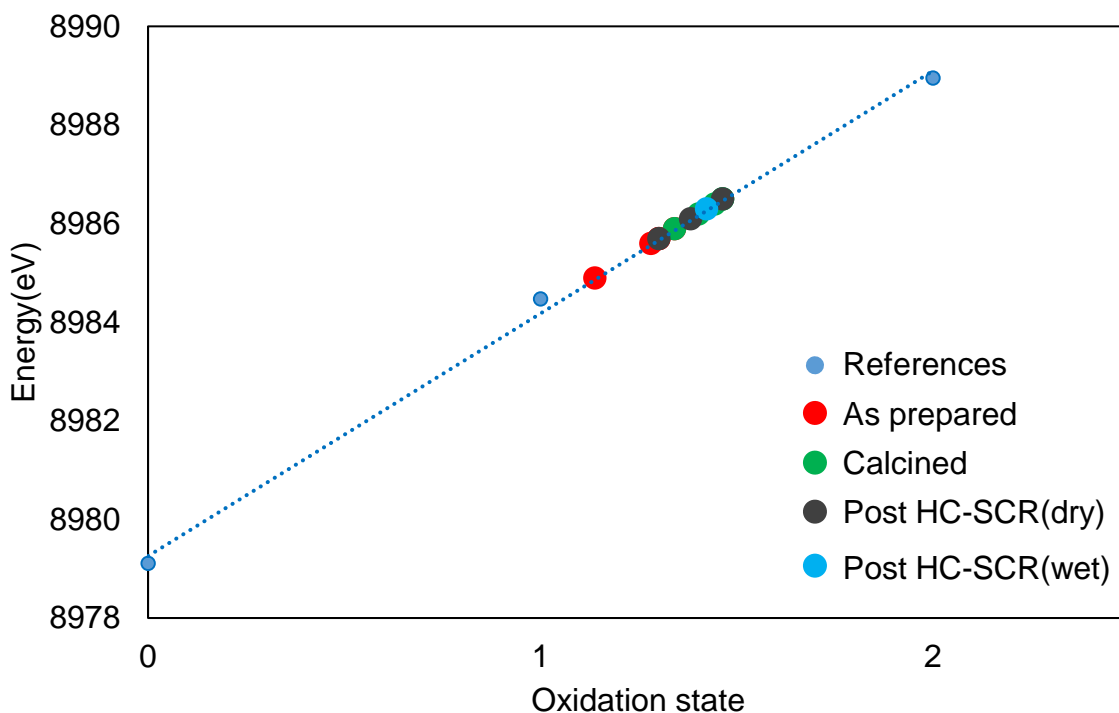


Figure 4-42: E_0 values of all Ex-situ samples plotted on the linear trendline obtained from the E_0 values of the reference compounds, Cu-foil, Cu_2O , and CuO .

4.7.1.1 As prepared samples

The shape of the XANES can also be used to determine the oxidations state of copper as well as the coordination of copper. By comparing the XANES of samples and references it was observed that the samples did not match any of the references completely. To exemplify this the XANES and first derivative XANES of C/Si0.3_Cu0.04 and H/Si0.5_Cu0.06/AP is shown in Figure 4-43, while the XANES plots for H/Si0.3_Cu0.04, H/Si0.5_Cu0.02, H/Si0.5_Cu0.04 can be found in appendix D.

The XANES of both C/Si0.3_Cu0.04/AP and H/Si0.5_Cu0.06/AP are comparable to the XANES of Cu-foil. However, the shoulder marked with a star is much less intense in the samples compared to Cu-foil. For C/Si0.3_Cu0.04 there also appears a second shoulder, marked with a blue diamond, which is also found in CuO . Based on this and the fact that the oxidations state appeared to be close to Cu^+ , there is most likely a combination of Cu^0 and Cu^{2+} in the as prepared samples.

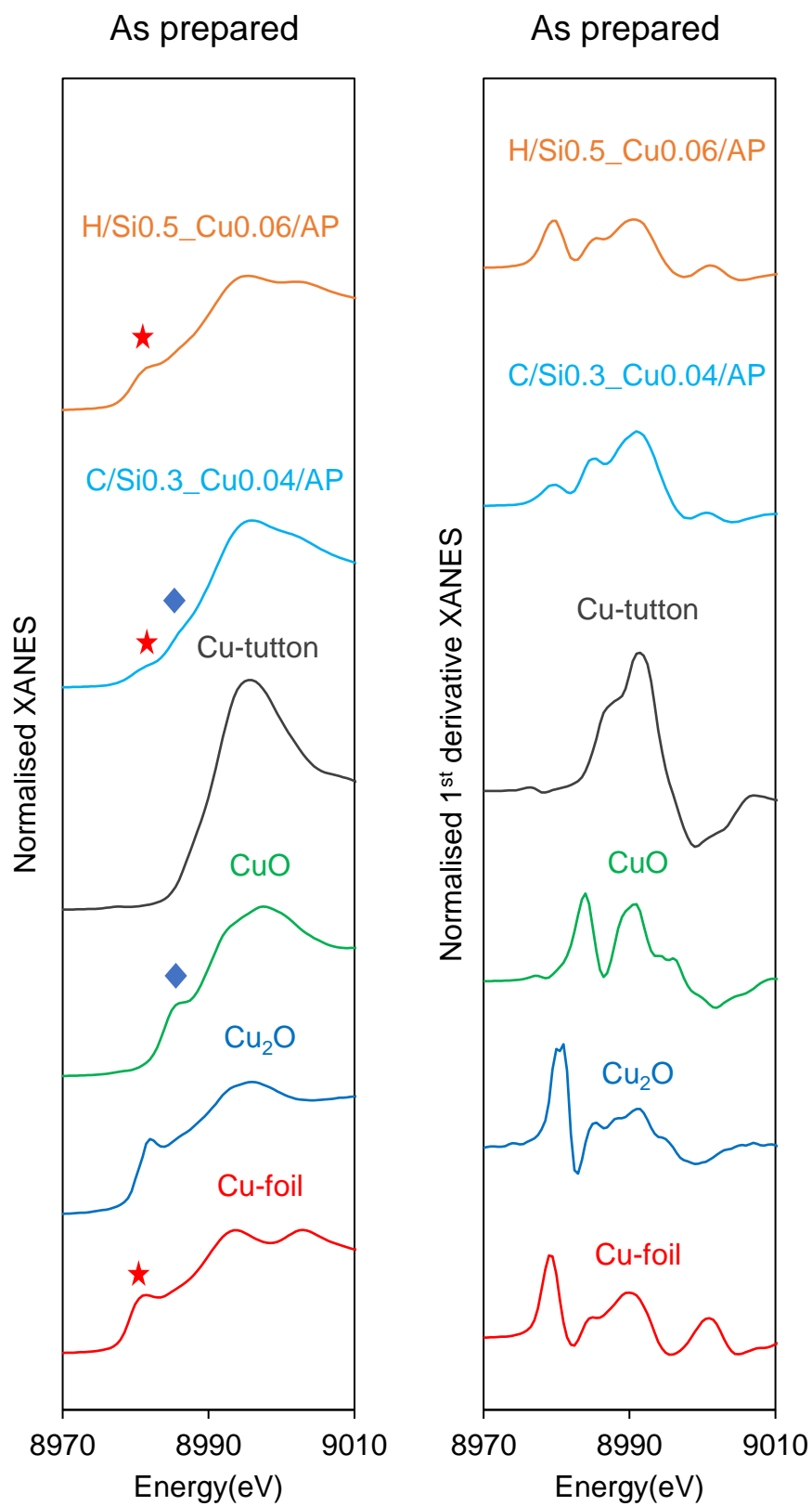


Figure 4-43: Normalised XANES and 1st derivative XANES of C/Si0.3_Cu0.04/AP, H/Si0.5_Cu0.06/AP, and references

To determine the copper-species in the as prepared samples linear combination fitting(LCF) was done. Combinations of all four references shown in Figure 4-43 were tried fitted, with the best fit obtained with a combination of Cu-foil, CuO and Cu-tutton. The relative amounts of copper species obtained are shown in Figure 4-44, and it appears that there is a combination of metallic copper and Cu^{2+} , with the metallic copper contribution increasing with Cu/Al. However, the R-factors had orders of magnitudes of -3, which is higher than what is wanted, and this indicates a low-quality fit.

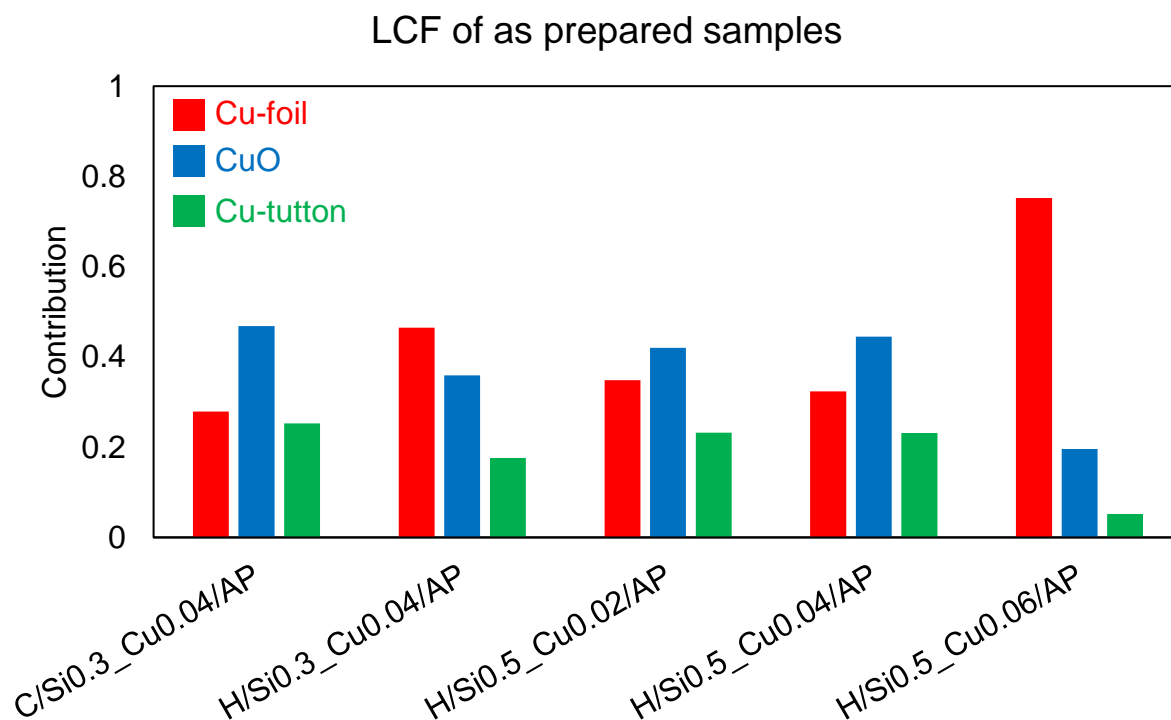


Figure 4-44: Results of LFC for as prepared C/CuSAPO-34 and H/CuSAPO-34 samples. The R-factors are found in Appendix D.

4.7.1.2 Calcined samples

After calcination the XANES of the samples appear to best match the XANES of Cu-tutton, as can be seen for H/Si0.5_Cu0.06 and C/Si0.3_Cu0.04 in Figure 4-45. This is however not a perfect match, due to the shoulder feature in the calcined samples being more intense compared to Cu-tutton.

From the E_0 values of the calcined samples, the apparent oxidation state is closest to Cu^+ . However, there is clearly no Cu^+ in the calcined samples, since Cu^+ gives rise to an intense pre-edge. A possibility is that some metallic copper, which was present in as prepared samples, is not oxidised during calcination. LCF was therefore attempted for the calcined samples, but the fit obtain was poor, with R-factors with orders of magnitude of -1.

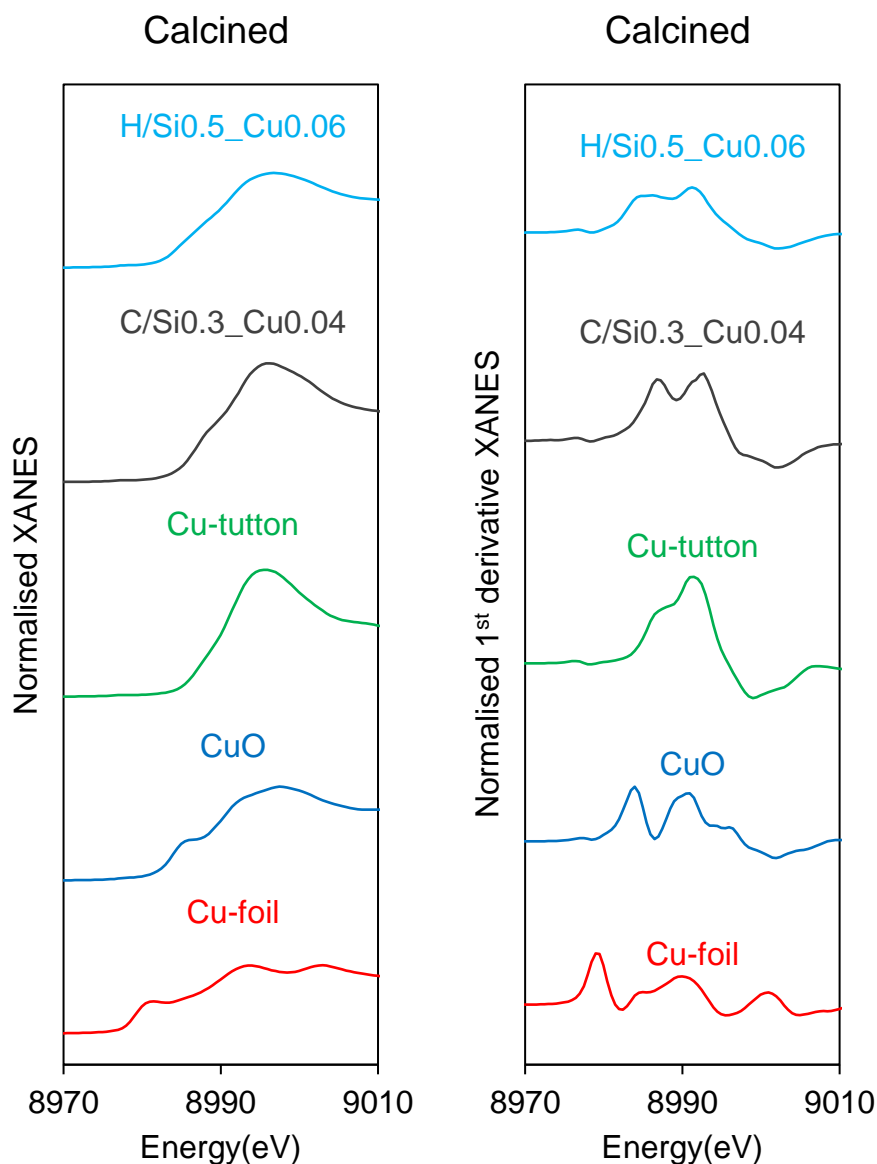


Figure 4-45: Normalised XANES and 1st derivative XANES of C/Si_{0.3}_Cu_{0.04}, H/Si_{0.5}_Cu_{0.06}, and references

4.7.2 EXAFS

In this subsection the results of EXAFS refinement done in DLV EXCURVE will be presented. The information obtained concerns what type of shells surrounding Cu and their distance and multiplicities.

4.7.2.1 As prepared samples

The result for the as prepared samples are summarized in Table 4-8. For all samples, a Cu-O and a Cu-Cu shell was fitted, with the distance of the Cu-Cu shells close to the value for the

Cu-foil (2.457(7)Å). This means that metallic copper is present in the as prepared samples, which was also seen from the XANES.

Table 4-8: The results of EXAFS refinement for as prepared samples, with type of shell, fermi energy, Debye Waller factor, shell distance, and R-factor given

Sample name	Shell	E_F [eV]	$2\sigma^2$ [Å ²]	N	r [Å]	R[%]
C/Si0.3_Cu0.04/AP	Cu-O	-6.5(7)	0.019(4)	4.1(4)	2.04(1)	38.69
	Cu-Cu		0.007(3)	1.1(3)	2.550(6)	
H/Si0.3_Cu0.04/AP	Cu-O	-6.0(9)	0.017(5)	3.1(5)	2.03(1)	39.32
	Cu-Cu		0.012(2)	2.5(5)	2.551(6)	
H/Si0.5_Cu0.02/AP	Cu-O	-6.4(7)	0.016(4)	3.5(4)	2.04(1)	36.67
	Cu-Cu		0.010(3)	1.6(4)	2.550(6)	
H/Si0.5_Cu0.04/AP	Cu-O	-6.4(7)	0.017(7)	3.6(4)	2.04(1)	39.04
	Cu-Cu		0.009(3)	1.4(3)	2.545(6)	
H/Si0.5_Cu0.06/AP	Cu-O	-4(1)	0.012(9)	1.7(6)	2.00(2)	40.40
	Cu-Cu		0.013(2)	4.7(8)	2.546(7)	

All as prepared samples had a similar quality of fit as seen from the R factor, for this reason the EXAFS and Fourier transformed EXAFS plots for only H/Si0.5_Cu0.06 is shown here, with the plots for the other samples in appendix D. From the FT EXAFS plot in Figure 4-46, there is good agreement between the experimental and theoretical fit curve, for the two shells fitted.

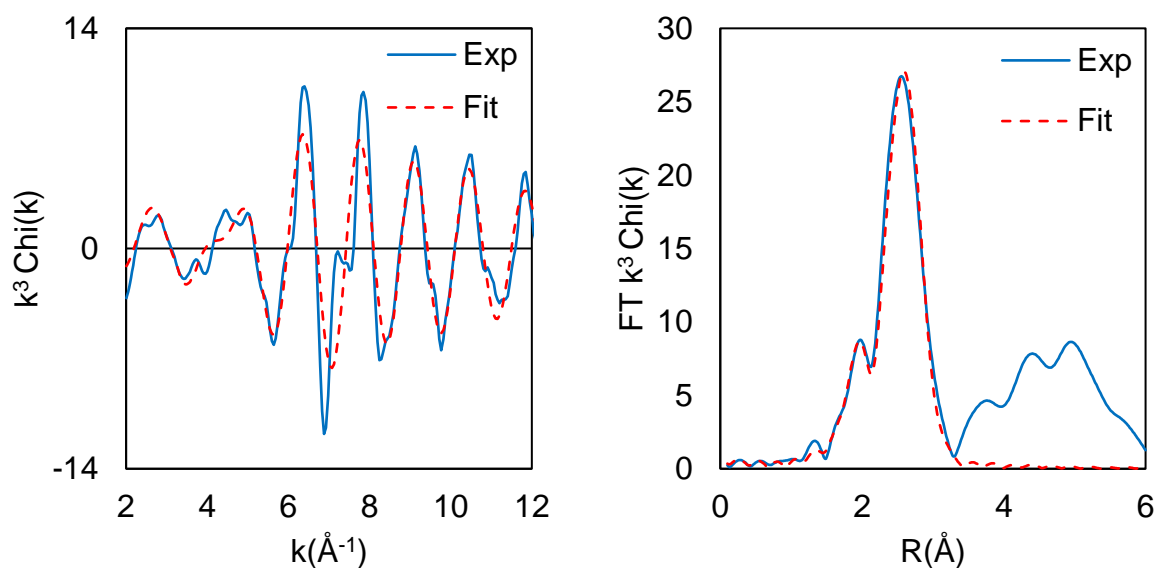


Figure 4-46: The normalised EXAFS (Left) and Fourier transformation of the normalised EXAFS (Right) for H/Si_{0.5}_Cu_{0.06}/AP. The blue line is the experimental data, and the dotted red line is the theoretically fitted curve

4.7.2.2 Calcined and post HC-SCR samples

The result of the EXAFS refinement for calcined and post HC-SCR samples are shown in Table 4-9. For all samples a reasonably good fit was obtained by fitting a single Cu-O shell. There also appears to be only minor changes arising in the sample during HC-SCR in dry feed. For HC-SCR done in wet feed there appears to be a slight change in multiplicity of the Cu-O shell. Since all samples had a similar quality of fit, the EXAFS and FT-EXAFS of H/Si_{0.5}_Cu_{0.06} is shown as example in Figure 4-47, while EXAFS plot of the remaining samples can be found in Appendix D.

Table 4-9: The results of EXAFS refinement for calcined and post HC-SCR samples, with type of shell, fermi energy, Debye Waller factor, shell distance, and R-factor given

Sample name	Shell	E_F [eV]	$2\sigma^2$ [\AA^2]	N	r [\AA]	R[%]
C/Si0.3_Cu0.04	Cu-O	-5.2(6)	0.011(2)	4.2(4)	1.964(7)	35.03
H/Si0.3_Cu0.04	Cu-O	-5.3(6)	0.011(2)	4.0(3)	1.963(6)	33.31
H/Si0.5_Cu0.02	Cu-O	-3.2(6)	0.010(2)	3.8(3)	1.953(6)	32.92
H/Si0.5_Cu0.04	Cu-O	-5.5(6)	0.011(2)	4.1(3)	1.967(6)	34.17
H/Si0.5_Cu0.06	Cu-O	-5.8(6)	0.010(2)	3.2(3)	1.961(6)	35.75
H/Si0.5_Cu0.02/HCd	Cu-O	-3.9(7)	0.009(2)	3.5(3)	1.946(7)	36.40
H/Si0.5_Cu0.04/HCd	Cu-O	-5.3(6)	0.010(2)	3.9(3)	1.957(6)	30.12
H/Si0.5_Cu0.04/HCW	Cu-O	-4.8(7)	0.005(1)	3.2(3)	1.965(5)	31.90
H/Si0.5_Cu0.06/HCd	Cu-O	-4.9(8)	0.007(2)	3.1(3)	1.951(7)	40.19

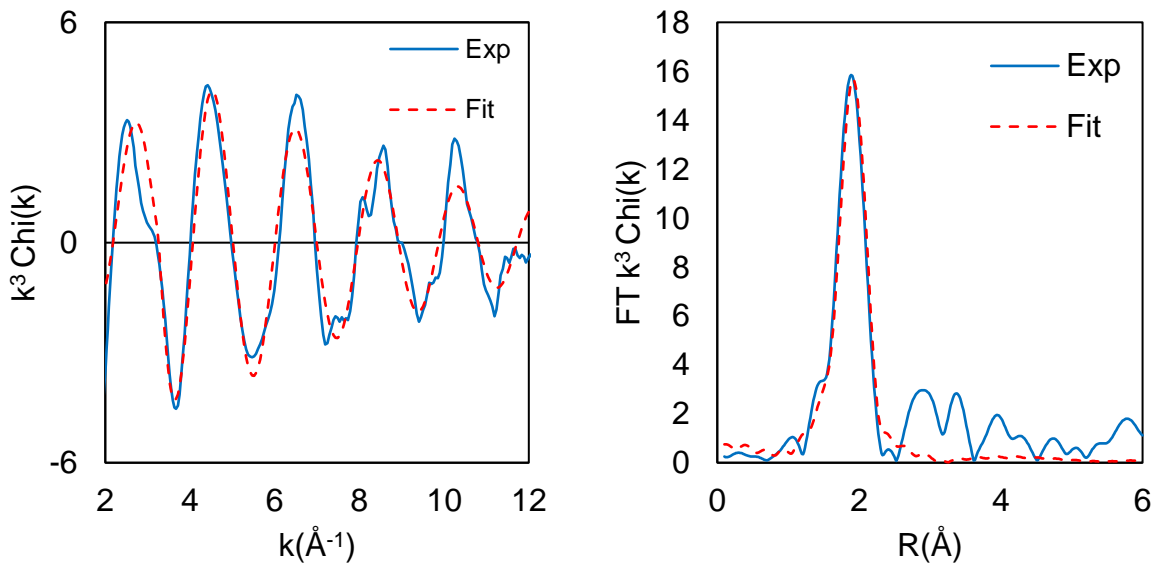


Figure 4-47: The normalised EXAFS (Left) and Fourier transformation of the normalised EXAFS (Right) for H/Si0.5_Cu0.06. The blue line is the experimental data, and the dotted red line is the theoretically fitted curve

4.7.2.3 Fourier filtering

For H/Si_{0.5}Cu_{0.06} Fourier filtering was done to determine the shell that gives rise to the peak between 2.9-3.3Å in the Fourier transformed EXAFS plot. The result of the refinement of the Fourier filtered EXAFS is summarised in Table 4-10. The fit for copper is poor, while the fit for the T-atoms is quite good. This could indicate that some copper is incorporated into the framework.

Table 4-10: The result of the refinement of the Fourier filtered peak of H/Si_{0.5}Cu_{0.06}.

Shell	E _F [eV]	2σ ² [Å ²]	N	r[Å]	R[%]
Cu-Cu	4(1)	0.037(5)	3.6(9)	3.41(1)	48.92
Cu-Al	-13.7(5)	0.008(1)	0.97(7)	3.358(4)	16.17
Cu-P	-18.1(5)	0.008(1)	0.78(6)	3.338(4)	16.79
Cu-Si	-15.8(5)	0.008(1)	0.87(6)	3.347(4)	16.72

4.7.2.4 TPR

For the C/Si_{0.3}Cu_{0.04} temperature programmed reduction (TPR) was performed. This was done to determine the particle size of the metallic copper particles formed and determine whether they are formed in the constrained environment of the SAPO-34 framework. EXAFS measurements were done at maximum temperature (670°C) and refined, with the results of the refinement shown in Table 4-11. The fitted EXAFS and Fourier transformed EXAFS plots are shown in Figure 4-48, with a reasonably good fit.

The work done by De Graaf et.al.⁷¹ makes it possible to calculate particle size from the coordination obtained from EXAFS. A coordination of 10 translates a particle size of 21Å. Since the SAPO-34 cage has the dimensions of 7.5x8.2Å, the metal particles are not formed within the cages. This is evidence of copper species being present outside the SAPO-34 pore network and thereby not being incorporated.

Table 4-11: The result of EXAFS refinement for C/Si0.3_Cu0.04 at 670°C during TPR

Shell	E_F [eV]	$2\sigma^2$ [Å ²]	N	r [Å]	R[%]
Cu-Cu	-5.11(7)	0.045(3)	10(1)	2.504(7)	39.33

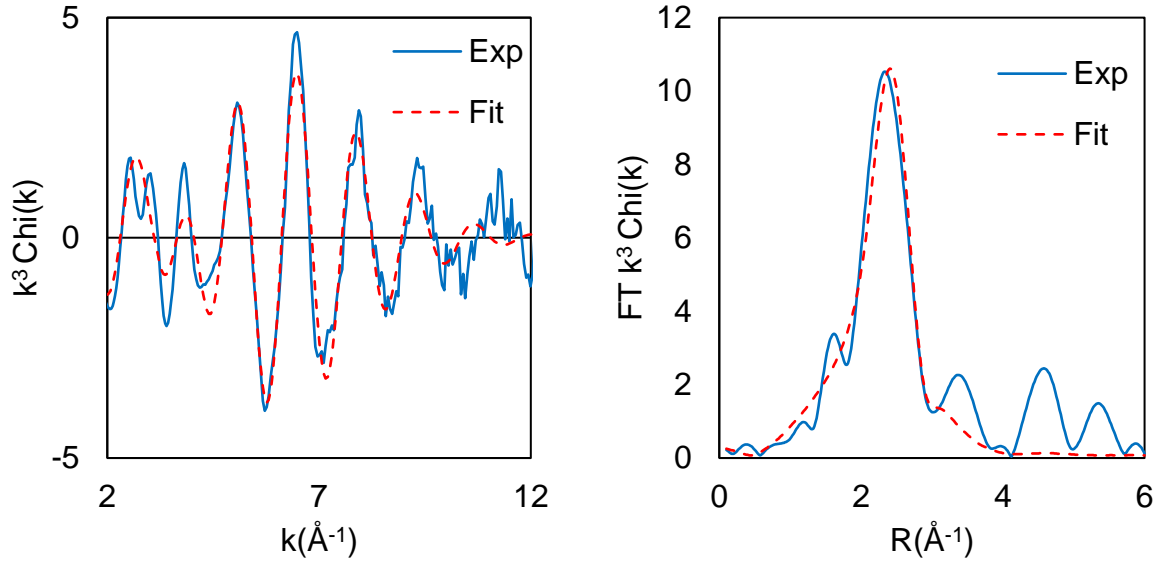


Figure 4-48: The normalised EXAFS (Left) and Fourier transformation of the normalised EXAFS (Right) for C/Si0.3_Cu0.04 at 670°C during TPR. The blue line is the experimental data, and the dotted red line is the theoretically fitted curve

4.8 HC-SCR

HC-SCR was performed in both dry and wet feed, using a FTIR or a NO_x-box as the analyser. The main result obtained from the testing is the conversion of NO_x, which is calculated by the following equation:

$$X_{NO} = \frac{C(NO)_{WBP} - C(NO)_{rx}}{C(NO)_{WBP}} * 100\%$$

with X_{NO} being the percentage of NO converted, $C(NO)_{WBP}$ being the weighted bypass NO concentration, and $C(NO)_{rx}$ being the NO concentration measured over the reactor. The $C(NO)_{WBP}$ was calculated by the following equation:

$$C(NO)_{WBP} = \left(\frac{500-T}{225}\right) * C(NO)_{BP(end)} + \left(\frac{T-275}{225}\right) * C(NO)_{BP(start)}$$

where T is the reaction temperature, $C(NO)_{BP(end)}$ is the concentration of NO measured over bypass at prior to reaction, and $C(NO)_{BP(start)}$ is the concentration of NO measured over bypass after completion of the reaction.

The samples that were tested for HC-SCR, their catalytic activity window, and their maximum conversion temperature are shown in Table 4-12.

Table 4-12: HC-SCR catalytic activity diagram, with M signifying maximum conversion temperature and the coloured squares being temperature where the NO_x conversion was above 30%.

Conversion \geq 30 % and temperature for maximum conversion										
Temperature	275	300	325	350	375	400	425	450	475	500
H/Si0.5Cu0.02										M
H/Si0.5Cu0.04							M			
C/Si0.5Cu0.04										M
H/Si0.5Cu0.06						M				
H/Si0.5Cu0.02(W)				M						
H/Si0.5Cu0.04(W)					M					
C/Si0.5Cu0.04(W)				M						
H/Si0.5Cu0.06(W)				M						
H/Si0.3Cu0.04						M				
C/Si0.3Cu0.04				M						

A comparison of the conversion of C/Si0.5_Cu0.04 and H/Si0.5_Cu0.04 is made in Figure 4-49. In dry feed the conventional sample has a higher conversion across the entire temperature range compared with the hierarchical, with the difference being between 2-25%. The same trend is also seen C/Si0.3_Cu0.04 and H/Si0.3_Cu0.04, with conversion plot found in the Appendix D.

In wet feed the conventional sample still has a better conversion in temperature range 275-325°C, while the hierarchical sample has better conversion between 350-500°C. For both the conventional and the hierarchical sample the conversion was better in dry feed at high temperature, while being better in wet feed at lower temperatures. This trend is more pronounced for the hierarchical sample and is also seen for the other hierarchical samples with different copper amounts.

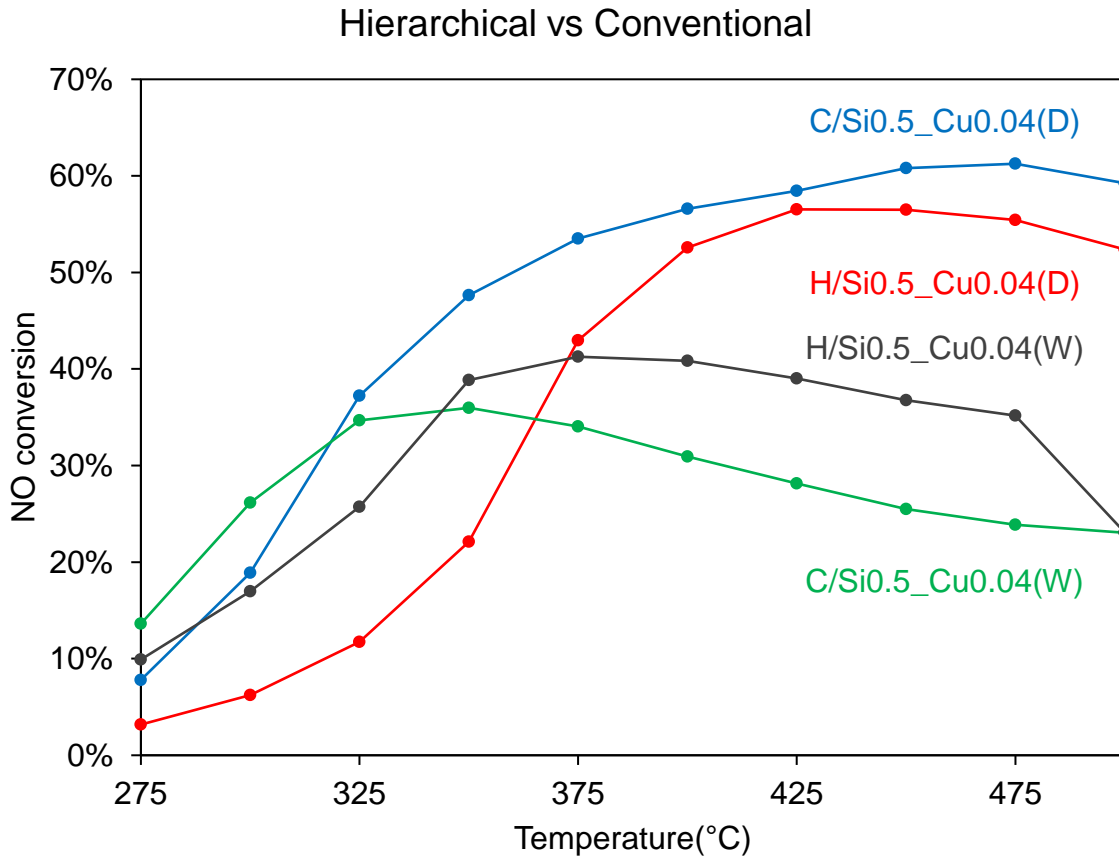


Figure 4-49: Shows the NO conversion, in dry and wet feed, for a hierarchical and conventional sample made with the same synthesis conditions

The copper content in hierarchical samples appear to influence the temperature range the catalyst is active in dry feed, as seen in Figure 4-50. Higher copper content appears to move the activity window to lower temperature, with hardly any change in maximum conversion. The same trend is not seen in wet feed. In wet feed, all samples have a relatively flat conversion

profile, as seen in Figure 4-51, and there is no clear correlation between copper content and conversion.

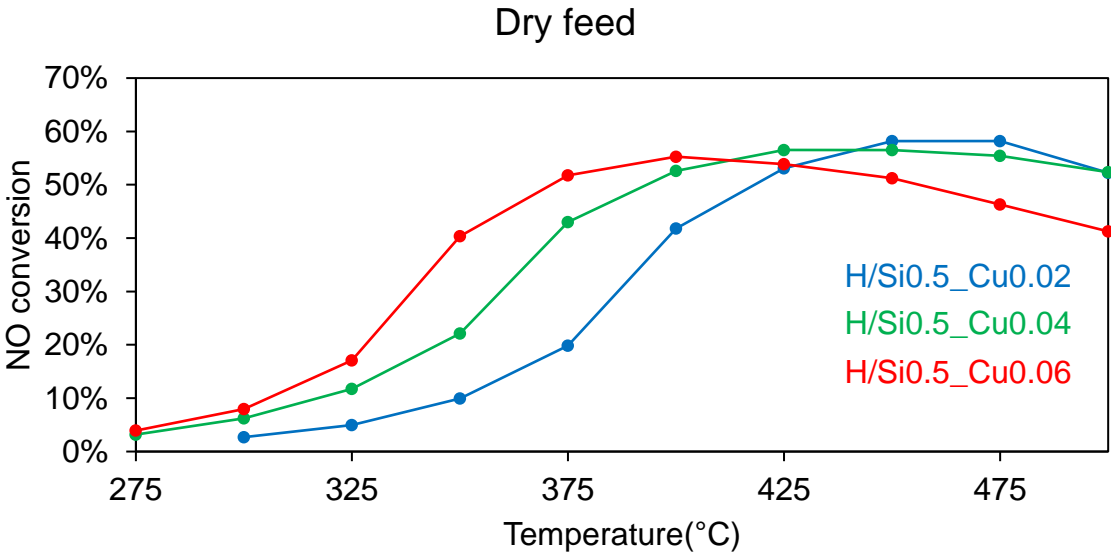


Figure 4-50: NO conversion for hierarchical samples with differing copper amounts in dry feed

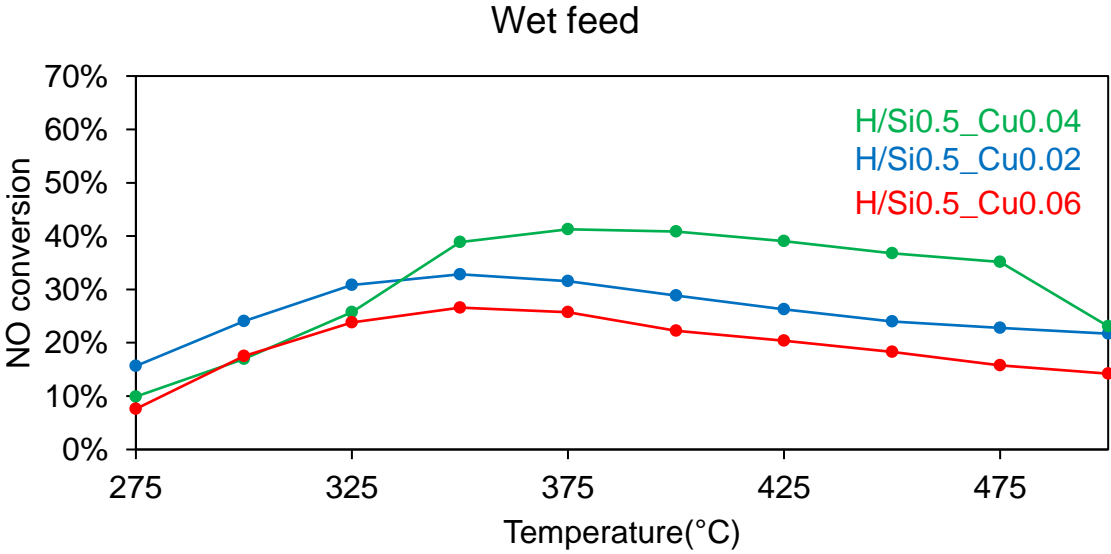


Figure 4-51: NO conversion for hierarchical samples with differing copper amounts in wet feed

5 Discussion

The main goal of this thesis was to synthesise hierarchical SAPO-34 with copper introduced by isomorphous substitution, for use as a HC-SCR catalyst. In addition, the synthesis of hierarchical SAPO-34 without copper was set as a secondary goal.

5.1 Hierarchical SAPO-34 without copper

To achieve the goal of synthesising hierarchical SAPO-34 without copper, various mesoporous structure directing agents (MeSDA) were tested, in combination with variation of other synthesis conditions. Determining whether a synthesis was successful was done by evaluating results obtained from XRD, N₂-physisorption, and SEM. For promising samples, MTH was performed to determine the effect the hierarchical structure had on catalytic properties. The MeSDA that were tested, and the results of characterisation and catalytic testing is summarised in Figure 5-1.

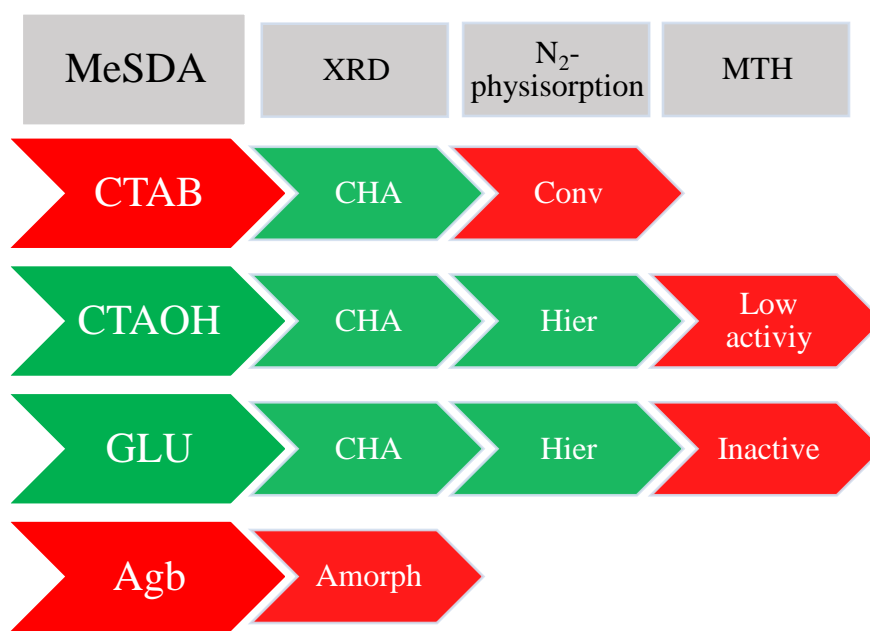


Figure 5-1: The characterisation and MTH results for hierarchical SAPO-34 made with various MeSDA. A MeSDA marked in green signify a successful synthesis of hierarchical SAPO-34, while red signifies an unsuccessful synthesis. Green also indicates desired results from characterisation techniques, with red indicating undesired results.

Based on XRD and N₂-physisorption results, using either CTAOH or glucose as the MeSDA yielded phase pure hierarchical SAPO-34. In the case CTAOH, a crystallisation parameter study had to be done to obtain phase pure SAPO-34. From the parameter study it was determined that three different temperature and time combinations could be used, as signified

by the green cells in Table 5-1. The other crystallisation times either yielded a combination of CHA and AFI or an amorphous product, signified by yellow and red, respectively.

Table 5-1: Results of the crystallisation parameter study, where CTAOH was used as the MeSDA

Time/ temperature	48h	72h	96h	120h
150°C	×	×	×	✓
180°C	✓	×	×	×
200°C	✓	×	×	×

The samples that were characterised as hierarchical, based on N₂-physisorption results, were H/150°C_120h, made with CTAOH, and H/GLU0.05, made with glucose. These samples both had mesopore volumes close to 0.20cm³/g, and comparing this to the H/SAPO-34 synthesised by Kong et.al.¹, where the maximum mesopore volume obtained was 0.178cm³/g, the samples are clearly hierarchical.

For H/150°C_120h the mesopores are disordered without a clearly defined pore size, as was concluded based on the hysteresis being a combination of a H3 and H4, and no peaks being observed in the BJH plot. This is in accordance with what was Sørli⁵³ for H/SAPO-34 synthesised with CTAOH. In H/GLU0.05 there appears to be a combination of ordered and disordered mesopores, which was concluded from the presence of a peak in the BJH plot at approximately 50Å. These results differ from what was reported by Miletto et.al.⁷², where only ordered mesopores with a pore sizes of 17 and 25Å were detected.

Sun et.al.⁷³ synthesised intercrystalline hierarchical SAPO-34, with mesopore volumes as high as 0.26cm³/g and crystallite sizes in the range of 100-500nm. Since H/GLU0.05 had crystallite sizes in the range of 10-30µm, it can be concluded that the mesopores present in H/GLU0.05 are intracrystalline.

SAPO-34 is known to be a good catalyst for the MTH reaction, with initial conversion close to 100% being reported for both conventional and hierarchical SAPO-34⁷⁰. Better catalytic lifetime of hierarchical SAPO-34 compared to conventional SAPO-34 was reported by Sun

et.al.⁷³, with a conversion of close to 100% maintained for 500min for the hierarchical SAPO-34 compared to 100min for the conventional SAPO-34. Although H/GLU0.05 and H/150°C_120h were classified as hierarchical SAPO-34, the catalytic activity and lifetime for the MTH reaction was significantly worse compared to reported values. From MTH catalytic testing, H/GLU0.05 proved to be completely inactive, while H/150°C_120h had a maximum conversion of 21% after 10min and was completely deactivated after 43min.

Since the Bronsted acid sites are the active sites for the MTH reaction, the acid properties of the samples were investigated. Bronsted acid sites were present in both H/GLU0.05 and H/150°C_120h, with shift of the acid sites in H/150°C_120h during CO-adsorption being measured to 276cm⁻¹. This is in accordance with what was reported for conventional SAPO-34 by Bordiga et.al.⁵⁷, where the shift of the acid sites was 270cm⁻¹. It can therefore be concluded that H/150°C_120h has a comparable acid strength to conventional SAPO-34, and the acid properties of H/150°C_120h does not seem to be the reason for the low catalytic performance.

Another factor that could influence the catalytic properties is the crystallite size. Increasing the average crystallite size of SAPO-34 from 0.4µm to 7µm has been shown to reduce the lifetime for the MTH reaction, with the small crystallite SAPO-34 being 10 times less active after 90min on stream⁷⁴. With the crystallite size of H/GLU0.05 being even larger than 7µm, this is a possible explanation for the inactivity of H/GLU0.05. Whether large crystallite size is a possible reason for the poor activity of H/150°C_120h cannot be evaluated due to SEM imaging not being performed for this sample.

A second factor that could contribute to the poor performance, is that the mesopores are connected in a way that does not improve intracrystalline diffusion. From the N₂-physisorption performed for H/GLU0.05 post MTH, all micropore appeared to be clogged while mesopores were left completely unaltered. The clogging of the micropores is a common problem for SAPO-34 during MTH⁷⁵, but the problem appears to be much more severe for H/GLU0.05, since the samples was completely inactive.

5.2 Hierarchical SAPO-34 with copper

The main goal of the thesis was to synthesise hierarchical SAPO-34 with isomorphously incorporated copper, for use in HC-SCR of NO_x. The approach taken was to test a variety of MeSDA and based on results from XRD, N₂-physisorption, ICP-MS, CO-adsorption, MTH, XAS and HC-SCR, determine whether the goal was achieved. A summary of the MeSDA tested and results of the characterisation techniques and catalytic testing is shown in Figure 5-2.

From the initial test of MeSDA, the samples that were classified as being hierarchical and had a total surface area(S_T) above 300m²/g, were H/CTAB0.05_Cu0.02 and H/CTAOH0.05_Cu0.02, using CTAOH and CTAB as the MeSDA, respectively. The mesopores of both samples appear to be disordered and without a clearly defined pore size, as can be inferred from the hysteresis being a combination of H3 and H4 and the lack of any clearly defined peaks in the BJH plots⁵⁰. The pore structure therefore appears to be similar to the hierarchical samples without copper, where the samples were classified as being intracrystalline hierarchical SAPO-34 with disordered mesopores. It can therefore be concluded that H/CTAB0.05_Cu0.02 and H/CTAOH0.05_Cu0.02 do not have the idealised hierarchical structure, where ordered mesopores connected the crystallite surface with micropores in the interior of the crystallite¹⁶. Based on the results from XRD and N₂-physisorption, CTAOH was chosen for further syntheses, and from this point forward the discussion will be related to these samples.

As previously mentioned it was difficult to determine solely from XRD results whether the samples were completely phase pure due to possible presence of metallic copper in as prepared samples and CuO in calcined samples. When comparing this to the XAS results of calcined samples it still not possible to conclude since no Cu-Cu distances were found indicating the presence of Cu⁰ or CuO⁷⁶. For the as prepared samples Cu-Cu distances, at 2.55Å were found with multiplicity ranging from 1.1-4.7 were found, proving that cu is not fully incorporated since Cu metal has distance at 2.55Å⁷⁷. This means that there is probably some CuO present in calcined sample, as was also indicated by peaks in the diffractograms. The findings were true for all Ex-situ samples, which were synthesised using either MOR or MOR+CTAOH. It is therefore likely that MOR autoreduces copper during crystallisation, as has been reported to be the case for amines³⁹.

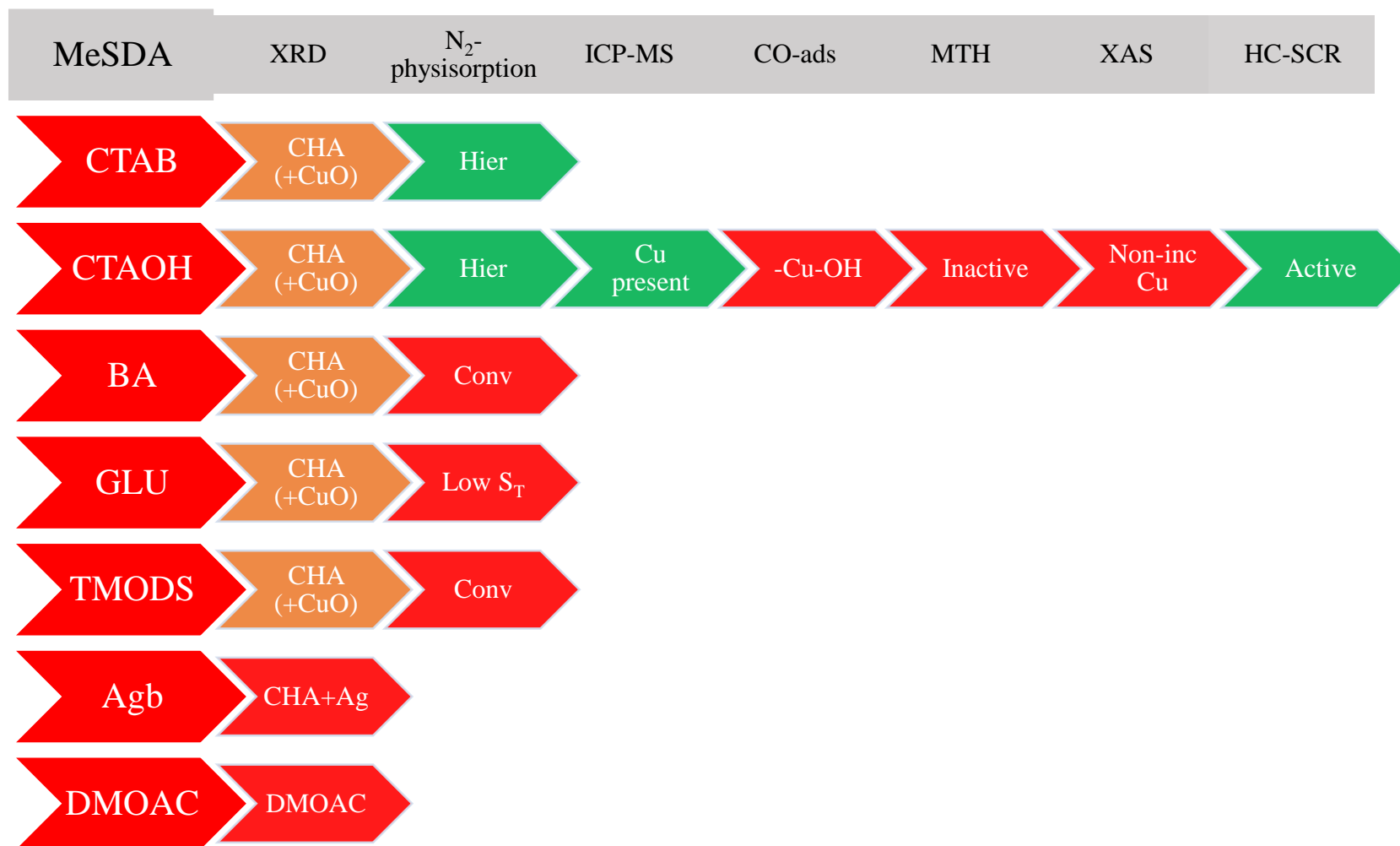


Figure 5-2: Summary of the characterisation and HC-SCR results for hierarchical SAPO-34 with copper, made with various MeSDA. A MeSDA marked in green signify a successful synthesis of hierarchical SAPO-34 with incorporated copper, while red signifies an unsuccessful synthesis. For the characterisation techniques and catalytic testing, green signifies desired results, orange signifies inconclusive results and red signifies undesired results

The result of linear combination fitting and the E_0 values of as prepared samples indicate the presence of both metallic copper and Cu^{2+} . The fact that a poor fit was obtained for linear combination fitting of XANES for calcined samples, using Cu-foil, Cu_2O , CuO and Cu-tutton as the references, is evidence of a different coordinated Cu^{2+} -species being present. Taking this into account and the good fit obtained for a second T-atom shell through by Fourier filtering, some fraction of the copper could have been incorporated.

However, the copper was not entirely reduced, as seen from Cu-O distances found at approximately 1.9\AA in as prepared samples, this could in part be attributed to Cu^{2+} being partially incorporated into the framework of SAPO-34. The reason for this might be come from using TEPA as a co-complexing agent for Cu^{2+} , which has been done by Martinez-Franco et.al. were TEPA was found to aid incorporation of Cu^{2+} in conventional SAPO-34. Determining whether CTAOH also autoreduces copper is difficult, due to MOR being used in all synthesis. It could be interesting to investigate other MiSDA in combination with TEPA and CTAOH.

On the other hand, a part of the goal was making samples active for HC-SCR. The above-mentioned C/CuSAPO-34(D) and H/CuSAPO-34(D) were shown to be active, with the best conversion in for C/CuSAPO-34 being 73% at 375°C and the best conversion for H/CuSAPO-34 was 62% at 400°C . The selectivity towards N_2 cannot be determined due to HC-SCR being performed with a FTIR analyser, that can only detect IR active gases. The Maximum conversion for copper containing SAPO-34 has been reported by Jakobsen¹⁵ to be above 80% at 500°C , which is higher compared to the conversions shown above for C/CuSAPO-34 and H/CuSAPO-34.

The lower conversion of C/CuSAPO-34 and H/CuSAPO-34 could be due to the presence of CuO, which is known to be inactive for HC-SCR⁷⁸. For the temperature programmed reduction of C/Si_{0.3}Cu_{0.04}, the particle size of metallic copper was calculated to be 21\AA , which is larger than what the SAPO-34 cage can accommodate. This means that at least some of the copper is not contained in the micropores and could indicate presence of Cu-species e.g. CuO at external crystallite surfaces, that sinter during reduction.

The lower HC-SCR catalytic activity could also be due to all C/CuSAPO-34 and H/CuSAPO-34 having surface areas, given in Table 5-2, lower than $550\text{m}^2/\text{g}$, which is the benchmark value for SAPO-34. It has previously been reported by Zuo et.al.¹¹ that lower surface areas of SAPO-34 leads to lower NO conversion in HC-SCR. Comparing the surface area of C/CuSAPO-34

and H/CuSAPO-34 and max NO conversion, also shown in Table 5-2, there appears to be some correlation, however C/Si0.5_Cu0.04 which has the highest surface area does not have the highest conversion. This indicates that other factors, such as the incomplete incorporation of copper resulting in CuO species, also has an effect. Determining the effect mesopores in H/CuSAPO-34 had on the HC-SCR reaction is difficult due to variations in surface area, and possible variations in amounts of non-incorporated copper. However, from comparing the mesopore volume with max conversion, shown in Table 5-2, it appears that the presence of mesopores in these samples have no solely positive effect, whereas the sample with highest mesopore volume at 0.14cm³/g gives one of the lowest conversions in this study.

Table 5-2: Shows copper content, surface area, mesopore volume, and max NO conversion for C/CuSAPO-34 and H/CuSAPO-34 tested for HC-SCR

Sample	Cu/Al (ICP-MS)	Surface area (m ² /g)	Mesopore volume (cm ³ /g)	Max NO conversion
C/Si0.3_Cu0.04	0.099	452	0.011	73%
C/Si0.5_Cu0.04	0.103	486	0.002	61%
H/Si0.3_Cu0.04	0.134	402	0.112	62%
H/Si0.5_Cu0.02	0.090	352	0.14	58%
H/Si0.5_Cu0.04	0.117	337	0.064	57%
H/Si0.5_Cu0.06	0.296	281	0.083	55%

In addition to catalytic testing for HC-SCR, catalytic testing for MTH was done for H/Si0.3_Cu0.04 and C/Si0.3_Cu0.04. The result for both samples were poor, with the H/CuSAPO-34 sample being completely inactive and the conventional sample having a conversion of 16% after 10min on stream and was subsequently deactivated. The conversion and lifetime is significantly worse compared to what has been reported for C/SAPO-34, H/SAPO-34 and C/CuSAPO-34^{70, 79}, where initial conversion has been as high as 100% and conversion above 50% has been maintained for as long as 3 hours. These results are reminiscent of the results obtained for H/SAPO-34, where the possible explanations for the poor performance given were large crystallites and non-beneficial mesopore connectivity.

In addition, bands were assigned to CO interacting with Cu^{2+} and Cu^+ species. The presence of Cu^+ species was not expected, since all copper should be Cu^{2+} if incorporation was successful. An explanation of this could be that Cu^{2+} was reduced during the dehydration, prior to CO-adsorption. Since H/Si0.3_Cu0.04 had acidic properties comparable to C/Si0.3_Cu0.04, the samples should be active for MTH. The fact that it is not active, points towards crystallite size or mesopore connectivity being the reason for the poor catalytic performance.

As for H/GLU0.05, the unaltered non-micropore volume after the MTH reaction indicate that the mesopores in H/Si0.3_Cu0.04 are connected to the crystallite surface to a certain extent. However, since the activity of H/CuSAPO-34 has been shown to be worse compared to C/CuSAPO-34, for both MTH and HC-SCR, it appears that the mesopores are connected in a way that is not beneficial for catalysis.

Finally, the presence of non-incorporated copper for H/CuSAPO-34 and C/CuSAPO-34 indicates that there is a problem with the general synthesis procedure. Since it has previously been reported that amines can lead to formation of metallic copper during hydrothermal synthesis of SAPO-5 and SAPO-11³⁹, it is reasonable to suggest that metallic copper is formed due to morpholine, which was used as the MeSDA for all H/CuSAPO-34 and C/CuSAPO-34 syntheses. It is therefore difficult to draw any conclusion regarding the applicableness of the MeSDA tested.

6 Conclusion

To summarise, the goal of synthesising hierarchical SAPO-34 was achieved by using glucose and CTAOH as the MeSDA. The successful syntheses yielded intracrystalline hierarchical SAPO-34, where the mesopores are disordered and without a clearly defined pore size. The mesopores did however appear to be connected to the crystallite surface to a certain extent, which is the entire premise behind introducing mesopores. The catalytic properties for the MTH reaction was poor for the H/SAPO-34 samples made with glucose and CTAOH, which could be due to large crystallite sizes, non-beneficial connectivity of mesopores, or a combination of the two factors.

The main goal of synthesising H/CuSAPO-34 with copper isomorphously substituted, for use in the HC-SCR was however not achieved. All H/CuSAPO-34 syntheses conducted were shown to contain non-incorporated copper, as determined from XAS results, and the copper was therefore at best, partially incorporated. Despite this, samples made with CTAB or CTAOH appeared to have intracrystalline mesopores which to a certain extent connected to the

crystallite surface. The catalytic performance of H/CuSAPO-34 samples made with CTAOH for HC-SCR and MTH, was worse compared to the C/CuSAPO-34 samples. In the case of HC-SCR, the activity was also worse than what has been reported previously for copper containing conventional and hierarchical SAPO-34. For MTH, the H/CuSAPO-34 samples were completely inactive, which was found to be due to abnormally rapid deactivation from clogging of micropores.

7 Further work

For further work, the main priority should be to try to devise a synthesis that successfully incorporates copper into hierarchical SAPO-34, without the formation of any non-incorporated copper species.

As stated, the morpholine appears to be the reason metallic copper was formed during syntheses, and to solve this problem two approaches exist. Either the morpholine should be replaced by another MiSDA, or variation of other syntheses parameters should be tested.

C/CuSAPO-34/corderite was successfully synthesised by Wang et.al.⁴⁰ using morpholine as the MiSDA, and this synthesis procedure could be a good starting point if morpholine is to be used. Using TEAOH is another option, since TEAOH is an ammonium cation and should hopefully not lead to metallic copper forming.

Testing of additional MeSDA should also be performed, since all hierarchical SAPO-34 synthesised, with or without copper, appear to have mesopores which are disordered and without a clearly defined pore size. The ideal MeSDA would be one that generates ordered mesopores, with a clearly defined pore size, which connect the crystallite surface and the internal micropores.

Further characterisation of the H/CuSAPO-34 and C/CuSAPO-34 samples should not be prioritised due copper not being incorporated. However, SEM imaging of C/Si0.5_Cu0.04 could be done to have a more rigorous comparison of particles size difference between H/CuSAPO-34 and C/CuSAPO-34.

When it comes to the H/SAPO-34 samples, SEM analysis should be performed for H/150°C_120h to be able to compare crystallite size with H/GLU0.05, and thereby understand the difference in MTH performance. For both H/150°C_120h and H/GLU0.05 further characterisation of the mesopore connectivity should be done. This could be done by performing FTIR measurements, while using a probe molecule larger than CO, such as collidine⁸⁰, which only can access the mesopores. Collidine will only be able to perturb Bronsted acid sites situated at the end of the micropores connected to the MeSDA, and thereby you can assess the amount of acid sites accessible from the mesopores.

8 References

1. Kong, L.; Jiang, Z.; Zhao, J.; Liu, J.; Shen, B., The Synthesis of Hierarchical SAPO-34 and its Enhanced Catalytic Performance in Chloromethane Conversion to Light Olefins. *Catalysis Letters* **2014**, *144* (9), 1609-1616.
2. Guidance document on control techniques for emissions of sulphur, nitrogen oxides, volatile organic compounds and particulate matter (including PM₁₀, PM_{2.5} and black carbon) from stationary sources*. Long-range, E. B. f. t. C. o.; Pollution, T. A., Eds. Economic Commission for Europe: 2015.
3. National emissions reported to the Convention on Long-range Transboundary Air Pollution (LRTAP Convention). <https://www.eea.europa.eu/data-and-maps/data/national-emissions-reported-to-the-convention-on-long-range-transboundary-air-pollution-lrtap-convention-11#tab-data-visualisations> (accessed 14.03.18).
4. Chaloulakou, A.; Mavroidis, I.; Gavriil, I., Compliance with the annual NO₂ air quality standard in Athens. Required NO_x levels and expected health implications. *Atmospheric Environment* **2008**, *42* (3), 454-465.
5. Skalska, K.; Miller, J. S.; Ledakowicz, S., Trends in NO_x abatement: A review. *Sci. Total Environ.* **2010**, *408* (19), 3976-3989.
6. Greenhouse gas emission statistics - emission inventories. http://ec.europa.eu/eurostat/statistics-explained/index.php/Greenhouse_gas_emission_statistics_-_emission_inventories (accessed 18.03.2018).
7. Russo, M. A.; Leitão, J.; Gama, C.; Ferreira, J.; Monteiro, A., Shipping emissions over Europe: A state-of-the-art and comparative analysis. *Atmospheric Environment* **2018**, *177*, 187-194.
8. Thompson, D.; Brown, T. D.; Beér, J. M., NO_x formation in combustion. *Combustion and Flame* **1972**, *19* (1), 69-79.
9. Joumard, R.; Jost, P.; Hickman, J.; Hassel, D., Hot passenger car emissions modelling as a function of instantaneous speed and acceleration. *Sci. Total Environ.* **1995**, *169* (1), 167-174.
10. Castagnola, M.; Caserta, J.; Chatterjee, S.; Chen, H.-Y.; Conway, R.; Fedeyko, J.; Klink, W.; Markatou, P.; Shah, S.; Walker, A., Engine Performance of Cu- and Fe-Based SCR Emission Control Systems for Heavy Duty Diesel Applications. SAE International: 2011.
11. Zuo, Y.; Han, L.; Bao, W.; Chang, L.; Wang, J., Effect of CuSAPO-34 catalyst preparation method on NO_x removal from diesel vehicle exhausts. *Chin. J. Catal.* **2013**, *34* (6), 1112-1122.
12. Sato, S.; Yu-u, Y.; Yahiro, H.; Mizuno, N.; Iwamoto, M., Cu-ZSM-5 zeolite as highly active catalyst for removal of nitrogen monoxide from emission of diesel engines. *Applied Catalysis* **1991**, *70* (1), L1-L5.
13. Ishihara, T.; Kagawa, M.; Hadama, F.; Takita, Y., Copper Ion-Exchanged SAPO-34 as a Thermostable Catalyst for Selective Reduction of NO with C₃H₆. *Journal of Catalysis* **1997**, *169* (1), 93-102.

14. Nishiguchi, H.; Kimura, S.; Ishihara, T.; Takita, Y., Selective reduction of NOX with C3H6 over CU incorporated into silicoaluminophosphate (SAPO). *Research on Chemical Intermediates* **1998**, *24* (4), 391-399.
15. Jakobsen, T. Investigation of hierarchical pore characteristics and interactions with copper for catalytic applications. NTNU, Trondheim, 2014.
16. Pérez-Ramírez, J.; Christensen, C. H.; Egeblad, K.; Christensen, C. H.; Groen, J. C., Hierarchical zeolites: Enhanced utilisation of microporous crystals in catalysis by advances in materials design. *Chem. Soc. Rev.* **2008**, *37* (11), 2530-2542.
17. I.Chorkendorff, J. W. N., *Concepts of Modern Catalysis and Kinetics*. Wiley-VCH: Weinheim, 2007.
18. Database of Zeolite Structures. <http://www.iza-structure.org/databases/> (accessed 06.04.18).
19. Moliner, M.; Martínez, C.; Corma, A., Synthesis Strategies for Preparing Useful Small Pore Zeolites and Zeotypes for Gas Separations and Catalysis. *Chemistry of Materials* **2014**, *26* (1), 246-258.
20. Hartmann, M.; Kevan, L., Transition-Metal Ions in Aluminophosphate and Silicoaluminophosphate Molecular Sieves: Location, Interaction with Adsorbates and Catalytic Properties. *Chem. Rev. (Washington, D. C.)* **1999**, *99* (3), 635-663.
21. Momma, K.; Izumi, F., VESTA 3 for three-dimensional visualization of crystal, volumetric and morphology data. *Journal of Applied Crystallography* **2011**, *44* (6).
22. Lok, B. M.; Messina, C. A.; Patton, R. L.; Gajek, R. T.; Cannan, T. R.; Flanigen, E. M., Silicoaluminophosphate molecular sieves: another new class of microporous crystalline inorganic solids. *Journal of the American Chemical Society* **1984**, *106* (20), 6092-6093.
23. Prakash, A. M.; Unnikrishnan, S., Synthesis of SAPO-34: high silicon incorporation in the presence of morpholine as template. *Journal of the Chemical Society, Faraday Transactions* **1994**, *90* (15), 2291-2296.
24. Qiao, Z. A.; Huo, Q. S., Chapter 15 - Synthetic Chemistry of the Inorganic Ordered Porous Materials. In *Modern Inorganic Synthetic Chemistry (Second Edition)*, Elsevier: Amsterdam, 2017; pp 389-428.
25. Sun, Q.; Xie, Z.; Yu, J., The state-of-the-art synthetic strategies for SAPO-34 zeolite catalysts in methanol-to-olefin conversion. *National Science Review* **2017**, nwx103-nwx103.
26. Wilson, S.; Barger, P., The characteristics of SAPO-34 which influence the conversion of methanol to light olefins. *Microporous and Mesoporous Materials* **1999**, *29* (1), 117-126.
27. Li, J.; Wei, Y.; Liu, G.; Qi, Y.; Tian, P.; Li, B.; He, Y.; Liu, Z., Comparative study of MTO conversion over SAPO-34, H-ZSM-5 and H-ZSM-22: Correlating catalytic performance and reaction mechanism to zeolite topology. *Catalysis Today* **2011**, *171* (1), 221-228.
28. Rostami, R.; Ghavipour, M.; Di, Z.; Wang, Y.; Behbahani, R., *Study of coke deposition phenomena on the SAPO_34 catalyst and its effects on light olefin selectivity during the methanol to olefin reaction*. 2015; Vol. 5, p 81965-81980.
29. Yang, H.; Liu, Z.; Gao, H.; Xie, Z., Synthesis and catalytic performances of hierarchical SAPO-34 monolith. *Journal of Materials Chemistry* **2010**, *20* (16), 3227-3231.
30. Feliczak-Guzik, A., Hierarchical zeolites: Synthesis and catalytic properties. *Microporous and Mesoporous Materials* **2018**, *259*, 33-45.

31. Kärger, J.; Freude, D., Mass Transfer in Micro- and Mesoporous Materials. *Chemical Engineering & Technology* **2002**, *25* (8), 769-778.
32. Yang, X.; Lu, T.; Chen, C.; Zhou, L.; Wang, F.; Su, Y.; Xu, J., Synthesis of hierarchical AlPO-n molecular sieves templated by saccharides. *Microporous and Mesoporous Materials* **2011**, *144* (1), 176-182.
33. Schmidt, I.; Boisen, A.; Gustavsson, E.; Ståhl, K.; Pehrson, S.; Dahl, S.; Carlsson, A.; Jacobsen, C. J. H., Carbon Nanotube Templated Growth of Mesoporous Zeolite Single Crystals. *Chemistry of Materials* **2001**, *13* (12), 4416-4418.
34. Gao, F.; Walter, E. D.; Washton, N. M.; Szanyi, J.; Peden, C. H. F., Synthesis and Evaluation of Cu-SAPO-34 Catalysts for Ammonia Selective Catalytic Reduction. 1. Aqueous Solution Ion Exchange. *ACS Catalysis* **2013**, *3* (9), 2083-2093.
35. Frache, A.; Palella, B. I.; Cadoni, M.; Pirone, R.; Pastore, H. O.; Marchese, L., CuAPSO-34 Catalysts for N₂O Decomposition in the Presence of H₂O. A Study of Zeolitic Structure Stability in Comparison to Cu-SAPO-34 and Cu-ZSM-5. *Topics in Catalysis* **2003**, *22* (1), 53-57.
36. Gao, F.; Walter, E. D.; Washton, N. M.; Szanyi, J.; Peden, C. H. F., Synthesis and evaluation of Cu/SAPO-34 catalysts for NH₃-SCR 2: Solid-state ion exchange and one-pot synthesis. *Applied Catalysis B: Environmental* **2015**, *162*, 501-514.
37. Atkins.; Overton; Rourke; Weller; Armstrong, *Inorganic Chemistry*. Fifth edition ed.; Oxford: 2009.
38. Mathisen, K. X-ray absorption spectroscopic studies on active metal sites in zeotypes during the selective catalytic reduction of NO_x with propene in an oxygen rich atmosphere. Doctoral thesis, NTNU, Trondheim, Norway, 2005.
39. Moen, A.; Nicholson, D. G., Reduction of copper(II) with subsequent disproportionation of copper(I) during the hydrothermal syntheses of microporous silicoaluminium phosphates sapo-5 and -11. *Journal of the Chemical Society, Faraday Transactions* **1995**, *91* (19), 3529-3535.
40. Wang, J.-c.; Chen, Y.; Tang, L.; Bao, W.-r.; Chang, L.-p.; Han, L.-n., One-step hydrothermal synthesis of Cu-SAPO-34/cordierite and its catalytic performance on NO_x removal from diesel vehicles. *Transactions of Nonferrous Metals Society of China* **2013**, *23* (11), 3330-3336.
41. Martínez-Franco, R.; Moliner, M.; Franch, C.; Kustov, A.; Corma, A., Rational direct synthesis methodology of very active and hydrothermally stable Cu-SAPO-34 molecular sieves for the SCR of NO_x. *Applied Catalysis B: Environmental* **2012**, *127*, 273-280.
42. Gutberlet, D. H.; Schallert, D. B., Selective catalytic reduction of nox from coal fired power plants. *Catalysis Today* **1993**, *16* (2), 207-235.
43. Wang, D.; Zhang, L.; Li, J.; Kamasamudram, K.; Epling, W. S., NH₃-SCR over Cu/SAPO-34 – Zeolite acidity and Cu structure changes as a function of Cu loading. *Catalysis Today* **2014**, *231*, 64-74.
44. Yahiro, H.; Iwamoto, M., Copper ion-exchanged zeolite catalysts in deNO_x reaction. *Applied Catalysis A: General* **2001**, *222* (1), 163-181.
45. Granger, P.; Parvulescu, V. I., Catalytic NO_x Abatement Systems for Mobile Sources: From Three-Way to Lean Burn after-Treatment Technologies. *Chemical Reviews* **2011**, *111* (5), 3155-3207.

46. Iwamoto, M.; Yahiro, H.; Shundo, S.; Yu-u, Y.; Mizuno, N., Influence of sulfur dioxide on catalytic removal of nitric oxide over copper ion-exchanged ZSM-5 zeolite. *Applied Catalysis* **1991**, *69* (1), L15-L19.
47. Yan, J. Y.; Lei, G. D.; Sachtler, W. M. H.; Kung, H. H., Deactivation of Cu/ZSM-5 Catalysts for Lean NO_x Reduction: Characterization of Changes of Cu State and Zeolite Support. *Journal of Catalysis* **1996**, *161* (1), 43-54.
48. Grinsted, R. A.; Jen, H. W.; Montreuil, C. N.; Rokosz, M. J.; Shelef, M., The relation between deactivation of CuZSM-5 in the selective reduction of NO and dealumination of the zeolite. *Zeolites* **1993**, *13* (8), 602-606.
49. Sardela, M. R., X-Ray Diffraction and Reflectivity. In *Practical Materials Characterization*, Sardela, M., Ed. Springer New York: New York, NY, 2014; pp 1-41.
50. Sing, K. S. W.; Everett, D. H.; Haul, R. A. W.; Moscou, L.; Pierotti, R. A.; Rouquerol, J.; Siemieniewska, T., Reporting Physisorption Data for Gas/Solid Systems with Special Reference to the Determination of Surface Area and Porosity. *Pure Appl. Chem.* **1985**, *57* (4), 603-619.
51. Sing, K. S. W.; Rouquerol, F.; Rouquerol, J.; Llewellyn, P., 8 - Assessment of Mesoporosity. In *Adsorption by Powders and Porous Solids (Second Edition)*, Academic Press: Oxford, 2014; pp 269-302.
52. Lowell, S.; Shields, J. E.; Thomas, M. A.; Thommes, M., Micropore Analysis. In *Characterization of Porous Solids and Powders: Surface Area, Pore Size and Density*, Lowell, S.; Shields, J. E.; Thomas, M. A.; Thommes, M., Eds. Springer Netherlands: Dordrecht, 2004; pp 129-156.
53. Sørli, G. Effect of Porosity on the Hydrothermal Stability of CuSAPO-34 for the deNO_x process. Master, NTNU, Trondheim, Norway, 2016.
54. Joy, D. C., Scanning Electron Microscopy. In *Materials Science and Technology*.
55. Emrani, P.; Fatemi, S.; Ashraf Talesh, S. S., *Effect of Synthesis Parameters on Phase Purity, Crystallinity and Particle Size of SAPO-34*. 2011; Vol. 30.
56. Karge, H. G., Characterization by infrared spectroscopy. *Microporous and Mesoporous Materials* **1998**, *22* (4), 547-549.
57. Bordiga, S.; Regli, L.; Cocina, D.; Lamberti, C.; Bjørgen, M.; Lillerud, K. P., Assessing the Acidity of High Silica Chabazite H-SSZ-13 by FTIR Using CO as Molecular Probe: Comparison with H-SAPO-34. *The Journal of Physical Chemistry B* **2005**, *109* (7), 2779-2784.
58. Cortés-Reyes, M.; Finocchio, E.; Herrera, C.; Larrubia, M. A.; Alemany, L. J.; Busca, G., A study of Cu-SAPO-34 catalysts for SCR of NO_x by ammonia. *Microporous and Mesoporous Materials* **2017**, *241*, 258-265.
59. Newville, M., *Fundamentals of XAFS*. 2004; Vol. 78.
60. What is a Synchrotron? <http://www.esrf.eu/about/synchrotron-science/synchrotron> (accessed 07.03.2018).
61. What is a Beamline? <http://www.esrf.eu/about/synchrotron-science/beamline> (accessed 15.03.2018).
62. Baker, M. L.; Mara, M. W.; Yan, J. J.; Hodgson, K. O.; Hedman, B.; Solomon, E. I., K- and L-edge X-ray absorption spectroscopy (XAS) and resonant inelastic X-ray scattering (RIXS) determination of differential orbital covalency (DOC) of transition metal sites. *Coordination Chemistry Reviews* **2017**, *345*, 182-208.

63. Calvin, S., *XAFS for Everyone*. Taylor & Francis: 2013.
64. Fay, M. J.; Proctor, A.; Hoffmann, D. P.; Hercules, D. M., Unraveling EXAFS spectroscopy. *Analytical Chemistry* **1988**, *60* (21), 1225A-1243A.
65. Ravel, B.; Newville, M., ATHENA, ARTEMIS, HEPHAESTUS: data analysis for X-ray absorption spectroscopy using IFEFFIT. *Journal of Synchrotron Radiation* **2005**, *12* (4), 537-541.
66. Tomic, S.; Searle, B. G.; Wander, A.; Harrison, N. M.; Dent, A. J.; Mosselmans, J. F. W.; Inglesfield, J. E., New Tool for the Analysis of EXAFS: The DL_EXCURV Package. **2004**.
67. Ali, D. Pore Characteristics and Acid Properties of Hierarchical SAPO-34. NTNU, 2015.
68. Wang, L.; Li, W.; Qi, G.; Weng, D., Location and nature of Cu species in Cu/SAPO-34 for selective catalytic reduction of NO with NH₃. *Journal of Catalysis* **2012**, *289*, 21-29.
69. Szanyi, J.; Kwak, J. H.; Zhu, H.; Peden, C. H. F., Characterization of Cu-SSZ-13 NH₃ SCR catalysts: an in situ FTIR study. *Physical Chemistry Chemical Physics* **2013**, *15* (7), 2368-2380.
70. Wu, L.; Hensen, E. J. M., Comparison of mesoporous SSZ-13 and SAPO-34 zeolite catalysts for the methanol-to-olefins reaction. *Catalysis Today* **2014**, *235*, 160-168.
71. de Graaf, J.; van Dillen, A. J.; de Jong, K. P.; Koningsberger, D. C., Preparation of Highly Dispersed Pt Particles in Zeolite Y with a Narrow Particle Size Distribution: Characterization by Hydrogen Chemisorption, TEM, EXAFS Spectroscopy, and Particle Modeling. *Journal of Catalysis* **2001**, *203* (2), 307-321.
72. Miletto, I.; Ivaldi, C.; Paul, G.; Chapman, S.; Marchese, L.; Raja, R.; Gianotti, E., Hierarchical SAPO-34 Architectures with Tailored Acid Sites using Sustainable Sugar Templates. *ChemistryOpen* **2018**, *7* (4), 297-301.
73. Sun, Q.; Wang, N.; Xi, D.; Yang, M.; Yu, J., Organosilane surfactant-directed synthesis of hierarchical porous SAPO-34 catalysts with excellent MTO performance. *Chem. Commun.* **2014**, *50* (49), 6502-6505.
74. Lee, K. Y.; Chae, H.-J.; Jeong, S.-Y.; Seo, G., Effect of crystallite size of SAPO-34 catalysts on their induction period and deactivation in methanol-to-olefin reactions. *Applied Catalysis A: General* **2009**, *369* (1), 60-66.
75. Qi, G.; Xie, Z.; Yang, W.; Zhong, S.; Liu, H.; Zhang, C.; Chen, Q., Behaviors of coke deposition on SAPO-34 catalyst during methanol conversion to light olefins. *Fuel Processing Technology* **2007**, *88* (5), 437-441.
76. Ghijsen, J.; Tjeng, L. H.; van Elp, J.; Eskes, H.; Westerink, J.; Sawatzky, G. A.; Czyzyk, M. T., Electronic structure of $\{\text{Cu}\}_2\text{O}$ and CuO. *Physical Review B* **1988**, *38* (16), 11322-11330.
77. Kristiansen, T. Aerogels; A new class of materials for catalytic purposes. NTNU, Trondheim, Norway, 2013.
78. Kim, M. H.; Nam, I.-S., New opportunity for HC-SCR technology to control NO_x emission from advanced internal combustion engines. In *Catalysis: Volume 18*, Spivey, J. J., Ed. The Royal Society of Chemistry: 2005; Vol. 18, pp 116-185.
79. Salih, H. A.; Muraza, O.; Abussaud, B.; Al-Shammari, T. K.; Yokoi, T., Catalytic enhancement of SAPO-34 for methanol conversion to light olefins using in-situ metal incorporation. *Industrial & Engineering Chemistry Research* **2018**.

80. Holm, M. S.; Svelle, S.; Joensen, F.; Beato, P.; Christensen, C. H.; Bordiga, S.; Bjørgen, M., Assessing the acid properties of desilicated ZSM-5 by FTIR using CO and 2,4,6-trimethylpyridine (collidine) as molecular probes. *Applied Catalysis A: General* **2009**, *356* (1), 23-30.

Appendix A: Synthesis

Table A-1: Amounts added of chemicals for the syntheses of C/SAPO-34 and H/SAPO-34.

	Amount added						
	Al	P	Si	TEA	TEAOH	H ₂ O	MeSDA
C/Si0.26	6.86g	9.44g	3.70g	8.30g	3.05g	39g	-
H/CTAB0.01	4.90g	7.72g	4.05g	6.82g	3.90g	35g	0.25mL(CTAB)
H/CTAOH0.004	4.90g	7.72g	4.05g	6.82g	3.90g	39g	3.20mL(CTAOH)
H/CTAOH0.008	4.90g	7.72g	4.05g	6.82g	3.90g	39g	6.41mL(CTAOH)
H/CTAPH0.0013	4.90g	7.72g	4.05g	6.82g	3.90g	39g	9.61mL(CTAOH)
H/x°C_yh*	4.90g	7.96g	3.11g	6.98g	2.54g	31.5g	2.70mL(CTAOH)

*The same amount of the chemicals was added for all crystallisation temperatures and times

Table A-2: Amounts added of chemicals for syntheses of H/SAPO-34 with glucose and silver behenate as the MeSDA

	Amount added						
	Al	P	Si	TEPA	MOR	H ₂ O	MeSDA
H/GLU0.05	4.90g	7.96g	3.11g	0.26g	11.12g	45g	0.662g(GLU)
H/Agb0.03	4.90g	7.96g	3.11g	0.26g	11.12g	45g	0.929g(Agb)

Table A-3: Amounts added of chemicals for syntheses of C/CuSAPO-34

	Amount added							
	Al	P	Si	CuO	TEPA	MOR	H ₂ O	MeSDA
H/Si0.3_Cu0.02	4.90g	7.96g	3.11g	0.11g	0.26g	11.12g	44g	-
H/Si0.3_Cu0.04	4.90g	7.96g	3.11g	0.22g	0.52g	11.12g	45g	-
H/Si0.5_Cu0.04	4.90g	7.96g	5.18g	0.22g	0.52g	11.12g	44g	-

Table A-4: Amounts added of chemicals for syntheses of H/CuSAPO-34 using a variety of MeSDA

	Amount added							
	Al	P	Si	CuO	TEPA	MOR	H ₂ O	MeSDA
H/CTAB0.05_Cu0.02	4.90g	7.96g	3.11g	0.11g	0.26g	11.12g	45g	1.26g (CTAB)
H/CTAOH0.05_Cu0.02	4.90g	7.96g	3.11g	0.11g	0.26g	11.12g	45g	17.1mL (CTAOH)
H/DMOAC0.05_Cu0.02	4.90g	7.96g	3.11g	0.11g	0.26g	11.12g	45g	3.8g (DMOAC)
H/GLU0.05_Cu0.02	4.90g	7.96g	3.11g	0.11g	0.26g	11.12g	45g	0.62g (GLU)
H/TMODS0.05_Cu0.02	4.90g	7.96g	3.11g	0.11g	0.26g	11.12g	45g	1.90g (TMODS)
H/BA0.05_Cu0.02	4.90g	7.96g	3.11g	0.11g	0.26g	11.12g	45g	1.16g (BA)
H/AgB0.05_Cu0.02	4.90g	7.96g	3.11g	0.11g	0.26g	11.12g	45g	1.56g (Agb)

Table A-5: Amounts added of chemicals for syntheses of H/CuSAPO-34 using CTAOH as the MeSDA

	Amount added							
	Al	P	Si	CuO	TEPA	MOR	H ₂ O	CTAOH
H/Si0.3-Cu0.02	4.90g	7.96g	3.11g	0.110g	0.26g	11.12g	40g	5.39mL
H/Si0.3Cu0.03	4.90g	7.96g	3.11g	0.165g	0.39g	11.12g	40g	5.39mL
H/Si0.3Cu0.04	4.90g	7.96g	3.11g	0.220g	0.52g	11.12g	40g	5.39mL
H/Si0.3-Cu0.05	4.90g	7.96g	3.11g	0.275g	0.65g	11.12g	40g	5.39mL
H/Si0.3-Cu0.06	4.90g	7.96g	3.11g	0.329g	0.78g	11.12g	40g	5.39mL
H/Si0.5-Cu0.02	4.90g	7.96g	5.18g	0.110g	0.26g	11.12g	40g	5.39mL
H/Si0.5-Cu0.03	4.90g	7.96g	5.18g	0.165g	0.39g	11.12g	40g	5.39mL
H/Si0.5-Cu0.04	4.90g	7.96g	5.18g	0.220g	0.52g	11.12g	40g	5.39mL
H/Si0.5-Cu0.05	4.90g	7.96g	5.18g	0.275g	0.65g	11.12g	40g	5.39mL
H/Si0.5-Cu0.06	4.90g	7.96g	5.18g	0.329	0.78g	11.12g	40g	5.39mL

Appendix B: Additional XRD

Si/Al=0.3(As prepared)

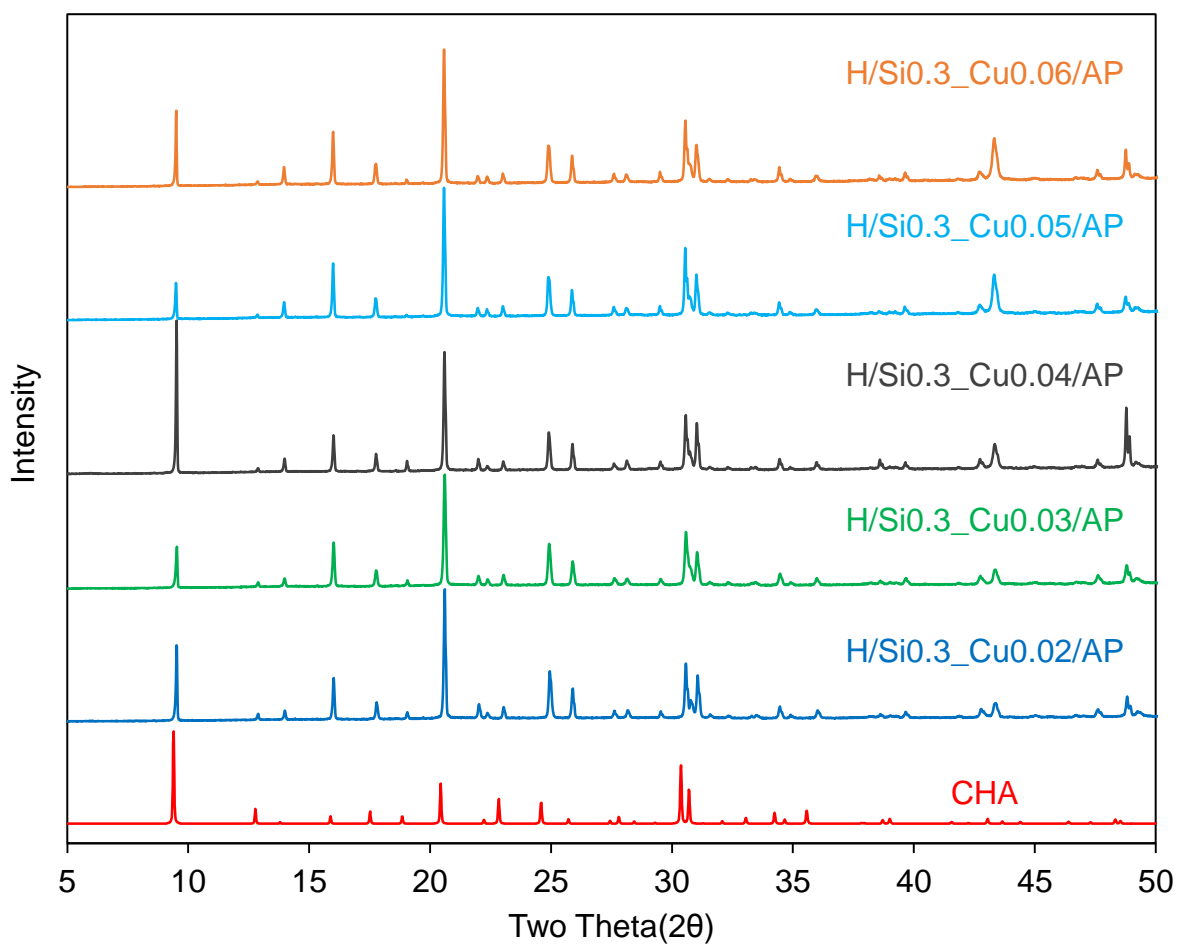


Figure B-1: Diffractograms of as prepared H/CuSAPO-34 samples made with CTAOH and Si/Al=0.3

Si/Al=0.3(Calcined)

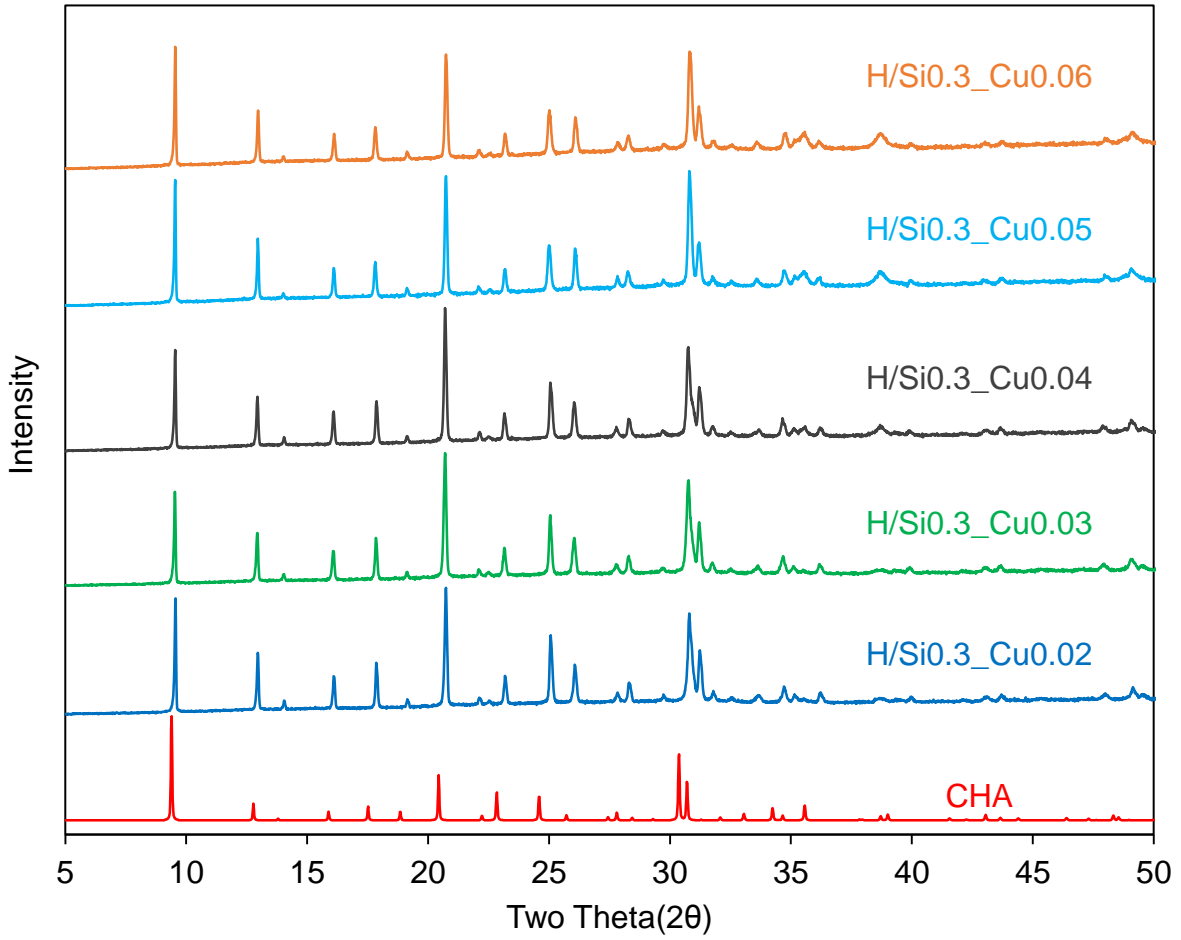


Figure B-2: Diffractograms of calcined H/CuSAPO-34 samples made with CTAOH and Si/Al=0.3

Appendix C: Additional SEM

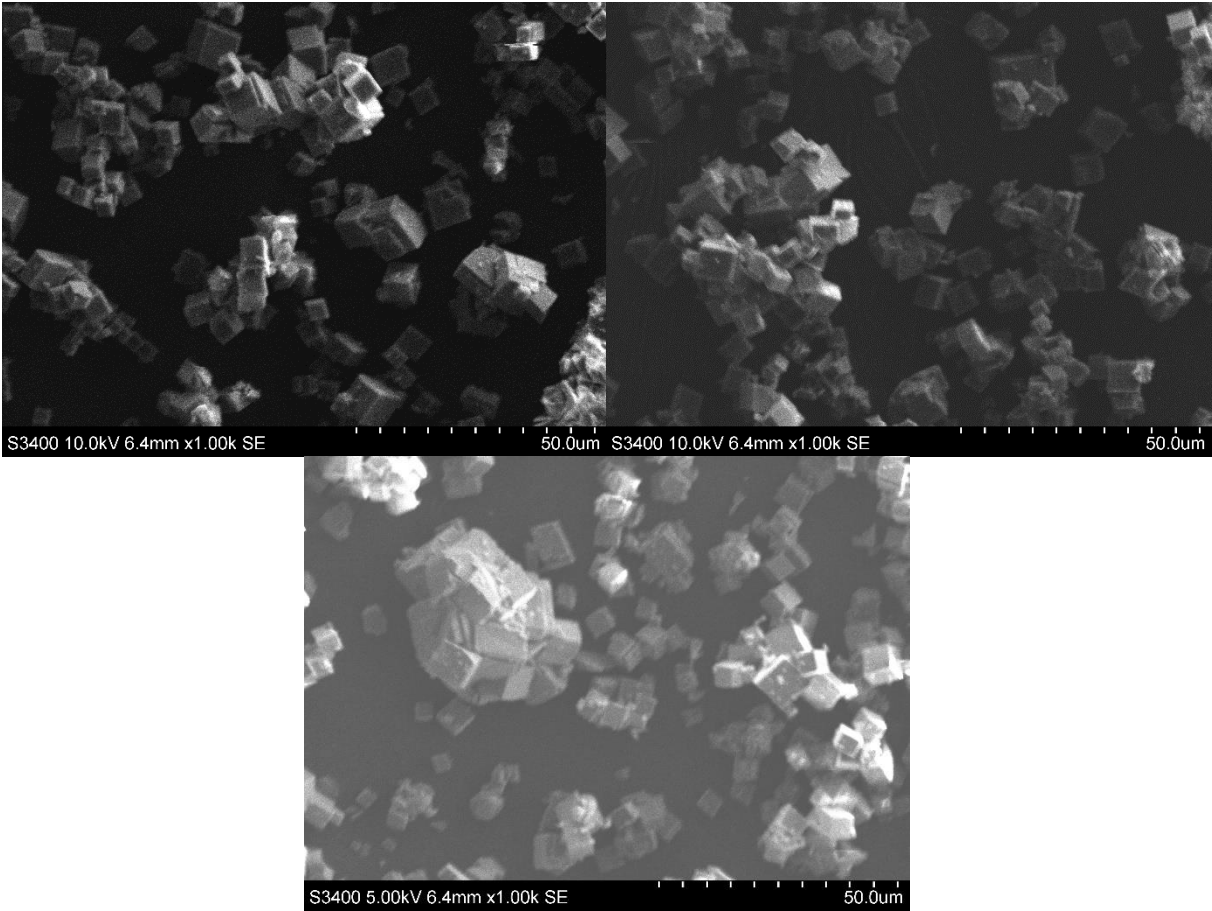


Figure C-1: Additional SEM images for C/Si_{0.3}Cu_{0.04}

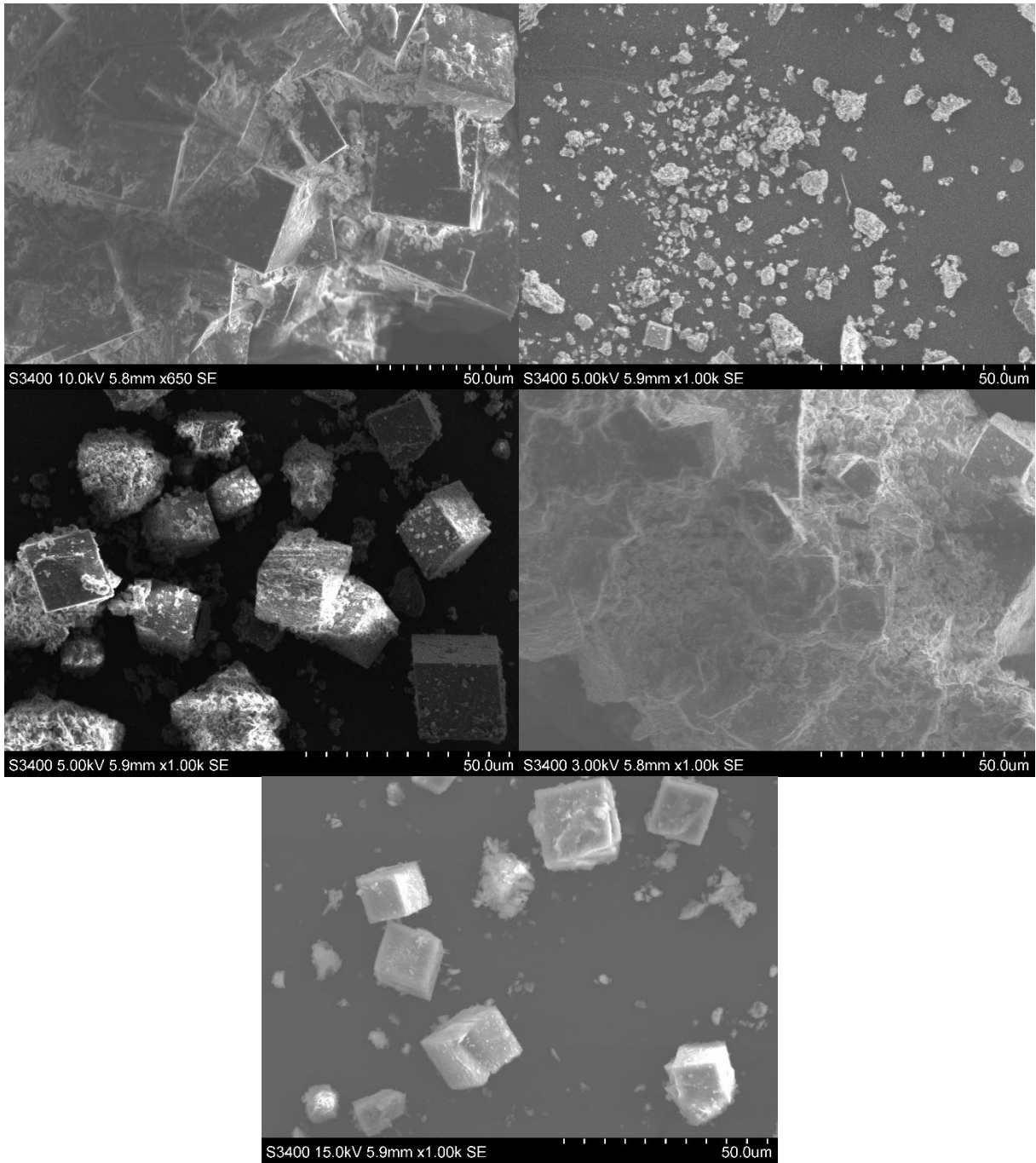


Figure C-2: Additional SEM images for C/Si_{0.5}_Cu_{0.02}

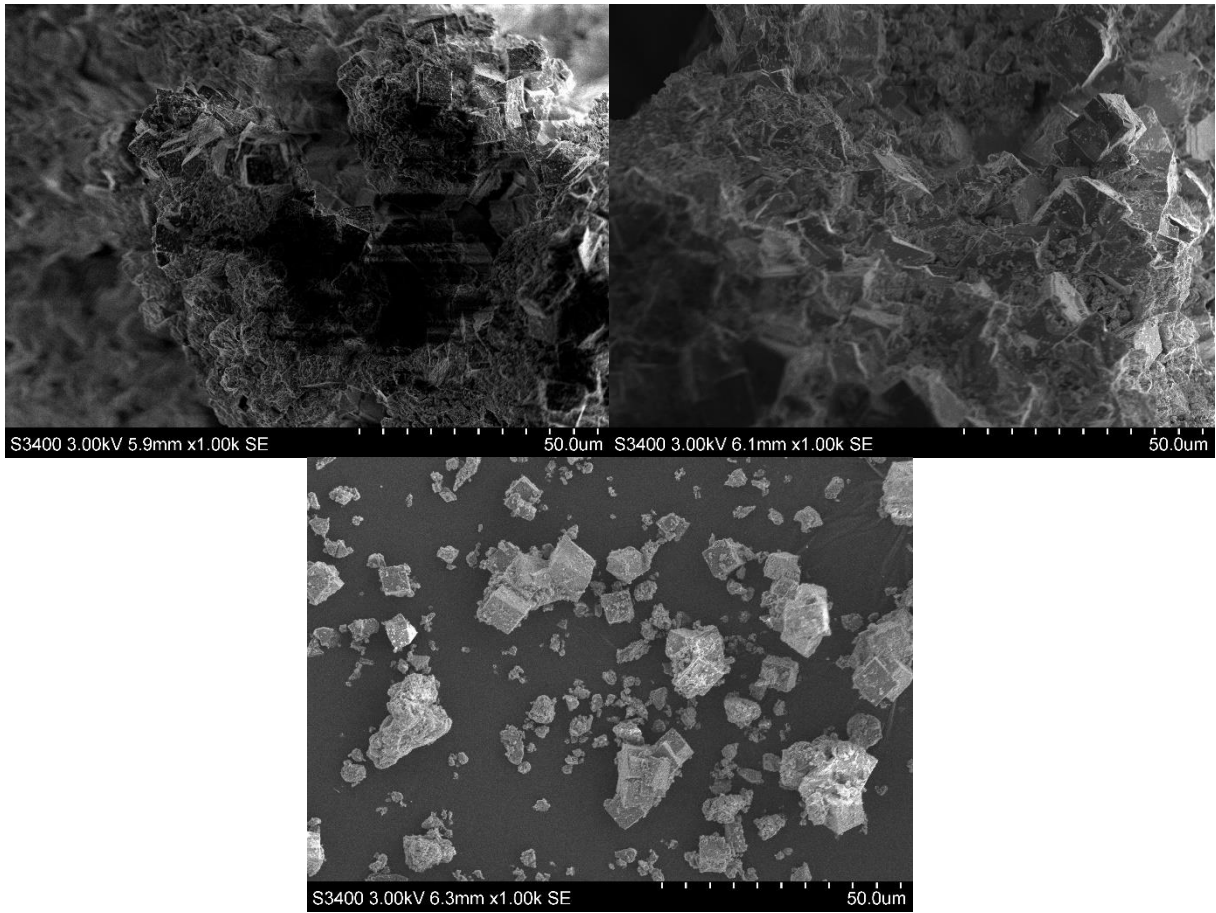


Figure C-3: Additional SEM images for $C/Si_{0.5}Cu_{0.04}$

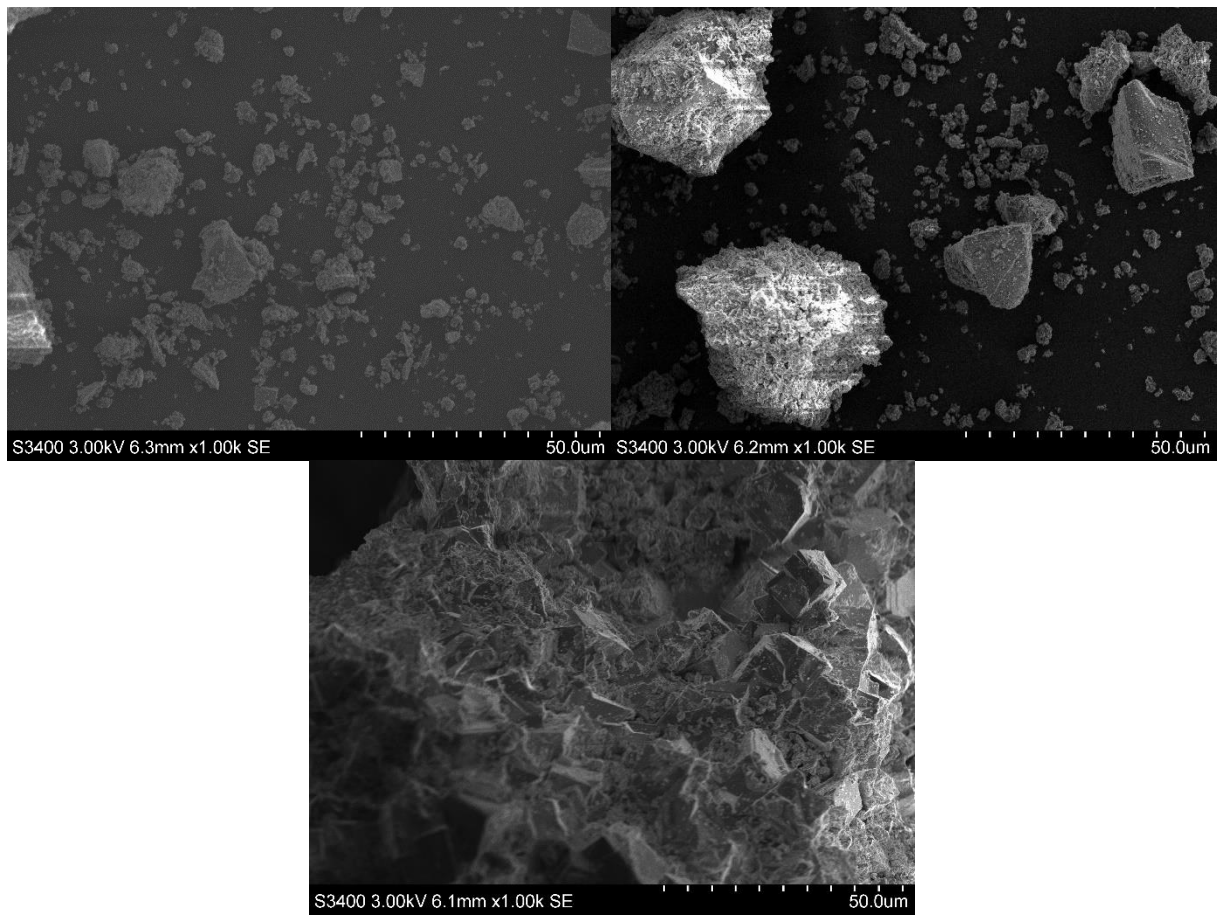


Figure C-4: Additional SEM images for H/Si_{0.3}Cu_{0.06}

Appendix D: Additional XAS

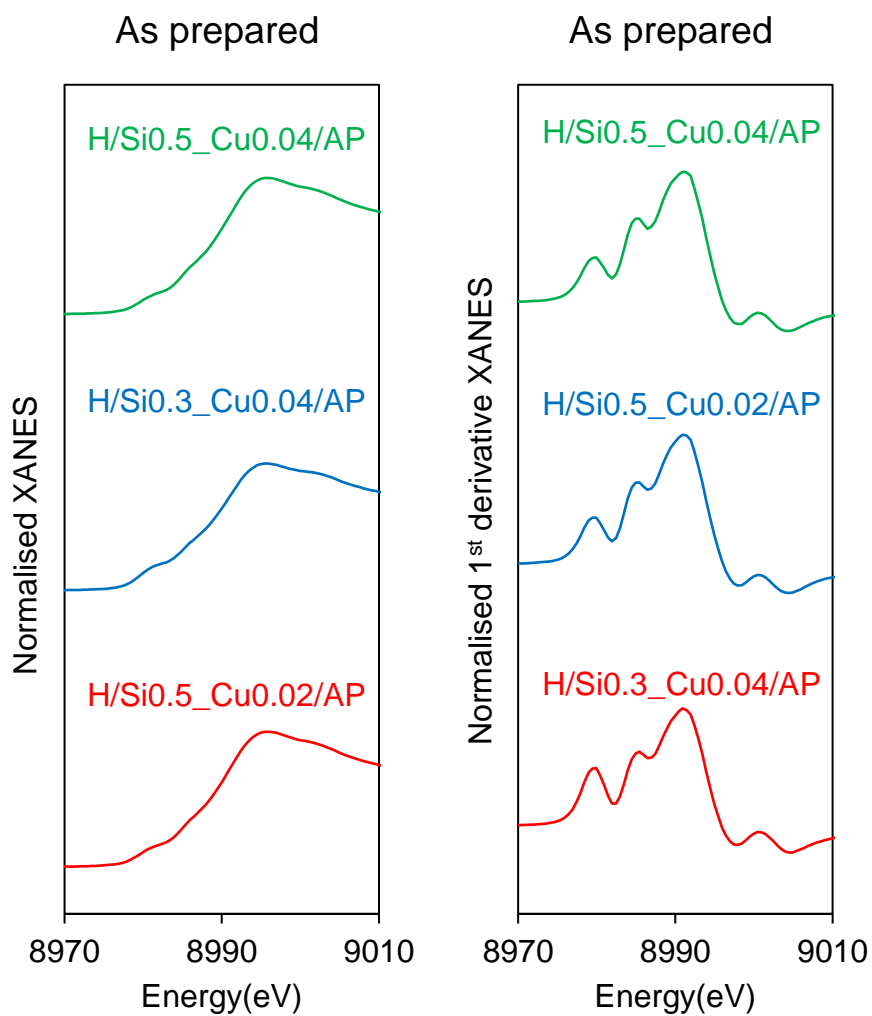


Figure D-1: Normalised XANES and 1st derivative XANES of H/Si0.3_Cu0.04/AP, H/Si0.5_Cu0.02/AP and H/Si0.5_Cu0.04/AP

Table D-1: The result of LFC for as prepared C/CuSAPO-34 and H/CuSAPO-34 samples

Sample name	Linear combination fitting			R-factor
	Cu-foil [%]	CuO [%]	Cu-tutton [%]	
C/Si0.5_Cu0.04/AP	28	47	25	0.004387
H/Si0.3_Cu0.04/AP	35	42	23	0.003583
H/Si0.5_Cu0.02/AP	47	36	18	0.003656
H/Si0.5_Cu0.04/AP	32	44	23	0.003581
H/Si0.5_Cu0.06/AP	75	20	5	0.005688

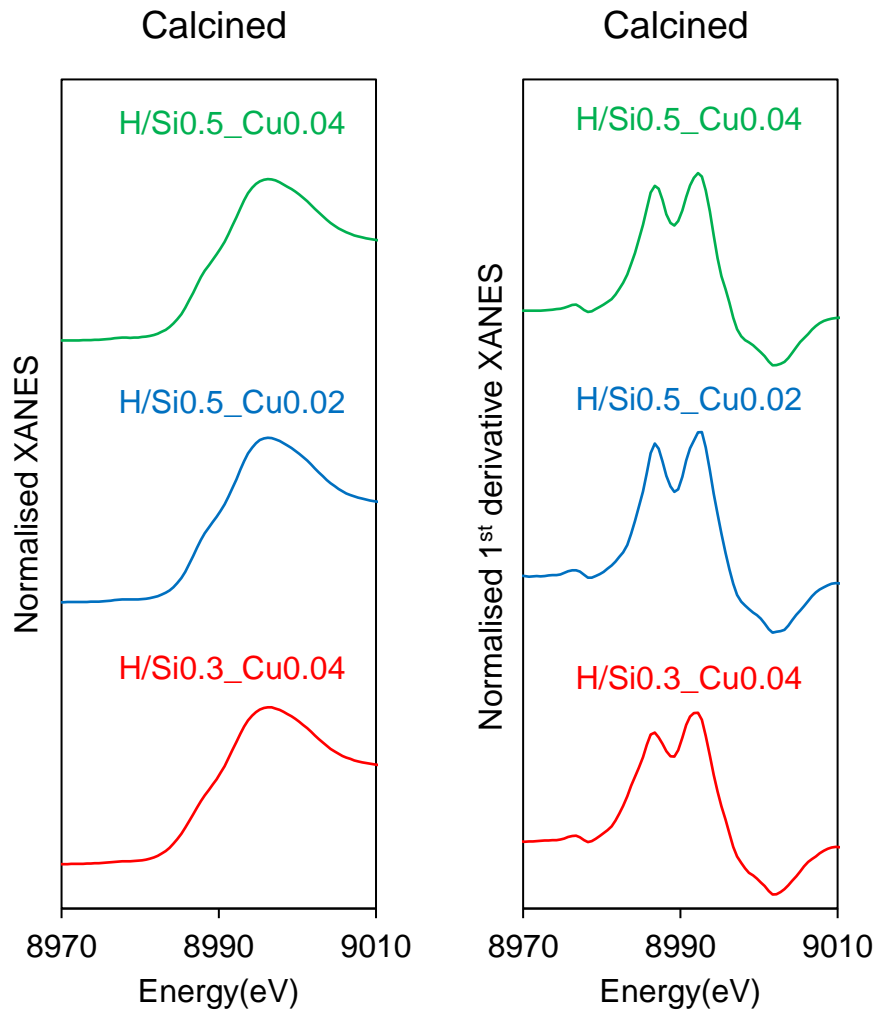


Figure D-2: Normalised XANES and 1st derivative XANES of H/Si0.3_Cu0.04, H/Si0.5_Cu0.02 and H/Si0.5_Cu0.04

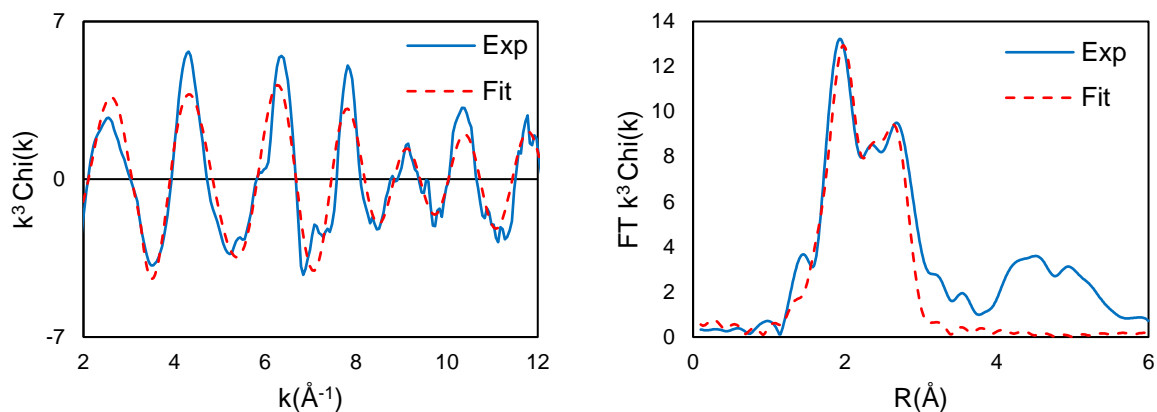


Figure D-3: The normalised EXAFS (Left) and Fourier transformation of the normalised EXAFS (Right) for C/Si_{0.3}Cu_{0.04}/AP. The blue line is the experimental data, and the dotted red line is the theoretically fitted curve

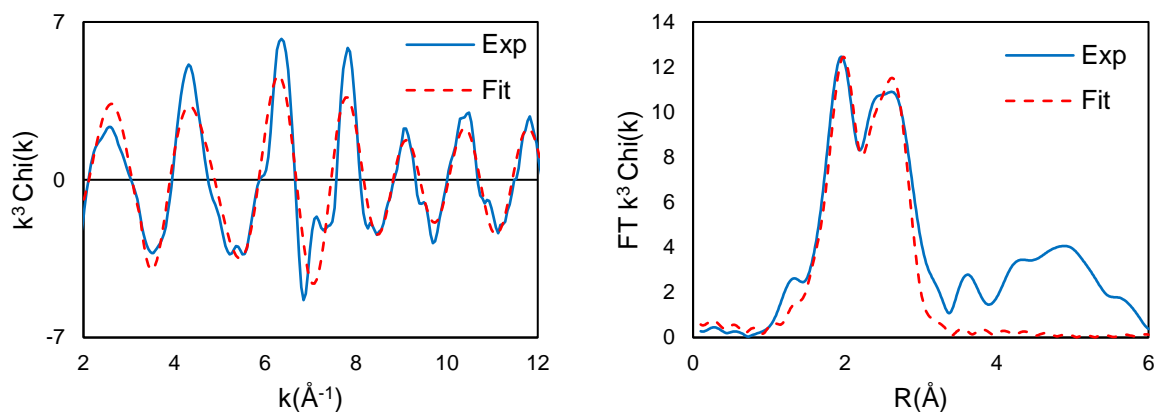


Figure D-4: The normalised EXAFS (Left) and Fourier transformation of the normalised EXAFS (Right) for H/Si_{0.5}Cu_{0.02} AP. The blue line is the experimental data, and the dotted red line is the theoretically fitted curve

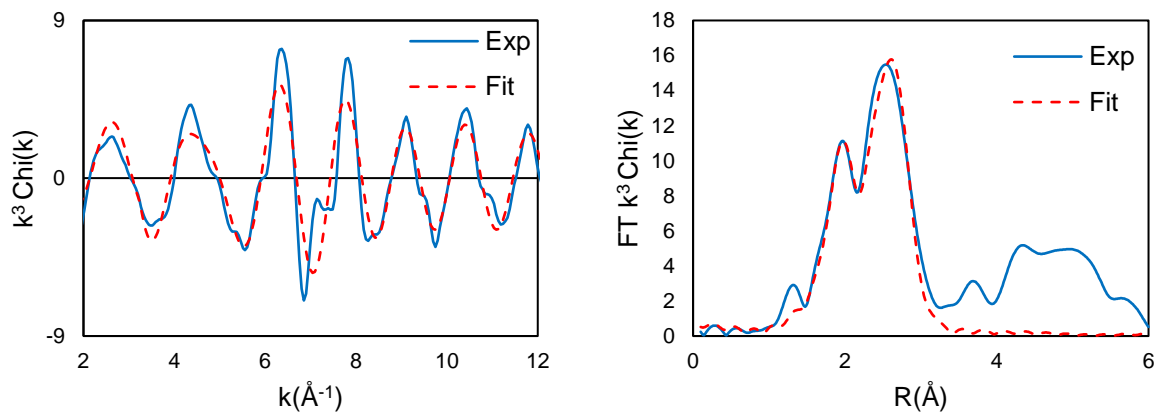


Figure D-5: The normalised EXAFS (Left) and Fourier transformation of the normalised EXAFS (Right) for H/Si_{0.3}Cu_{0.04} AP. The blue line is the experimental data, and the dotted red line is the theoretically fitted curve

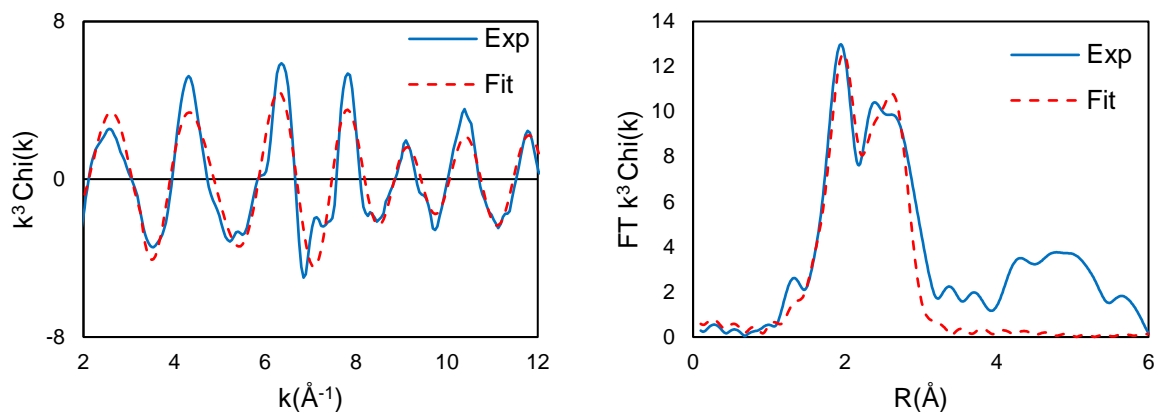


Figure D-6: The normalised EXAFS (Left) and Fourier transformation of the normalised EXAFS (Right) for H/Si_{0.5}Cu_{0.04}AP. The blue line is the experimental data, and the dotted red line is the theoretically fitted curve

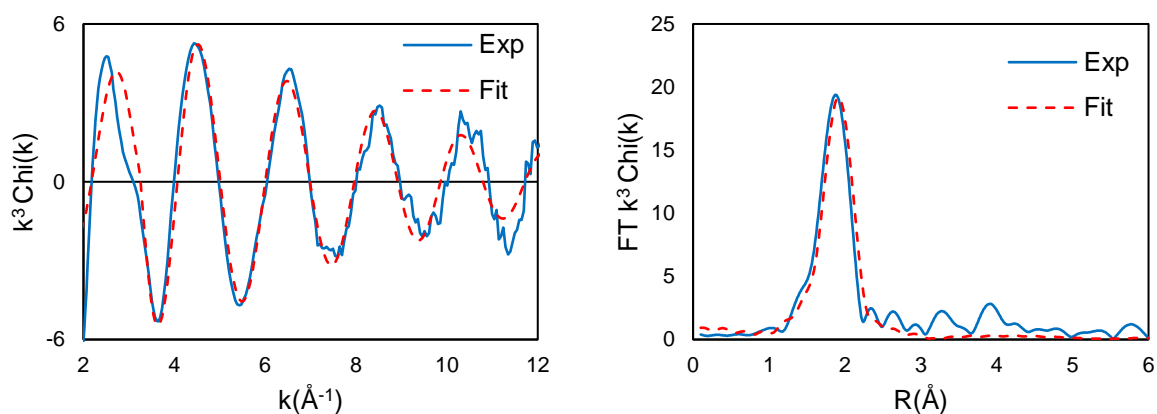


Figure D-7: The normalised EXAFS (Left) and Fourier transformation of the normalised EXAFS (Right) for C/Si_{0.3}Cu_{0.04}. The blue line is the experimental data, and the dotted red line is the theoretically fitted curve

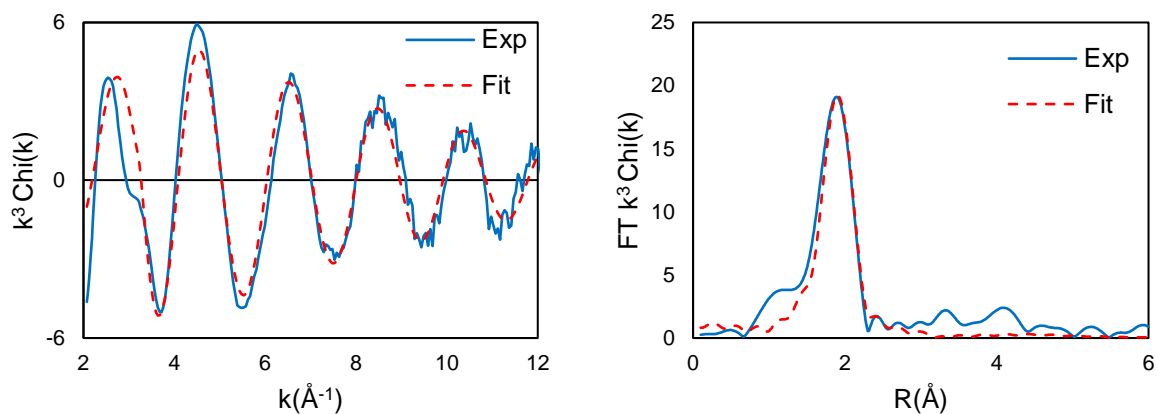


Figure D-8: The normalised EXAFS (Left) and Fourier transformation of the normalised EXAFS (Right) for H/Si_{0.5}Cu_{0.02}. The blue line is the experimental data, and the dotted red line is the theoretically fitted curve

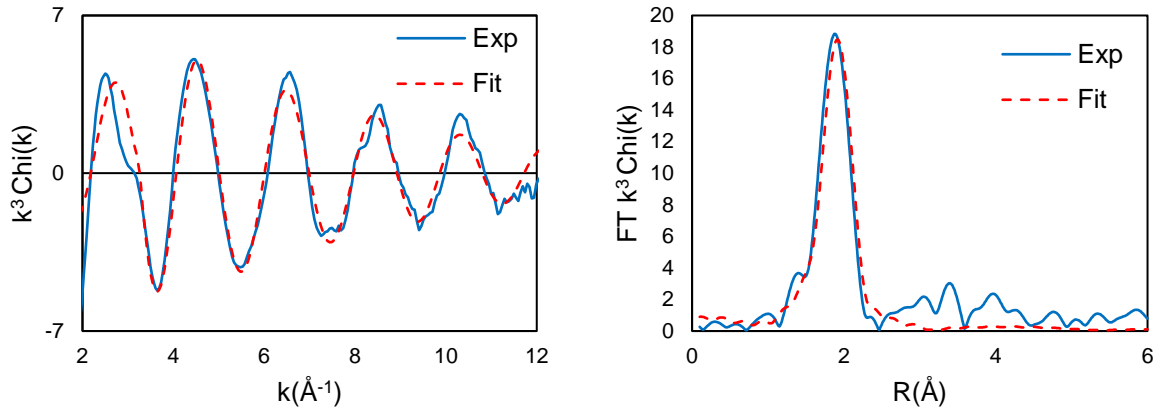


Figure D-9: The normalised EXAFS (Left) and Fourier transformation of the normalised EXAFS (Right) for H/Si_{0.3}Cu_{0.04}. The blue line is the experimental data, and the dotted red line is the theoretically fitted curve

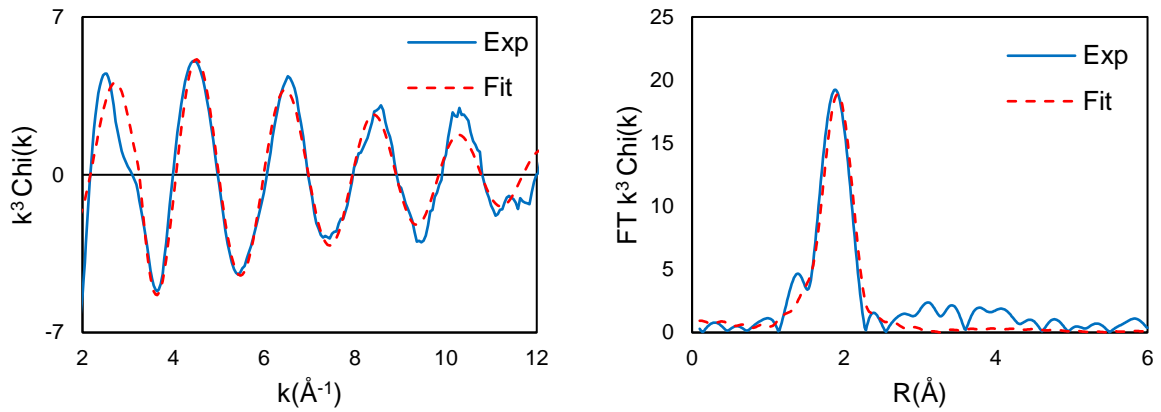


Figure D-10: The normalised EXAFS (Left) and Fourier transformation of the normalised EXAFS (Right) for H/Si_{0.5}Cu_{0.04}. The blue line is the experimental data, and the dotted red line is the theoretically fitted curve

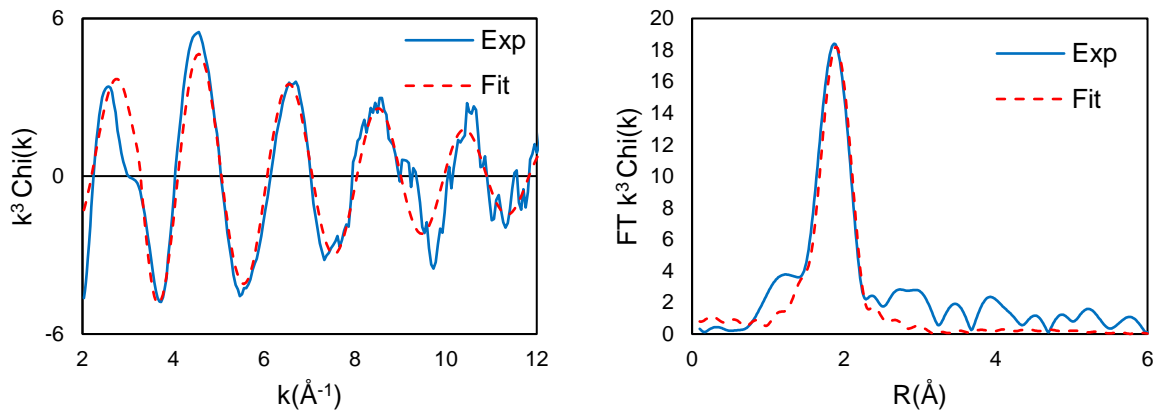


Figure D-11: The normalised EXAFS (Left) and Fourier transformation of the normalised EXAFS (Right) for H/Si_{0.5}Cu_{0.02}/HCd. The blue line is the experimental data, and the dotted red line is the theoretically fitted curve

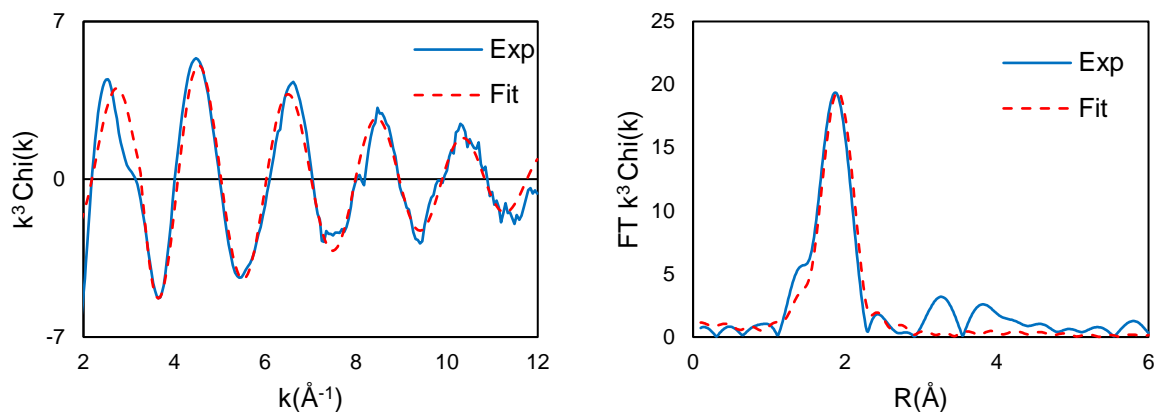


Figure D-12: Figure 8-1: The normalised EXAFS (Left) and Fourier transformation of the normalised EXAFS (Right) for H/Si_{0.5}Cu_{0.04}/HCd. The blue line is the experimental data, and the dotted red line is the theoretically fitted curve

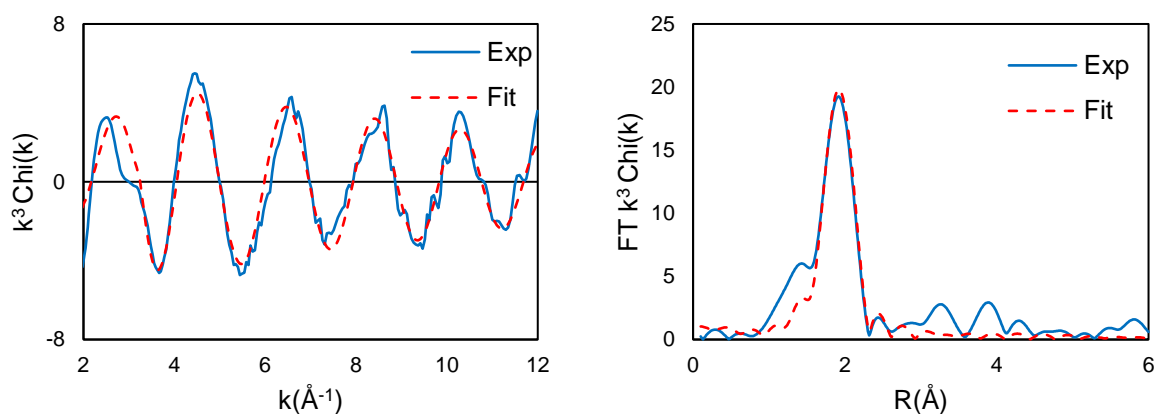


Figure D-13: The normalised EXAFS (Left) and Fourier transformation of the normalised EXAFS (Right) for H/Si_{0.5}Cu_{0.04}/HCw. The blue line is the experimental data, and the dotted red line is the theoretically fitted curve

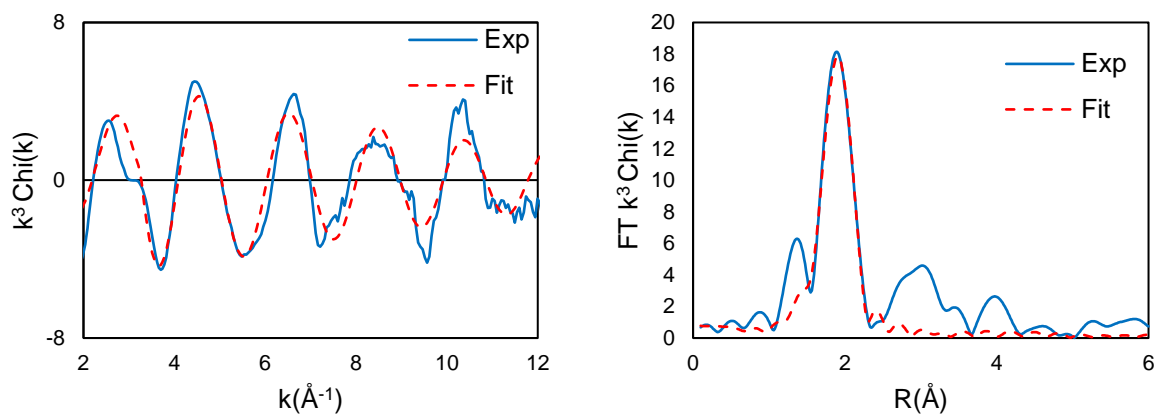


Figure D-14: The normalised EXAFS (Left) and Fourier transformation of the normalised EXAFS (Right) for H/Si_{0.5}Cu_{0.06}/HCd. The blue line is the experimental data, and the dotted red line is the theoretically fitted curve

Appendix E: Additional HC-SCR

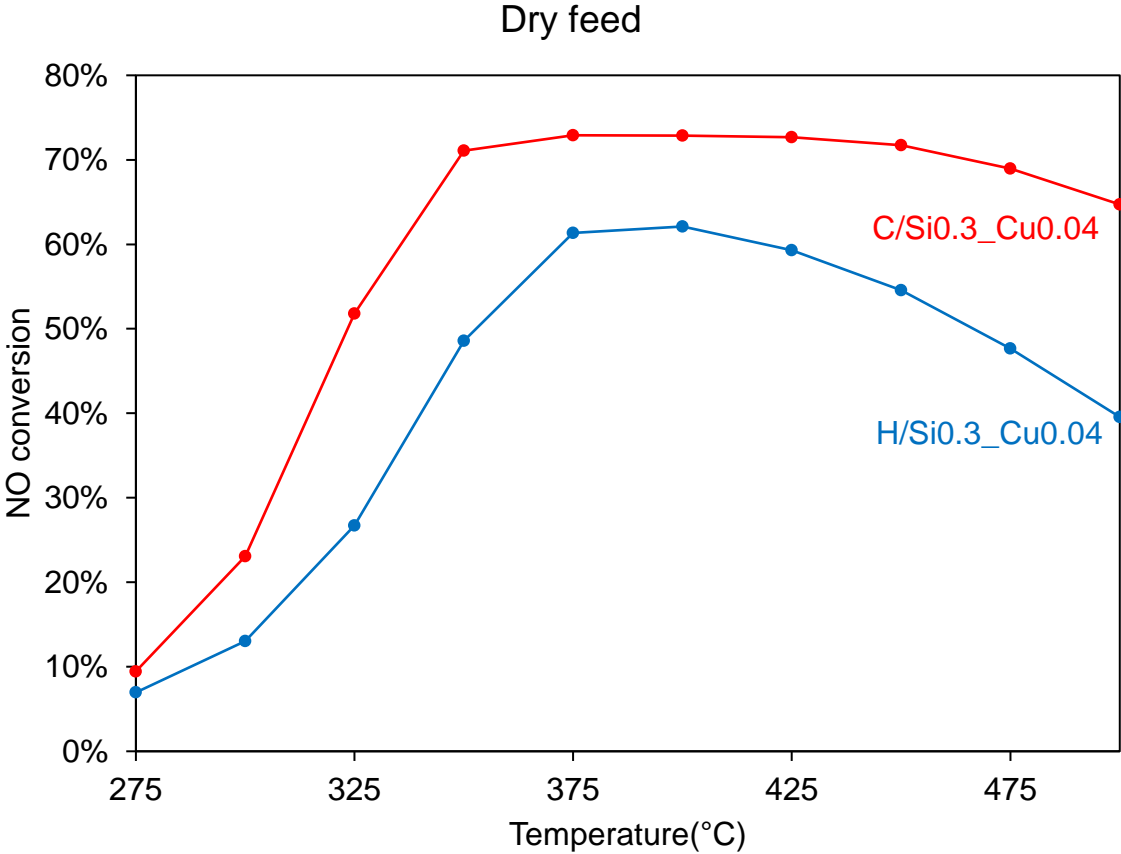


Figure E-1: NO conversion for C/Si_{0.3}_Cu_{0.04} and H/Si_{0.3}_Cu_{0.04} in dry feed